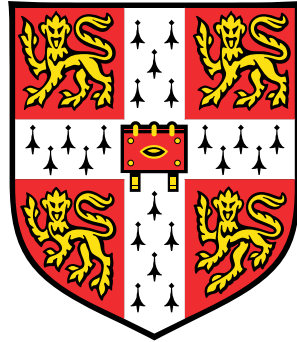


A Unified Framework for Simulating Impact-Induced Detonation of a Combustible Material in an Elasto-Plastic Confiner



Haran Jackson

The Centre for Scientific Computing

University of Cambridge

This dissertation is submitted for the degree of

Doctor of Philosophy in Scientific Computing

Fitzwilliam College

Supervisor: Dr N. Nikiforakis

Declaration

This dissertation is the result of my own work and includes nothing which is the outcome of work done in collaboration except where specifically indicated in the text.

Word Count (including tables, figure legends, and appendices):

Haran Jackson
January 4th 2018

Acknowledgements

I would like to thank my supervisor, Dr Nikos Nikiforakis, for all the help and guidance he has given me. Additionally, I would like to thank Dr Louisa Michael, Geraint Harcombe, Tomé Gouveia, Knut Sverdrup, and Bruno Dog for the many useful discussions we had.

Research Output

During my PhD, I acted as a reviewer for the Journal of Computational Physics. The following materials were produced over the course of my programme.

Publications

- H Jackson, N Nikiforakis, *Fast numerical schemes for plastic simulation with the Godunov-Peshkov-Romenski model* (in preparation)
- H Jackson, G Harcombe, N Nikiforakis, *A solver based on eigendecomposition of the Cauchy tensor for Godunov-Romenski-type continuum models* (in preparation)
- H Jackson, N Nikiforakis, *A Riemann ghost fluid method for modeling multimaterial interfaces with the GPR model* (in preparation)
- H Jackson, *The Montecinos-Balsara ADER-FV polynomial basis: convergence properties & extension to non-conservative multidimensional systems* (Computers & Fluids, 2018)
- H Jackson, *A fast numerical scheme for the Godunov-Peshkov-Romenski model of continuum mechanics* (Journal of Computational Physics, 2017)
- H Jackson, *On the eigenvalues of the ADER-WENO Galerkin predictor* (Journal of Computational Physics, 2017)

Conference Presentations

- International Conference on Computational Science 2017 (Zürich, CH), *Paper: A Fast Numerical Scheme for the Godunov-Peshkov-Romenski Model of Continuum Mechanics*
- SIAM International Conference on Numerical Combustion 2017 (Orlando, FL), *Minisymposium: A New Approach for Cook-off Modeling*

-
- Scientific Computation in the University of Cambridge Seminar Day 2017 (Cambridge, UK), *Poster: A Numerical Method based on Operator Splitting for the GPR Model of Continuum Mechanics*
 - Cavendish Graduate Student Conference 2016 (Cambridge, UK), *Poster: A New Framework for Simulating Multimaterial Systems and Gaseous Cookoff*

Open-Source Software

- ADER (pypi.org/project/ADER): The ADER method for solving any (potentially very stiff) hyperbolic system of PDEs
- Julia-WENO (github.com/haranjackson/Julia-WENO): An optimized Julia implementation of the WENO reconstruction algorithm, of any order of accuracy
- Euler1D (github.com/haranjackson/Euler1D): A few first- and second-order methods for solving the 1D Euler equations, implemented in C++
- ProjectionMethod (github.com/haranjackson/ProjectionMethod): A C++ implementation of Chorin's Project Method
- NewtonKrylov (github.com/haranjackson/NewtonKrylov): A C++ implementation of the Newton-Krylov algorithm, with Python bindings
- LGMRES (github.com/haranjackson/LGMRES): A C++ implementation of the LGMRES algorithm, with Python bindings (1star, 1 fork)
- LegendreGauss (github.com/haranjackson/LegendreGauss): C++ code to compute the Legendre-Gauss nodes and weights on $[-1,1]$, based on NumPy's `leggauss` function

Abstract

Contents

Contents	vi
List of Figures	x
List of Tables	xiv
Nomenclature	xvii
0 Introduction	1
0.1 Background	1
0.2 Objectives of this Study	1
0.3 Mathematical Model	1
0.4 Numerical Methods	4
0.4.1 The WENO Reconstruction	5
0.4.2 The Galerkin Predictor	7
0.4.3 The Finite Volume Scheme	11
0.4.4 Time Step and Boundary Conditions	12
1 Objective 1: Extending the GPR Model	13
1.1 Equations of State	13
1.1.1 Mie-Gruneisen Models	13
1.1.2 Variable Transverse Perturbation Speed	14
1.2 Multiphase Reactive Materials	18
1.2.1 Extended Model	18
1.2.2 Mixture Rules	19

1.2.3	Reaction Rate Laws	21
1.3	Numerical Treatment of Source Terms	22
1.4	Numerical Results	22
1.4.1	Seven-Wave Elastic Riemann Problem	22
1.4.2	Shock-Induced Detonation	25
1.4.3	Heating-Induced Deflagration	25
1.4.4	Heating-Induced Detonation	27
2	Objective 2: Improved Numerical Methods	31
2.1	Extending the Montecinos-Balsara ADER Method	31
2.1.1	The Discontinuous Galerkin Method	34
2.1.2	The Continuous Galerkin Method	36
2.1.3	Convergence Properties	37
2.2	Operator Splitting Methods	39
2.2.1	The Homogeneous System	40
2.2.2	The Thermal Impulse ODEs	42
2.2.3	The Distortion ODEs	43
2.2.4	Distortion Correction in Fluids	56
2.3	Numerical Results	57
2.3.1	Newtonian Fluids & Elastic Solids	57
2.3.2	Non-Newtonian Fluids & Elastoplastic Solids	67
2.4	Conclusions	74

3	Objective 3: Simulating Material Interfaces	79
3.1	Ghost Fluid Methods	79
3.1.1	Level Set Methods	79
3.1.2	The Original Ghost Fluid Method	79
3.1.3	The Riemann Ghost Fluid Method	82
3.2	A Riemann Ghost Fluid Method for the GPR Model	83
3.2.1	Solving the Riemann Problem	83
3.2.2	Linear Conditions	90
3.2.3	The Case without Heat Conduction	91
3.3	Numerical Results	93
3.3.1	Helium Bubble	93
3.3.2	Water-Air Shock Tube	95
3.3.3	Copper-PBX Impact	95
3.3.4	Aluminium in Vacuum	95
3.3.5	Heat Conduction in a Gas	95
3.3.6	Intermaterial Heating-Induced Acoustic Wave	100
3.3.7	Aluminium Plates	105
3.3.8	Taylor Bar	105
4	Impact-Induced Detonation in an Elasto-Plastic Confiner	106
4.1	Reactive C4 Confined by Steel	106
4.2	Reactive C4 Confined by Steel with Air Gap	106
4.3	Rod Impact on Copper Vessel	106
5	Conclusions & Discussion	107
	References	108

A	System Matrices	115
A.1	Fluxes, Sources, and Non-Conservative Terms	115
A.2	Jacobians	115
B	Eigenstructure	126
B.1	Primitive System	126
B.2	Eigenvalues	128
B.3	Eigenvectors	131
C	Model Parameters	138
C.1	Material Properties	138
C.2	Equation of State Parameters	138
C.3	Combustion Parameters	139

List of Figures

1.1	Density and velocity for the 7-wave elastic Riemann problem	23
1.2	Total stress for the 7-wave elastic Riemann problem	24
1.3	Pressure, density, concentration of reactant, and velocity (in the reference frame of the shock) in the viscous shock-induced detonation test	26
1.4	Temperature, pressure, and concentration of reactant in the heating-induced deflagration test with inert gas (left) / reactive gas (right)	28
1.5	Temperature, pressure, and concentration of reactant in the heating-induced detonation test	30
2.1	The (shaded) region to which x_i, x_j are confined in the evolution of the distortion ODEs	46
2.2	The stress-strain relationships for different kinds of fluids (source [REF]) . .	51
2.3	The components of the distortion tensor in the Strain Relaxation Test	58
2.4	The singular values of the distortion tensor and the energy in the Strain Relaxation Test	58
2.5	The components of the stress tensor in the Strain Relaxation Test	58
2.6	Results of solving Stokes' First Problem ($\mu = 10^{-2}, \mu = 10^{-3}, \mu = 10^{-4}$) with an ADER-WENO scheme and a Split-WENO scheme ($N = 2$)	60
2.7	Density, velocity, and pressure for the Viscous Shock problem, solved with an ADER-WENO scheme and a Split-WENO scheme ($N = 2$)	63
2.8	Viscous stress and heat flux for the Viscous Shock problem, solved with both an ADER-WENO scheme and a Split-WENO scheme ($N = 2$)	64

2.9	Results of solving the problem of Heat Conduction in Gas with both an ADER-WENO scheme and a Split-WENO scheme ($N = 2$)	64
2.10	Results for the 3-wave and 5-wave purely elastic Riemann problems	65
2.11	Components of the distortion tensor during the Strain Relaxation Test: approximate analytical solution (crosses) is compared with numerical ODE solution (solid line)	69
2.12	Stress tensor during the Strain Relaxation Test: approximate analytical solution (crosses) is compared with numerical ODE solution (solid line)	69
2.13	Total energy during the Strain Relaxation Test: approximate analytical solution (crosses) is compared with numerical ODE solution (solid line)	71
2.14	Velocity profiles for different dilatants (left) and pseudoplastics (right), in steady Poiseuille flow	71
2.15	Velocity profiles for the Lid-Driven Cavity Test under the new formulation (solid line), for a dilatant with $n=1.5$. Slices are taken through the center of the domain, in both axes, and compared with those of [11] and [56].	72
2.16	Velocity profiles for the Lid-Driven Cavity Test under the new formulation (solid line), for a pseudoplastic with $n=0.5$. Slices are taken through the center of the domain, in both axes, and compared with those of [11] and [56].	72
2.17	Streamplots for the Lid-Driven Cavity Test, for a pseudoplastic with $n=0.5$ (left) and a dilatant with $n=1.5$ (right)	73
2.18	Density and velocity in the elastoplastic piston test, for various values of power-law parameter n	73
2.19	Zoom view of density and velocity in the elastoplastic piston test, for various values of power-law parameter n	75
2.20	1D density profiles for the 2D Cylindrical Shock Test, comparing the GPR model w/ split solver (left) with the results from [8] (right)	75
2.21	1D velocity profiles for the 2D Cylindrical Shock Test, comparing the GPR model w/ split solver (left) with the results from [8] (right)	76

2.22	1D stress tensor profiles for the 2D Cylindrical Shock Test, comparing the GPR model w/ split solver (left) with the results from [8] (right)	76
2.23	1D temperature profiles for the 2D Cylindrical Shock Test, comparing the GPR model w/ split solver (left) with the results from [8] (right)	77
2.24	2D plots of density and speed for the Cylindrical Shock Test	77
3.1	The Original Ghost Fluid Method	80
3.2	The Original Ghost Fluid Method, with the isobaric fix	81
3.3	The qualitative structure of the solution to the Riemann Problem, showing the different possible types of waves	82
3.4	The Riemann Ghost Fluid Method	83
3.5	The Riemann Problem for the GPR model, assuming all waves are distinct	84
3.6	Different sets of characteristic curves, traveling from their respective initial points to the star region	85
3.7	Density, pressure, and velocity for the helium bubble test with GPR-RGFM at times $t = 7 \times 10^{-4}$ (left) and $t = 14 \times 10^{-4}$ (right)	94
3.8	Density, pressure, velocity, and internal energy for the water-air shock tube test with GPR-RGFM	96
3.9	Density, velocity, and total stress for the Copper-PBX test with GPR-RGFM	97
3.10	Density, velocity, and total stress for the aluminium-vacuum test with GPR-RGFM	98
3.11	Density, velocity, and total stress for the aluminium-vacuum test with GPR-RGFM, including thermal conduction	99
3.12	Temperature, heat flux, and density for the intermaterial heat conduction test with GPR-RGFM	101

3.13	Temperature and pressure for the intermaterial heating-induced acoustic wave test with: a single volume of air (top); two volumes of air initially separated at $x^* = 22.5$ (middle); air and helium initially separated at $x^* = 22.5$ (bottom).	103
3.14	Heat flux for the intermaterial heating-induced acoustic wave test with: a single volume of air (top); two volumes of air initially separated at $x^* = 22.5$ (middle); air and helium initially separated at $x^* = 22.5$ (bottom).	104
3.15	The aluminium plate impact test, at various different times	105

List of Tables

1.1	$e^{ref}, p^{ref}, \Gamma, T_{ref}$ for different kinds of Mie-Gruneisen equations of state . . .	15
1.2	$\frac{de^{ref}}{d\rho}, \frac{dp^{ref}}{d\rho}, \Gamma'$ for different kinds of Mie-Gruneisen equations of state	16
1.3	Initial conditions for the viscous shock-induced detonation test	25
2.1	Initial conditions for the slow opposing shear flow test	57
2.2	Initial conditions for the heat conduction test	62
2.3	Wall time for various tests (all with 200 cells) under the ADER-WENO method and the Split-WENO method	68
2.4	Time steps taken for various tests (all with 200 cells) under the ADER-WENO method and the Split-WENO method	68
2.5	Convergence rates for the Split-WENO method ($N = 2$)	68
2.6	Convergence rates for the Split-WENO method ($N = 3$)	68
2.7	Convergence rates for the ADER-DG PNPM method ($N, M = 2$)	69
3.1	Initial conditions for the helium bubble test	95
3.2	Initial conditions for the water-air shock tube test	95
3.3	Initial conditions for the heat conduction test	100
3.4	Initial conditions for the intermaterial heating-induced acoustic wave test . .	102
3.5	Mass of the air volume in scenarios 2 and 3 at various times	102
C.1	Reference parameters for various materials	138
C.2	Parameters for the Ideal-/Stiffened-Gas, Shock Mie-Gruneisen, and Godunov-Romenski equations of state	138
C.3	Plasticity parameters for various materials	139

Nomenclature

Roman Symbols

\boldsymbol{J}	Thermal impulse vector
\boldsymbol{q}	Heat flux vector
\boldsymbol{v}	Velocity
\boldsymbol{A}	Distortion tensor
B_c	Prefactor in Arrhenius reaction kinetics
c_0	Adiabatic speed of sound
c_h	Characteristic velocity of heat waves
c_p	Specific heat capacity at constant pressure
c_s	Characteristic velocity of transverse perturbations
c_v	Specific heat capacity at constant volume
E	Total specific energy
E_a	Activation energy of a reactive species
K_0	Reaction rate in discrete ignition temperature reaction kinetics
p	Pressure
p_∞	Pressure constant in stiffened gas equation of state
Q_c	Energy formed per unit mass of reactant
R_c	Universal gas constant
s	Entropy
T	Temperature

t	Time variable
T^{ref}	Reference temperature appearing in the Mie-Gruneisen EOS
T_i	Ignition temperature in discrete ignition temperature reaction kinetics
x	Space variable

Greek Symbols

α	A constant appearing in the Godunov-Romenski EOS
β	A constant appearing in the Godunov-Romenski EOS
δ	Kronecker delta
γ	A constant appearing in the Godunov-Romenski EOS
γ	Ratio of specific heat capacities, equal to $\frac{c_p}{c_v}$
λ	Concentration of reactive species
ρ	Density
ρ_0	Reference density
Σ	Total stress tensor
σ	Viscous shear stress tensor
c_t	Coefficient in the thermal impulse contribution to the energy (denoted elsewhere in the literature by α)
τ_1	Strain dissipation time
τ_2	Thermal impulse dissipation time

Other Symbols

$\ \cdot\ $	Euclidean vector norm
$\ \cdot\ _F$	Frobenius matrix norm

Acronyms / Abbreviations

CJ	Chapman-Jouguet
DG	Discontinuous Galerkin
EOS	Equation of State
FV	Finite Volume
WENO	Weighted Essentially Non-Oscillatory
ZND	Zel'dovich-Neumann-Doring

Notes

Unless otherwise stated, repeated indices in vector, matrix and tensor quantities are to be summed over. If M is a matrix, then M_i is taken to be the i th column of M (note, not the i th row). MATLAB-style index notation is used, such that $M_{i:j}$ refers to the matrix consisting of the columns $i \dots j$ of M (including columns i and j). $M_{i:j,m:n}$ refers to the submatrix of M with corners at M_{im} and M_{jn} .

Chapter 0

Introduction

0.1 Background

0.2 Objectives of this Study

0.3 Mathematical Model

The GPR model, first introduced in Peshkov and Romenski [61] - and expanded upon by Dumbser et al. [24] and Boscheri et al. [13] - takes the following form:

$$\frac{\partial \rho}{\partial t} + \frac{\partial (\rho v_k)}{\partial x_k} = 0 \quad (1a)$$

$$\frac{\partial (\rho v_i)}{\partial t} + \frac{\partial (\rho v_i v_k + p \delta_{ik} - \sigma_{ik})}{\partial x_k} = 0 \quad (1b)$$

$$\frac{\partial A_{ij}}{\partial t} + \frac{\partial (A_{ik} v_k)}{\partial x_j} + v_k \left(\frac{\partial A_{ij}}{\partial x_k} - \frac{\partial A_{ik}}{\partial x_j} \right) = -\frac{\psi_{ij}}{\theta_1} \quad (1c)$$

$$\frac{\partial (\rho J_i)}{\partial t} + \frac{\partial (\rho J_i v_k + T \delta_{ik})}{\partial x_k} = -\frac{\rho H_i}{\theta_2} \quad (1d)$$

$$\frac{\partial (\rho s)}{\partial t} + \frac{\partial (\rho s v_k + H_k)}{\partial x_k} = \frac{\rho}{T} \left(\frac{\psi_{kl} \psi_{kl}}{\theta_1} + \frac{H_k H_k}{\theta_2} \right) \quad (1e)$$

where θ_1 and θ_2 are positive scalar functions, and $\psi = \frac{\partial E}{\partial A}$ and $\mathbf{H} = \frac{\partial E}{\partial J}$. Entropy does not decrease during the dissipative time evolution:

$$\frac{\partial (\rho s)}{\partial t} + \frac{\partial (\rho s v_k + H_k)}{\partial x_k} \geq 0 \quad (2)$$

(1e) can be replaced with the following equation, which will be used instead when solving the model in this study:

$$\frac{\partial (\rho E)}{\partial t} + \frac{\partial (\rho E v_k + (p \delta_{ik} - \sigma_{ik}) v_i + q_k)}{\partial x_k} = 0 \quad (3)$$

Note that (1a), (1b), (1c), (1d), (3) can be written in the following form:

$$\frac{\partial Q}{\partial t} + \nabla \cdot \mathbf{F} + \mathbf{B} \cdot \nabla Q = S \quad (4)$$

The following definitions are given:

$$p = \rho^2 \left. \frac{\partial E}{\partial \rho} \right|_{s,A} \quad (5a)$$

$$\sigma = -\rho A^T \left. \frac{\partial E}{\partial A} \right|_{\rho,s} \quad (5b)$$

$$T = \left. \frac{\partial E}{\partial s} \right|_{\rho,A} \quad (5c)$$

$$\mathbf{q} = T \frac{\partial E}{\partial \mathbf{J}} \quad (5d)$$

To close the system, the EOS must be specified, from which the above quantities and the sources can be derived. E is the sum of the contributions of the energies at the molecular scale (microscale), the material element¹ scale (mesoscale), and the flow scale (macroscale):

$$E = E_1(\rho, s) + E_2(\rho, s, A, \mathbf{J}) + E_3(\mathbf{v}) \quad (6)$$

In previous studies, E_1 has to been taken to be either the ideal gas EOS, the stiffened gas EOS, or the shock Mie-Gruneisen EOS. A more general set of choices for E_1 is given in Section 1.1.

E_2 has the following quadratic form:

$$E_2 = \frac{c_s(\rho, s)^2}{4} \|\text{dev}(G)\|_F^2 + \frac{c_t(\rho, s)^2}{2} \|\mathbf{J}\|^2 \quad (7)$$

c_s is the characteristic velocity of transverse perturbations. In previous studies, c_s has always been constant. In this study, it will be extended to have a ρ dependence, as outlined in Section 1.1. c_t is related to the characteristic velocity of propagation of heat waves:

$$c_h = \frac{c_t}{\rho} \sqrt{\frac{T}{c_v}} \quad (8)$$

¹The concept of a *material element* corresponds to that of a fluid parcel from fluid dynamics, applied to both fluids and solids.

0.3 Mathematical Model

In previous studies, c_t has been taken to be constant, as it will in this study. Note that Dumbser [24] denotes this variable by α , which is avoided here due to a clash with a parameter of one of the equations of state used.

$G = A^T A$ is the Gramian matrix of the distortion tensor, and $\text{dev}(G)$ is the deviator (trace-free part) of G :

$$\text{dev}(G) = G - \frac{1}{3} \text{tr}(G) I \quad (9)$$

E_3 is the usual specific kinetic energy per unit mass:

$$E_3 = \frac{1}{2} \|\mathbf{v}\|^2 \quad (10)$$

The following forms are taken:

$$\theta_1 = \frac{\tau_1 c_s^2}{3 |A|^{\frac{5}{3}}} \quad (11a)$$

$$\theta_2 = \tau_2 c_t^2 \frac{\rho T_0}{\rho_0 T} \quad (11b)$$

$$\tau_1 = \begin{cases} \frac{6\mu}{\rho_0 c_s^2} & \text{viscous fluids} \\ \tau_0 \left(\frac{\sigma_0}{\|\text{dev}(\sigma)\|_F} \right)^n & \text{elastoplastic solids} \end{cases} \quad (12a)$$

$$\tau_2 = \frac{\rho_0 \kappa}{T_0 c_t^2} \quad (12b)$$

The justification of these choices is that classical Navier–Stokes–Fourier theory is recovered in the stiff limit $\tau_1, \tau_2 \rightarrow 0$ (see [24]). The power law for elastoplastic solids is based on the work [8].

Finally, we have the following relations:

$$\sigma = -\rho c_s^2 G \text{dev}(G) \quad (13a)$$

$$\mathbf{q} = c_t^2 T \mathbf{J} \quad (13b)$$

$$-\frac{\psi}{\theta_1(\tau_1)} = -\frac{3}{\tau_1} |A|^{\frac{5}{3}} A \text{dev}(G) \quad (13c)$$

$$-\frac{\rho \mathbf{H}}{\theta_2(\tau_2)} = -\frac{T \rho_0}{T_0 \tau_2} \mathbf{J} \quad (13d)$$

The following constraint also holds [61]:

$$\det(A) = \frac{\rho}{\rho_0} \quad (14)$$

The GPR model and Godunov and Romenski's 1970s model of elastoplastic deformation in fact relies upon the same equations. The realization of Peshkov and Romenski was that these are the equations of motion for an arbitrary continuum - not just a solid - and so the model can be applied to fluids too. Unlike in previous continuum models, material elements have not only finite size, but also internal structure, encoded in the distortion tensor.

The strain dissipation time τ_1 of the HPR model is a continuous analogue of Frenkel's "particle settled life time" [31]; the characteristic time taken for a particle to move by a distance of the same order of magnitude as the particle's size. Thus, τ_1 characterizes the time taken for a material element to rearrange with its neighbors. $\tau_1 = \infty$ for solids and $\tau_1 = 0$ for inviscid fluids. It is in this way that the HPR model seeks to describe all three major phases of matter, as long as a continuum description is appropriate for the material at hand.

The evolution equation for \mathbf{J} and its contribution to the energy of the system are derived from Romenski's model of hyperbolic heat transfer, originally proposed in [50, 64], and implemented in [62, 63]. In this model, \mathbf{J} is effectively defined as the variable conjugate to the entropy flux, in the sense that the latter is the derivative of the specific internal energy with respect to \mathbf{J} . Romenski remarks that it is more convenient to evolve \mathbf{J} and E than the heat flux or the entropy flux, and thus the equations take the form given here. τ_2 characterizes the speed of relaxation of the thermal impulse due to heat exchange between material elements.

0.4 Numerical Methods

The GPR model, being non-conservative, with stiff source terms, represents a particularly challenging set of PDEs. In this study they are solved by an ADER-WENO method. First, the cell-wise constant state variable data from the current time step is reconstructed using high-order spatial polynomials according to the WENO method. This reconstruction is then extended to a reconstruction in both space and time for each individual cell in the domain, using the Discontinuous Galerkin method. A finite volume solver is then used to couple neighboring cells and produce the cell-wise constant data at the next time step.

0.4.1 The WENO Reconstruction

First introduced by Liu et al. [48] and developed by Jiang and Shu [41], WENO methods are used to produce high order polynomial approximations to piece-wise constant data. Many variations exist. In this study, the method of [28] is used.

Consider the domain $[0, L]$. Take $K, N \in \mathbb{N}$. The order of accuracy of the resulting method will be $N + 1$. Take the set of grid points $x_i = \frac{iL}{K}$ for $i = 0, \dots, K$ and let $\Delta x = \frac{L}{K}$. Denote cell $[x_i, x_{i+1}]$ by C_i . Given cell-wise constant data u on $[0, L]$, an order N polynomial reconstruction of u in C_i will be performed. Define the scaled space variable:

$$\chi^i = \frac{1}{\Delta x} (x - x_i) \quad (15)$$

Denoting the Gauss-Legendre abscissae on $[0, 1]$ by $\{\chi_0, \dots, \chi_N\}$, define the nodal basis of order N : the Lagrange interpolating polynomials $\{\psi_0, \dots, \psi_N\}$ with the following property:

$$\psi_i(\chi_j) = \delta_{ij} \quad (16)$$

If N is even, take the stencils:

$$\begin{cases} S_1 &= \{C_{i-\frac{N}{2}}, \dots, C_{i+\frac{N}{2}}\} \\ S_2 &= \{C_{i-N}, \dots, C_i\} \\ S_3 &= \{C_i, \dots, C_{i+N}\} \end{cases} \quad (17)$$

If N is odd, take the stencils:

$$\begin{cases} S_1 &= \{C_{i-\lfloor \frac{N}{2} \rfloor}, \dots, C_{i+\lceil \frac{N}{2} \rceil}\} \\ S_2 &= \{C_{i-\lceil \frac{N}{2} \rceil}, \dots, C_{i+\lfloor \frac{N}{2} \rfloor}\} \\ S_3 &= \{C_{i-N}, \dots, C_i\} \\ S_4 &= \{C_i, \dots, C_{i+N}\} \end{cases} \quad (18)$$

The data is reconstructed on S_j as:

$$\sum_p \psi_p(\chi^i(x)) \hat{w}_p^{ij} \quad (19)$$

where the \hat{w}_p^{ij} are solutions to the following linear system:

$$\frac{1}{\Delta x} \int_{x_k}^{x_{k+1}} \sum_p \psi_p(\chi^k(x)) \hat{w}_p^{ij} dx = u_k \quad \forall C_k \in S_j \quad (20)$$

where u_k is the value of u in C_k . This can be written as $M_j \hat{\mathbf{w}}^{ij} = \mathbf{u}_{[j_0:j_N]}$ where $\{j_0, \dots, j_N\}$ indexes the cells in S_j . In this study reconstructions with $N = 2$ are used. The matrices of these linear systems and their inverses are precomputed to accelerate the solution of these systems.

Define the oscillation indicator matrix:

$$\Sigma_{mn} = \sum_{\alpha=1}^N \int_0^1 \psi_m^{(\alpha)} \psi_n^{(\alpha)} d\chi \quad (21)$$

and the oscillation indicator for each stencil:

$$o_j = \Sigma_{mn} \hat{w}_m^{ij} \hat{w}_n^{ij} \quad (22)$$

The full reconstruction in C_i is:

$$w_i(x) = \sum_p \psi_p(\chi^i(x)) \bar{w}_p^i \quad (23)$$

where $\bar{w}_p^i = \omega_j \hat{w}_p^{ij}$ is the weighted coefficient of the p th basis function, with weights:

$$\omega_j = \frac{\tilde{\omega}_j}{\sum_k \tilde{\omega}_k} \quad \tilde{\omega}_j = \frac{\zeta_j}{(o_j + \varepsilon)^r} \quad (24)$$

In this study, $r = 8$, $\varepsilon = 10^{-14}$, $\zeta_j = 10^5$ if S_j is a central stencil, and $\zeta_j = 1$ if S_j is a side stencil, as in [23].

The reconstruction can be extended to two dimensions by taking:

$$v^i = \frac{1}{\Delta y} (y - y_i) \quad (25)$$

and defining stencils in the y-axis in an analogous manner. The data in C_i is then reconstructed using stencil S_j as:

$$\sum_{p,q} \psi_p \left(\chi^i(x) \right) \psi_q \left(v^i(x) \right) \tilde{w}_{pq}^{ij} \quad (26)$$

where the coefficients of the weighted 1D reconstruction are used as cell averages:

$$M_j \tilde{w}_p^{ij} = \bar{w}_p^{[j_0:j_N]} \quad \forall p \in \{0, \dots, N\} \quad (27)$$

The oscillation indicator is calculated for each p in the same manner as the 1D case. The reconstruction method is easily further extensible to three dimensions, now using the coefficients \bar{w}_{pq} of the weighted 2D reconstruction as cell averages.

0.4.2 The Galerkin Predictor

Take a non-conservative, hyperbolic system of the form:

$$\frac{\partial \mathbf{Q}}{\partial t} + \frac{\partial \mathbf{F}(\mathbf{Q})}{\partial x} + \mathbf{B}(\mathbf{Q}) \cdot \frac{\partial \mathbf{Q}}{\partial x} = \mathbf{S}(\mathbf{Q}) \quad (28)$$

where \mathbf{Q} is the vector of conserved variables, \mathbf{F} is the conservative nonlinear flux, \mathbf{B} is the block matrix corresponding to the purely non-conservative component of the system, and $\mathbf{S}(\mathbf{Q})$ is the algebraic source vector.

Take the grid for the previous section, and time steps $t_0 < t_1 < \dots$ while defining $\Delta t_n = t_{n+1} - t_n$. Combining the techniques presented in [21, 23], the Discontinuous Galerkin method produces at each time step t_n a local polynomial approximation to \mathbf{Q} on each space-time cell $C_i \times [t_n, t_{n+1}]$.

Now define the scaled time variable:

$$\tau^n = \frac{1}{\Delta t_n} (t - t_n) \quad (29)$$

Thus, (28) becomes:

$$\frac{\partial \mathbf{Q}}{\partial \tau^n} + \frac{\partial \mathbf{F}^*(\mathbf{Q})}{\partial \chi^i} + \mathbf{B}^*(\mathbf{Q}) \cdot \frac{\partial \mathbf{Q}}{\partial \chi^i} = \mathbf{S}^*(\mathbf{Q}) \quad (30)$$

where

$$\mathbf{F}^* = \frac{\Delta t_n}{\Delta x} \mathbf{F} \quad B^* = \frac{\Delta t_n}{\Delta x} B \quad \mathbf{S}^* = \Delta t_n \mathbf{S} \quad (31)$$

The non-dimensionalization notation and spacetime cell indexing notation will be dropped for simplicity in what follows. Now define the set of spatio-temporal basis functions:

$$\{\theta_k(\chi, \tau)\} = \{\psi_p(\chi) \psi_s(\tau) : 0 \leq p, s \leq N\} \quad (32)$$

Denoting the Galerkin predictor by \mathbf{q} , take the following set of approximations:

$$\mathbf{Q} \approx \mathbf{q} = \theta_\beta \mathbf{q}_\beta \quad (33a)$$

$$\mathbf{F}(\mathbf{Q}) \approx \theta_\beta \mathbf{F}_\beta \quad (33b)$$

$$B(\mathbf{Q}) \cdot \frac{\partial \mathbf{Q}}{\partial \chi} \approx \theta_\beta \mathbf{B}_\beta \quad (33c)$$

$$\mathbf{S}(\mathbf{Q}) \approx \theta_\beta \mathbf{S}_\beta \quad (33d)$$

for some coefficients $\mathbf{q}_\beta, \mathbf{F}_\beta, \mathbf{B}_\beta, \mathbf{S}_\beta$.

If $\{\psi_0, \dots, \psi_N\}$ is a nodal basis, the *nodal basis representation* may be used:

$$\mathbf{F}_\beta = \mathbf{F}(\mathbf{q}_\beta) \quad (34a)$$

$$\mathbf{B}_\beta = B(\mathbf{q}_\beta) \cdot \left(\frac{\partial \theta_\gamma(\chi_\beta, \tau_\beta)}{\partial \chi} \mathbf{q}_\gamma \right) \quad (34b)$$

$$\mathbf{S}_\beta = \mathbf{S}(\mathbf{q}_\beta) \quad (34c)$$

where (χ_β, τ_β) are the coordinates of the node corresponding to basis function θ_β .

If a modal basis is used, $\mathbf{F}_\beta, \mathbf{B}_\beta, \mathbf{S}_\beta$ may be found from the previous values of \mathbf{q}_β in the iterative processes described below.

For functions $f(\chi, \tau) = f_\chi(\chi) f_\tau(\tau)$ and $g(\chi, \tau) = g_\chi(\chi) g_\tau(\tau)$, define the following integral operators:

$$[f, g]^t = f_\tau(t) g_\tau(t) \langle f_\chi, g_\chi \rangle \quad (35a)$$

$$\{f, g\} = \langle f_\tau, g_\tau \rangle \langle f_\chi, g_\chi \rangle \quad (35b)$$

Multiplying (30) by test function θ_α , using the polynomial approximations for Q, F, B, S , and integrating over space and time gives:

$$\left\{ \theta_\alpha, \frac{\partial \theta_\beta}{\partial \tau} \right\} \mathbf{q}_\beta = - \left\{ \theta_\alpha, \frac{\partial \theta_\beta}{\partial \chi} \right\} \mathbf{F}_\beta + \{ \theta_\alpha, \theta_\beta \} (\mathbf{S}_\beta - \mathbf{B}_\beta) \quad (36)$$

0.4.2.1 The Discontinuous Galerkin Method

This method of computing the Galerkin predictor allows solutions to be discontinuous at temporal cell boundaries, and is also suitable for stiff source terms.

Integrating (36) by parts in time gives:

$$\begin{aligned} \left([\theta_\alpha, \theta_\beta]^1 - \left\{ \frac{\partial \theta_\alpha}{\partial \tau}, \theta_\beta \right\} \right) \mathbf{q}_\beta &= [\theta_\alpha, \mathbf{w}]^0 - \left\{ \theta_\alpha, \frac{\partial \theta_\beta}{\partial \chi} \right\} \mathbf{F}_\beta \\ &\quad + \{ \theta_\alpha, \theta_\beta \} (\mathbf{S}_\beta - \mathbf{B}_\beta) \end{aligned} \quad (37)$$

where \mathbf{w} is the reconstruction obtained at the start of the time step with the WENO method. Define the following:

$$U_{\alpha\beta} = [\theta_\alpha, \theta_\beta]^1 - \left\{ \frac{\partial \theta_\alpha}{\partial \tau}, \theta_\beta \right\} \quad (38a)$$

$$V_{\alpha\beta} = \left\{ \theta_\alpha, \frac{\partial \theta_\beta}{\partial \chi} \right\} \quad (38b)$$

$$\mathbf{W}_\alpha = [\theta_\alpha, \psi_\gamma]^0 \mathbf{w}_\gamma \quad (38c)$$

$$Z_{\alpha\beta} = \{ \theta_\alpha, \theta_\beta \} \quad (38d)$$

Thus:

$$U_{\alpha\beta} \mathbf{q}_\beta = \mathbf{W}_\alpha - V_{\alpha\beta} \mathbf{F}_\beta + Z_{\alpha\beta} (\mathbf{S}_\beta - \mathbf{B}_\beta) \quad (39)$$

This nonlinear system in \mathbf{q}_β is solved by a Newton method. The source terms must be solved implicitly if they are stiff. Note that \mathbf{W} has no dependence on \mathbf{q} .

0.4.2.2 The Continuous Galerkin Method

This method of computing the Galerkin predictor is not suitable for stiff source terms, but it provides substantial savings on computational cost and ensures continuity across temporal cell boundaries.

$\{\psi_0, \dots, \psi_N\}$ must be chosen in such a way that the first $N + 1$ elements of $\{\theta_\beta\}$ have only a spatial dependence. The first $N + 1$ elements of \mathbf{q} are then fixed by demanding continuity at $\tau = 0$:

$$\mathbf{q}(\chi, 0) = \mathbf{w}(\chi) \quad (40)$$

where \mathbf{w} is spatial the reconstruction obtained at the start of the time step with the WENO method.

For a given vector $\mathbf{v} \in \mathbb{R}^{(N+1)^2}$ and matrix $X \in M_{(N+1)^2, (N+1)^2}(\mathbb{R})$, let $\mathbf{v} = (\mathbf{v}^0, \mathbf{v}^1)$ and $X = \begin{pmatrix} X^{00} & X^{01} \\ X^{10} & X^{11} \end{pmatrix}$ where \mathbf{v}^0, X^{00} are the components relating solely to the first $N + 1$ components of \mathbf{v} . We only need to find the latter components of \mathbf{q} , and thus, from (36), we have:

$$\begin{aligned} \left\{ \theta_\alpha, \frac{\partial \theta_\beta}{\partial \tau} \right\}^{11} \mathbf{q}_\beta^1 &= \{\theta_\alpha, \theta_\beta\}^{11} (\mathbf{S}_\beta^1 - \mathbf{B}_\beta^1) - \left\{ \theta_\alpha, \frac{\partial \theta_\beta}{\partial \chi} \right\}^{11} \mathbf{F}_\beta^1 \\ &+ \{\theta_\alpha, \theta_\beta\}^{10} (\mathbf{S}_\beta^0 - \mathbf{B}_\beta^0) - \left\{ \theta_\alpha, \frac{\partial \theta_\beta}{\partial \chi} \right\}^{10} \mathbf{F}_\beta^0 \end{aligned} \quad (41)$$

Define the following:

$$U_{\alpha\beta} = \left\{ \theta_\alpha, \frac{\partial \theta_\beta}{\partial \tau} \right\}^{11} \quad (42a)$$

$$V_{\alpha\beta} = \left\{ \theta_\alpha, \frac{\partial \theta_\beta}{\partial \chi} \right\}^{11} \quad (42b)$$

$$\mathbf{W}_\alpha = \{\theta_\alpha, \theta_\beta\}^{10} (\mathbf{S}_\beta - \mathbf{B}_\beta)^0 - \left\{ \theta_\alpha, \frac{\partial \theta_\beta}{\partial \chi} \right\}^{10} \mathbf{F}_\beta^0 \quad (42c)$$

$$Z_{\alpha\beta} = \{\theta_\alpha, \theta_\beta\}^{11} \quad (42d)$$

Thus:

$$U_{\alpha\beta} \mathbf{q}_\beta^1 = \mathbf{W}_\alpha - V_{\alpha\beta} \mathbf{F}_\beta^1 + Z_{\alpha\beta} (\mathbf{S}_\beta^1 - \mathbf{B}_\beta^1) \quad (43)$$

Note that, as with the discontinuous Galerkin method, \mathbf{W} has no dependence on the degrees of freedom in \mathbf{q} .

0.4.3 The Finite Volume Scheme

Following the formulation of [23], integrating (28) over $[t_n, t_{n+1}] \times C_i$ gives:

$$\mathbf{Q}_i^{n+1} = \mathbf{Q}_i^n + \Delta t_n (\mathbf{S}_i^n - \mathbf{P}_i^n) - \frac{\Delta t_n}{\Delta x} (\mathbf{D}_{i+1}^n - \mathbf{D}_i^n) \quad (44)$$

where

$$\mathbf{Q}_i^n = \frac{1}{\Delta x} \int_{x_i}^{x_{i+1}} \mathbf{Q}(x, t_n) dx \quad (45a)$$

$$\mathbf{S}_i^n = \frac{1}{\Delta t_n \Delta x} \int_{t_n}^{t_{n+1}} \int_{x_i}^{x_{i+1}} \mathbf{S}(\mathbf{Q}) dx dt \quad (45b)$$

$$\mathbf{P}_i^n = \frac{1}{\Delta t_n \Delta x} \int_{t_n}^{t_{n+1}} \int_{x_i}^{x_{i+1}} \mathbf{B}(\mathbf{Q}) \cdot \frac{\partial \mathbf{Q}}{\partial x} dx dt \quad (45c)$$

$$\mathbf{D}_i^n = \frac{1}{\Delta t_n} \int_{t_n}^{t_{n+1}} \mathcal{D}(\mathbf{Q}^-(x_i, t), \mathbf{Q}^+(x_i, t)) dt \quad (45d)$$

$\mathbf{Q}^-, \mathbf{Q}^+$ are the left and right extrapolated states at the x_i boundary. $\mathbf{S}_i^n, \mathbf{P}_i^n, \mathbf{D}_i^n$ are calculated using an $N + 1$ -point Gauss-Legendre quadrature, replacing \mathbf{Q} with \mathbf{q}_h .

M , as defined in Section 0.4.2, is a diagonalizable matrix with decomposition $M = R\Lambda R^{-1}$ where the columns of R are the right eigenvectors and Λ is the diagonal matrix of eigenvalues. Define the following matrix:

$$|M| = R |\Lambda| R^{-1} \quad (46)$$

Using these definitions, the interface terms arising in the FV formula have the following form:

$$\mathcal{D}(\mathbf{q}^-, \mathbf{q}^+) = \frac{1}{2} (\mathbf{F}(\mathbf{q}^-) + \mathbf{F}(\mathbf{q}^+) + \hat{B} \cdot (\mathbf{q}^+ - \mathbf{q}^-) - \hat{M} \cdot (\mathbf{q}^+ - \mathbf{q}^-)) \quad (47)$$

\hat{M} is chosen to either correspond to a Rusanov/Lax-Friedrichs flux [69]:

$$\hat{M} = \max \left(\max |\Lambda(\mathbf{q}^-)|, \max |\Lambda(\mathbf{q}^+)| \right) \quad (48)$$

or a Roe flux [26]:

$$\hat{M} = \left| \int_0^1 M(\mathbf{q}^- + z(\mathbf{q}^+ - \mathbf{q}^-)) dz \right| \quad (49)$$

or a simplified Osher–Solomon flux [25]:

$$\hat{M} = \int_0^1 |M(\mathbf{q}^- + z(\mathbf{q}^+ - \mathbf{q}^-))| dz \quad (50)$$

\hat{B} takes the following form:

$$\hat{B} = \int_0^1 B(\mathbf{q}^- + z(\mathbf{q}^+ - \mathbf{q}^-)) dz \quad (51)$$

It was found that the Osher–Solomon flux would often produce slightly less diffusive results, but that it was more computationally expensive, and also had a greater tendency to introduce numerical artifacts.

0.4.4 Time Step and Boundary Conditions

Let Λ_i^n be the set of eigenvalues of the HPR system evaluated at \mathbf{Q}_i^n . $C_{cfl} < 1$ is a constant (usually taken to be 0.9, unless the problem being simulated is particularly demanding, requiring a lower value). A semi-analytic form for Λ is given in Section B.2. The eigenvalues determine the speed of propagation of information in the solution to the Riemann Problem at the cell interfaces, and the time step is chosen to ensure that the characteristics do not enter into other cells between t_n and t_{n+1} :

$$\Delta t_n = \frac{C_{cfl} \cdot \Delta x}{\max_i |\Lambda_i^n|} \quad (52)$$

Transmissive boundary conditions (allowing material and heat to pass through) are implemented by setting the state variables in the boundary cells to the same value as their non-boundary neighbors. Reflective boundary conditions are implemented in the same way, except that the directions of the velocity and thermal impulse vectors in the boundary cells are reversed.

Chapter 1

Objective 1: Extending the GPR Model

1.1 Equations of State

1.1.1 Mie-Gruneisen Models

It is required to specify the microscale energy E_1 appearing in (6). In this study, several different possible choices for E_1 are put into the same framework by expressing them in the following Mie-Gruneisen form [52]:

$$E_1(\rho, p) = e(\rho, p) = e^{ref}(\rho) + \frac{p - p^{ref}(\rho)}{\rho\Gamma(\rho)} \quad (1.1a)$$

$$T = T^{ref}\phi(\rho) + \frac{e - e^{ref}}{c_v} = T^{ref}\phi(\rho) + \frac{p - p^{ref}(\rho)}{c_v\rho\Gamma(\rho)} \quad (1.1b)$$

$$\phi(\rho) = \exp\left(\int_{\rho_0}^{\rho} \frac{\Gamma(\rho')}{\rho'} d\rho'\right) \quad (1.1c)$$

The forms taken by e^{ref} , p^{ref} , Γ for various different instances of this class are given in Table 1.1 on page 15. The first five entries in the table are standard results. The sixth is derived thus. The Godunov-Romenski hyperelastic EOS is given by:

$$E(\rho, S, A) = \frac{c_0^2}{2\alpha^2} \left(|A^T A|^{\alpha/2} - 1 \right)^2 + c_v T_0 |A^T A|^{\gamma/2} (e^{S/c_v} - 1) + \frac{b_0^2}{4} |A^T A|^{\beta/2} \|\text{dev}(A^T A)\|^2 \quad (1.2)$$

Using the relation $\det(A) = \frac{\rho}{\rho_0}$, this can be thought of as taking the form:

$$E_1(\rho, s) + \frac{c_s(\rho)^2}{4} \|\text{dev}(G)\|_F^2 \quad (1.3)$$

where $c_s = b_0 \left(\frac{\rho}{\rho_0}\right)^\beta$. Considering only the microscale energy component, note that we have:

$$p = \rho^2 \frac{\partial E_1}{\partial \rho} = \rho \left(\frac{c_0^2}{\alpha} \left(\left(\frac{\rho}{\rho_0} \right)^\alpha - 1 \right) \left(\frac{\rho}{\rho_0} \right)^\alpha + \gamma c_v T_0 \left(\frac{\rho}{\rho_0} \right)^\gamma (e^{S/c_v} - 1) \right) \quad (1.4)$$

Therefore:

$$E_1 - \frac{c_0^2}{2\alpha^2} \left(\left(\frac{\rho}{\rho_0} \right)^\alpha - 1 \right)^2 = \frac{p}{\gamma\rho} - \frac{c_0^2}{\gamma\alpha} \left(\left(\frac{\rho}{\rho_0} \right)^\alpha - 1 \right) \left(\frac{\rho}{\rho_0} \right)^\alpha \quad (1.5)$$

Thus E_1 can be put in Mie-Gruneisen form:

$$E_1 = \frac{p - \frac{c_0^2\rho}{\alpha} \left(\left(\frac{\rho}{\rho_0} \right)^\alpha - 1 \right) \left(\frac{\rho}{\rho_0} \right)^\alpha}{\gamma\rho} + \frac{c_0^2}{2\alpha^2} \left(\left(\frac{\rho}{\rho_0} \right)^\alpha - 1 \right)^2 \quad (1.6)$$

The following quantities are required when computing the eigenstructure of the system:

$$\frac{\partial T}{\partial \rho} = \frac{1}{c_v} \left(\frac{\partial e}{\partial \rho} - \frac{de^{ref}}{d\rho} \right) \quad (1.7a)$$

$$\frac{\partial T}{\partial p} = \frac{1}{c_v} \frac{\partial e}{\partial p} \quad (1.7b)$$

$$\frac{\partial e}{\partial \rho} = \frac{de^{ref}}{d\rho} - \frac{\frac{dp^{ref}}{d\rho} \rho \Gamma(\rho) + (\Gamma(\rho) + \rho \Gamma'(\rho)) (p - p^{ref}(\rho))}{(\rho \Gamma(\rho))^2} \quad (1.8a)$$

$$\frac{\partial e}{\partial p} = \frac{1}{\rho \Gamma(\rho)} \quad (1.8b)$$

The relevant functions for each of the EOSs used in this study are given in Table 1.2 on page 16.

Although this is a versatile class of equations of state - and it is fit for the purposes that the model is put to here - it should be noted that many other choices are available.

1.1.2 Variable Transverse Perturbation Speed

Taking (1.1a) and using the fact that $p = \rho^2 e_\rho$, we have:

$$e_\rho - \frac{\Gamma}{\rho} e = \frac{p^{ref}}{\rho^2} - \frac{\Gamma}{\rho} e^{ref} \quad (1.9)$$

Equation of State	$p^{ref}(\rho)$	$e^{ref}(\rho)$	$\Gamma(\rho)$	T^{ref}
Ideal Gas	0	0	$\gamma - 1$	0
Stiffened Gas	$-p_\infty$	$\frac{p_\infty}{\rho}$	$\gamma - 1$	0
Shock Mie-Gruneisen	$\frac{c_0^2 \left(\frac{1}{\rho_0} - \frac{1}{\rho} \right)^2}{\left(\frac{1}{\rho_0} - s \left(\frac{1}{\rho_0} - \frac{1}{\rho} \right) \right)^2}$	$\frac{p^{ref}}{2} \left(\frac{1}{\rho_0} - \frac{1}{\rho} \right)$	$\Gamma_0 \frac{\rho_0}{\rho}$	0
JWL	$A e^{-\frac{R_1 \rho_0}{\rho}} + B e^{-\frac{R_2 \rho_0}{\rho}}$	$\frac{A}{\rho_0 R_1} e^{-\frac{R_1 \rho_0}{\rho}} + \frac{B}{\rho_0 R_2} e^{-\frac{R_2 \rho_0}{\rho}}$	Γ_0	0
Cochran-Chan	$A \left(\frac{\rho}{\rho_0} \right)^{\epsilon_1} - B \left(\frac{\rho}{\rho_0} \right)^{\epsilon_2}$	$\frac{A}{\rho_0 (\epsilon_1 - 1)} \left(\left(\frac{\rho}{\rho_0} \right)^{\epsilon_1 - 1} - 1 \right) - \frac{B}{\rho_0 (\epsilon_2 - 1)} \left(\left(\frac{\rho}{\rho_0} \right)^{\epsilon_2 - 1} - 1 \right)$	Γ_0	0
Godunov-Romenski	$\frac{c_0^2 \rho}{\alpha} \left(\left(\frac{\rho}{\rho_0} \right)^\alpha - 1 \right) \left(\frac{\rho}{\rho_0} \right)^\alpha$	$\frac{c_0^2}{2\alpha^2} \left(\left(\frac{\rho}{\rho_0} \right)^\alpha - 1 \right)^2$	γ	T_0

Table 1.1: e^{ref} , p^{ref} , Γ , T_{ref} for different kinds of Mie-Gruneisen equations of state

Equation of State	$\frac{dp^{ref}}{d\rho}$	$\frac{de^{ref}}{d\rho}$	$\Gamma'(\rho)$
Ideal Gas	0	0	0
Stiffened Gas	0	$-\frac{p_\infty}{\rho^2}$	0
Shock Mie-Gruneisen	$\frac{c_0^2 \rho_0^2 (s(\rho_0 - \rho) - \rho)}{(s(\rho - \rho_0) - \rho)^3}$	$\frac{1}{2} \left(\frac{dp^{ref}}{d\rho} \left(\frac{1}{\rho_0} - \frac{1}{\rho} \right) + \frac{p^{ref}}{\rho^2} \right)$	$-\Gamma_0 \frac{\rho_0}{\rho^2}$
JWL	$\frac{AR_1 \rho_0}{\rho^2} e^{-\frac{R_1 \rho_0}{\rho}} + \frac{BR_2 \rho_0}{\rho^2} e^{-\frac{R_2 \rho_0}{\rho}}$	$\frac{A}{\rho^2} e^{-\frac{R_1 \rho_0}{\rho}} + \frac{B}{\rho^2} e^{-\frac{R_2 \rho_0}{\rho}}$	0
Cochran-Chan	$\frac{\epsilon_1 A}{\rho} \left(\frac{\rho}{\rho_0} \right)^{\epsilon_1} - \frac{\epsilon_2 B}{\rho} \left(\frac{\rho}{\rho_0} \right)^{\epsilon_2}$	$\frac{A}{\rho^2} \left(\frac{\rho}{\rho_0} \right)^{\epsilon_1} - \frac{B}{\rho^2} \left(\frac{\rho}{\rho_0} \right)^{\epsilon_2}$	0
Godunov-Romenski			0

Table 1.2: $\frac{dp^{ref}}{d\rho}$, $\frac{de^{ref}}{d\rho}$, Γ' for different kinds of Mie-Gruneisen equations of state

1.1 Equations of State

The solutions to this equation for different forms of Γ, p^{ref}, e^{ref} take the form below, where f is an arbitrary function of s , g depends on the form of Γ , and \hat{e} is a particular solution of the equation (which will be equal to e^{ref} if $p^{ref} = \rho^2 \frac{\partial e^{ref}}{\partial \rho}$).

$$e = f(s) g(\rho) + \hat{e}(\rho) \quad (1.10)$$

We have:

$$p = \rho^2 e_\rho = \rho^2 \left(f(s) g'(\rho) + \hat{e}'(\rho) \right) \quad (1.11)$$

Thus:

$$\frac{\frac{p}{\rho^2} - \hat{e}'(\rho)}{g'(\rho)} = f(s) = \frac{e - \hat{e}(\rho)}{g(\rho)} \quad (1.12)$$

Therefore:

$$E_1(\rho, p) = e(\rho, p) = \hat{e}(\rho) + \frac{g(\rho)}{g'(\rho)} \left(\frac{p}{\rho^2} - \hat{e}'(\rho) \right) \quad (1.13)$$

We now add another term to the energy, giving it the following form:

$$E(\rho, p) = e(\rho, p) = f(s) g(\rho) + \hat{e}(\rho) + B(\rho) h(A) \quad (1.14)$$

We then have:

$$p = \rho^2 \left(f(s) g'(\rho) + \hat{e}'(\rho) + B'(\rho) h(A) \right) \quad (1.15)$$

Thus:

$$\frac{\frac{p}{\rho^2} - \hat{e}'(\rho) - B'(\rho) h(A)}{g'(\rho)} = f(s) = \frac{e - \hat{e}(\rho) - B(\rho) h(A)}{g(\rho)} \quad (1.16)$$

Therefore:

$$e = \frac{g(\rho)}{g'(\rho)} \left(\frac{p}{\rho^2} - \hat{e}'(\rho) - B'(\rho) h(A) \right) + \hat{e}(\rho) + B(\rho) h(A) \quad (1.17)$$

Noting that $\frac{g(\rho)}{g'(\rho)} = \frac{\rho}{\Gamma(\rho)}$, this can be expressed as:

$$E(\rho, p) = e(\rho, p) = E_1(\rho, p) + \left(B(\rho) - \frac{\rho}{\Gamma(\rho)} B'(\rho) \right) h(A) \quad (1.18)$$

If the EOS comprises a microscale energy component of Mie-Gruneisen type, and a mesoscale energy component with speed of transverse vibrations dependent upon ρ , then this provides a method to recover the EOS in terms of ρ and p (by substituting $B(\rho) = \frac{c_s^2(\rho)}{4}$ and $h(A) = \|\text{dev}(A^T A)\|_F^2$).

1.2 Multiphase Reactive Materials

1.2.1 Extended Model

We now wish to simulate the mixture of two miscible materials, labelled 1 and 2. Let λ be the mass fraction of material 1. Let material 1 undergo a chemical reaction at rate K to form material 2. The GPR model can be extended to incorporate these factors thus:

$$\frac{\partial \rho}{\partial t} + \frac{\partial (\rho v_k)}{\partial x_k} = 0 \quad (1.19a)$$

$$\frac{\partial (\rho v_i)}{\partial t} + \frac{\partial (\rho v_i v_k + p \delta_{ik} - \sigma_{ik})}{\partial x_k} = 0 \quad (1.19b)$$

$$\frac{\partial A_{ij}}{\partial t} + \frac{\partial (A_{ik} v_k)}{\partial x_j} + v_k \left(\frac{\partial A_{ij}}{\partial x_k} - \frac{\partial A_{ik}}{\partial x_j} \right) = -\frac{\psi_{ij}}{\theta_1(\tau_1)} \quad (1.19c)$$

$$\frac{\partial (\rho J_i)}{\partial t} + \frac{\partial (\rho J_i v_k + T \delta_{ik})}{\partial x_k} = -\frac{\rho H_i}{\theta_2(\tau_2)} \quad (1.19d)$$

$$\frac{\partial (\rho E)}{\partial t} + \frac{\partial (\rho E v_k + (p \delta_{ik} - \sigma_{ik}) v_i + q_k)}{\partial x_k} = 0 \quad (1.19e)$$

$$\frac{\partial (\rho \lambda)}{\partial t} + \frac{\partial (\rho \lambda v_k)}{\partial x_k} = -\rho K \quad (1.19f)$$

K is the rate of reaction - a function of T and λ , whose form depends on the type of reaction kinetics used. The EOS is modified to include:

$$E_r(\lambda) = -Q_c(1 - \lambda) \quad (1.20)$$

1.2.2 Mixture Rules

Pressure and thermal equilibrium are assumed between the two materials. Note that we have:

$$\frac{1}{\rho} = \frac{\lambda}{\rho_1} + \frac{1-\lambda}{\rho_2} \quad (1.21)$$

$$e = \lambda e_1 + (1-\lambda) e_2 \quad (1.22)$$

The pressure equilibrium assumption gives:

$$\begin{aligned} p &= p_1^{ref} + \rho_1 \Gamma_1 (e_1 - e_1^{ref}) \\ &= p_2^{ref} + \rho_2 \Gamma_2 (e_2 - e_2^{ref}) \end{aligned} \quad (1.23)$$

Thus, the energy equation becomes:

$$e = \lambda \left(e_1^{ref} + \frac{p - p_1^{ref}}{\rho_1 \Gamma_1} \right) + (1-\lambda) \left(e_2^{ref} + \frac{p - p_2^{ref}}{\rho_2 \Gamma_2} \right) \quad (1.24)$$

The temperature equilibrium assumption gives:

$$T_1^{ref} \phi_1 + \frac{p - p_1^{ref}}{\rho_1 \Gamma_1 (c_v)_1} = T_2^{ref} \phi_2 + \frac{p - p_2^{ref}}{\rho_2 \Gamma_2 (c_v)_2} \quad (1.25)$$

Temperature and pressure of the mixture are required by the evolution equations. They are obtained by solving numerically the nonlinear system of algebraic equations given by (1.21), (1.24), (1.25) to first find $\rho_1, \rho_2 e_1, e_2$, and then substituting them in (1.23) and (1.25).

As, under the GPR model, the viscosity and thermal conductivity of a fluid govern the stiffness of the source terms, it is required to use a mixture model to calculate these quantities under the multiphase GPR model. Many mixture models have been proposed (e.g. see early simpler examples in [34, 37], or see [35] for a review of later, more complex models). In this study, we chose the first mixture rule presented in [2], which is based on Wilke's mixing rule (see [72]), coupled with curve fits from [12] and Eucken's Law. The model is chosen for its balance

1.2 Multiphase Reactive Materials

between expressiveness and simplicity. The viscosity and thermal conductivity of the mixture are calculated thus:

$$\mu = \frac{x\mu_1}{\phi_1} + \frac{(1-x)\mu_2}{\phi_2} \quad (1.26a)$$

$$\kappa = \frac{x\kappa_1}{\phi_1} + \frac{(1-x)\kappa_2}{\phi_2} \quad (1.26b)$$

$$\phi_1 = x + (1-x) \frac{\sqrt{1-\lambda} \left(1 + \sqrt{\frac{\mu_1}{\mu_2}} \left(\frac{1-\lambda}{\lambda}\right)^{\frac{1}{4}}\right)^2}{\sqrt{8}} \quad (1.26c)$$

$$\phi_2 = x \frac{\sqrt{\lambda} \left(1 + \sqrt{\frac{\mu_2}{\mu_1}} \left(\frac{\lambda}{1-\lambda}\right)^{\frac{1}{4}}\right)^2}{\sqrt{8}} + (1-x) \quad (1.26d)$$

where x is the molar fraction of material 1:

$$x = \frac{\frac{\rho_1}{M_1}}{\frac{\rho_1}{M_1} + \frac{\rho_2}{M_2}} \quad (1.27)$$

where M_1, M_2 are the molar masses of materials 1 and 2, respectively.

The speed of sound in the mixture is given by:

$$\begin{aligned} c_0 &= \sqrt{\left. \frac{\partial p}{\partial \rho} \right|_s} \\ &= \sqrt{\frac{\frac{p}{\rho^2} - \left. \frac{\partial e}{\partial \rho} \right|_p}{\left. \frac{\partial e}{\partial p} \right|_\rho}} \end{aligned} \quad (1.28)$$

Note that we have:

$$\frac{\partial e}{\partial p} = \lambda \frac{\partial e_1}{\partial p} + (1-\lambda) \frac{\partial e_2}{\partial p} \quad (1.29a)$$

$$\frac{\partial e}{\partial \rho} = \lambda \frac{\partial e_1}{\partial \rho_1} \frac{\partial \rho_1}{\partial \rho} + (1-\lambda) \frac{\partial e_2}{\partial \rho_2} \frac{\partial \rho_2}{\partial \rho} \quad (1.29b)$$

To find $\frac{\partial \rho_1}{\partial \rho}$, $\frac{\partial \rho_2}{\partial \rho}$, we differentiate (1.21) and (1.25) with respect to ρ , to obtain:

$$\frac{\lambda}{\rho_1^2} \frac{\partial \rho_1}{\partial \rho} + \frac{1-\lambda}{\rho_2^2} \frac{\partial \rho_2}{\partial \rho} = \frac{1}{\rho^2} \quad (1.30a)$$

$$\frac{\partial T_1}{\partial \rho_1} \frac{\partial \rho_1}{\partial \rho} - \frac{\partial T_2}{\partial \rho_2} \frac{\partial \rho_2}{\partial \rho} = 0 \quad (1.30b)$$

Thus:

$$\frac{\partial \rho_1}{\partial \rho} = \frac{1}{\rho^2} \cdot \frac{1}{\frac{\lambda}{\rho_1^2} \frac{\partial T_2}{\partial \rho_2} + \frac{1-\lambda}{\rho_2^2} \frac{\partial T_1}{\partial \rho_1}} \frac{\partial T_2}{\partial \rho_2} \quad (1.31a)$$

$$\frac{\partial \rho_2}{\partial \rho} = \frac{1}{\rho^2} \cdot \frac{1}{\frac{\lambda}{\rho_1^2} \frac{\partial T_2}{\partial \rho_2} + \frac{1-\lambda}{\rho_2^2} \frac{\partial T_1}{\partial \rho_1}} \frac{\partial T_1}{\partial \rho_1} \quad (1.31b)$$

1.2.3 Reaction Rate Laws

There are many different reaction rate laws that can be used to determine the form of K appearing in (1.19f).

In discrete ignition temperature reaction kinetics, no reaction occurs below the ignition temperature, T_i . Above T_i , the reaction proceeds at a constant rate $K_0 > 0$:

$$K = \begin{cases} K_0 \lambda & T \geq T_i \\ 0 & T < T_i \end{cases} \quad (1.32)$$

A more sophisticated model of reaction kinetics was devised by Svante Arrhenius in 1889 [3, 4]:

$$K = B_c e^{-\frac{E_a}{R_c T}} \lambda \quad (1.33)$$

where B_c is some prefactor (with units of frequency), and E_a is the activation energy of the reactive species.

1.3 Numerical Treatment of Source Terms

Whilst the ADER-WENO method presented in Section 0.4 is capable of solving the extended model of 1.2.1, special consideration needs to be made when solving the model with other methods based on temporal splitting (e.g. [39] - see Section 2.2 for more information). The following ODE needs to be solved in the process:

$$\frac{d\lambda}{dt} = -K \quad (1.34)$$

Following the formulation presented in [REF], we use the following representations:

$$\lambda(t) = \lambda_j \psi_j(t) \quad (1.35a)$$

$$K(t) = K_j \psi_j(t) \quad (1.35b)$$

Thus, multiplying (1.34) by ψ_j and integrating over the time interval, we have:

$$\langle \psi_i, \psi_j' \rangle \lambda_j = -\Delta t \langle \psi_i, \psi_j \rangle K_j \quad (1.36)$$

Using integration by parts, we have:

$$\left(\psi_i(1) \psi_j(1) - \langle \psi_i', \psi_j \rangle \right) \lambda_j = \psi_i(0) \lambda(0) - \Delta t \langle \psi_i, \psi_j \rangle K_j \quad (1.37)$$

As described in 0.4.2.1, the nodal basis representation is used, so that K_j is calculated as $K(\lambda_j)$.

1.4 Numerical Results

1.4.1 Seven-Wave Elastic Riemann Problem

This test is taken from [7]. The aim of the test is to validate the Mie-Gruneisen formulation of the Godunov-Romenski EOS presented in 1.1.1, and the formulation of the mesoscale GPR energy for the Godunov-Romenski EOS presented in 1.1.2.

1.4 Numerical Results

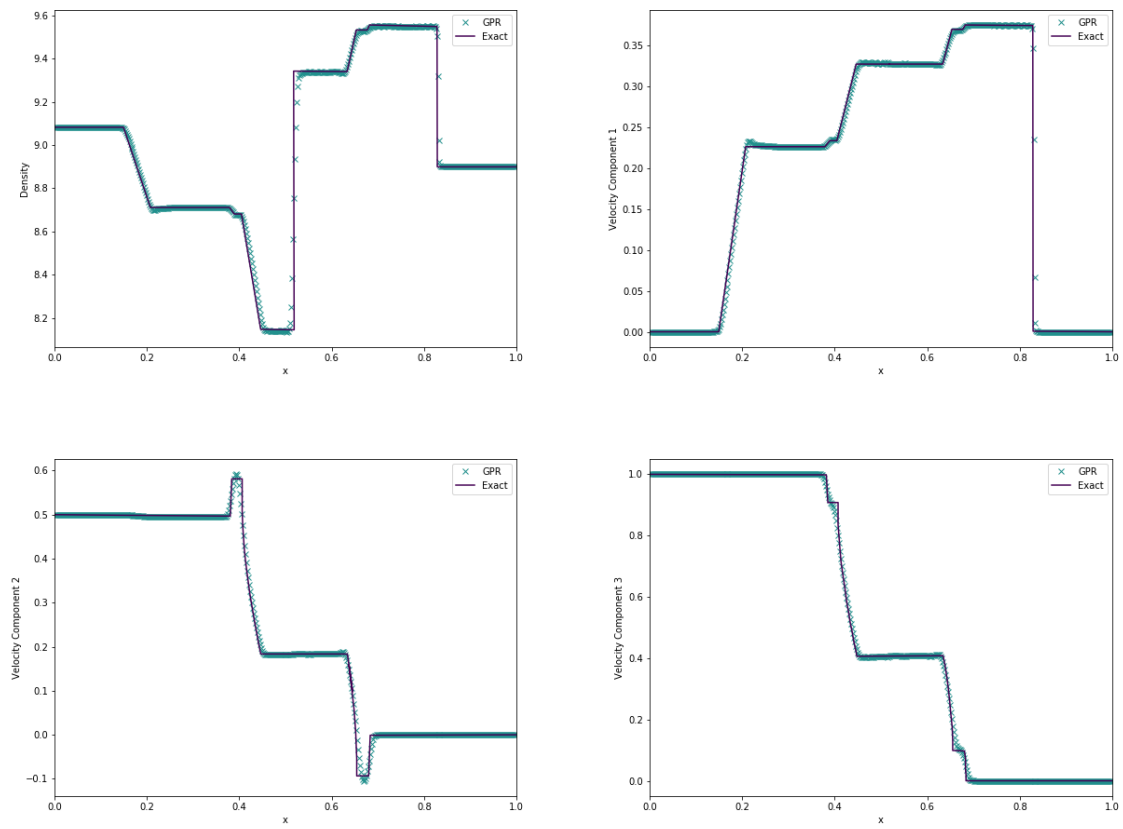


Figure 1.1: Density and velocity for the 7-wave elastic Riemann problem

1.4 Numerical Results

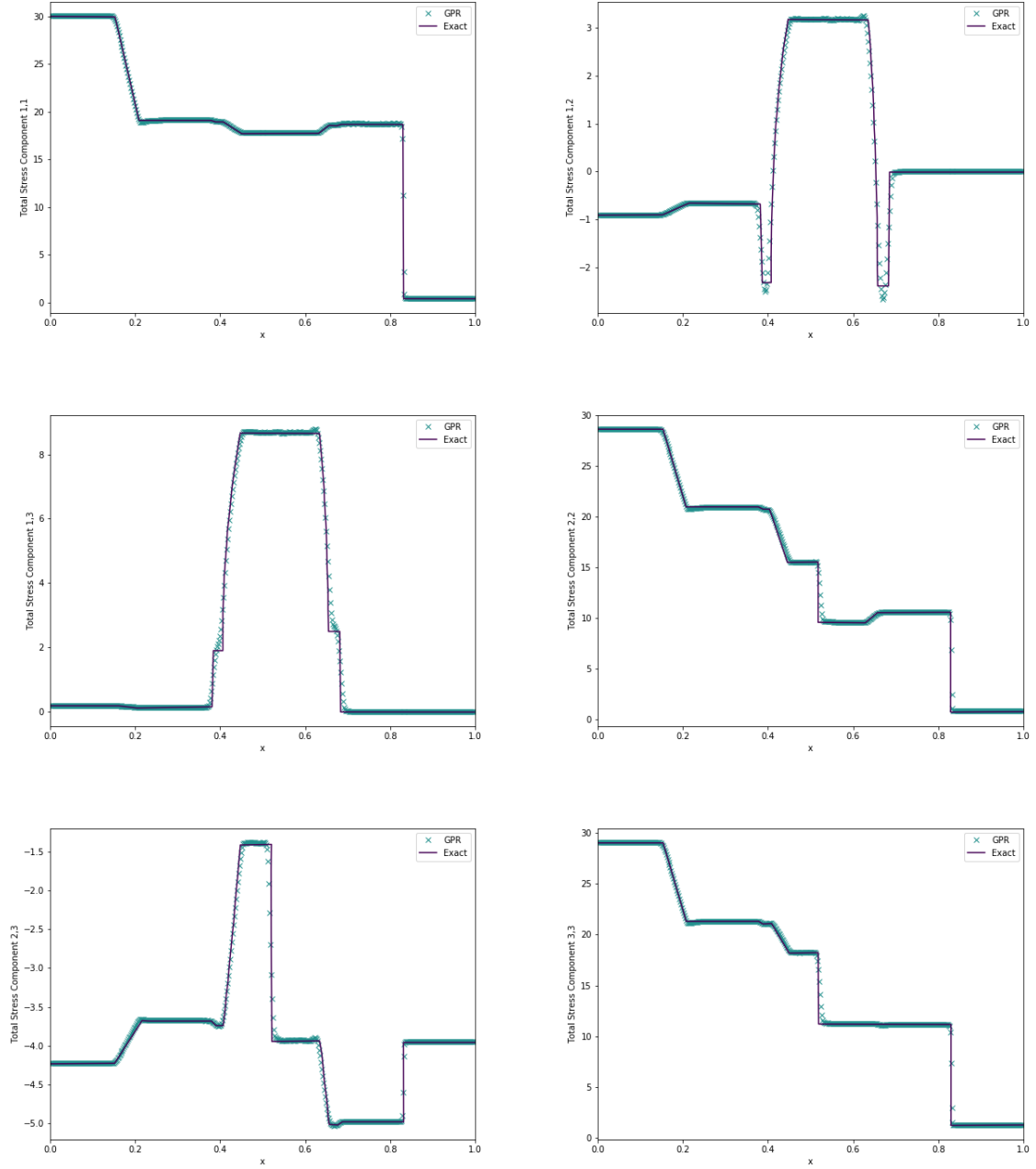


Figure 1.2: Total stress for the 7-wave elastic Riemann problem

	ρ	p	\mathbf{v}	A	\mathbf{J}	λ
$x < 0.25$	1.4	1	$\mathbf{0}$	$\sqrt[3]{1.4} \cdot I_3$	$\mathbf{0}$	0
$x \geq 0.25$	0.887565	0.191709	$(-0.577350, 0, 0)$	$\sqrt[3]{0.887565} \cdot I_3$	$\mathbf{0}$	1

Table 1.3: Initial conditions for the viscous shock-induced detonation test

1.4.2 Shock-Induced Detonation

The GPR model is now combined with discrete ignition temperature reaction kinetics to model a ZND detonation wave¹ in a viscous, reactive, ideal gas. The test consists of a CJ wave with speed 1, traveling into a region of totally unburnt gas. The initial conditions are taken from Helzel et al. [36] and are given in Table 1.3 on page 25.

The material parameters are taken to be: $\gamma = 1.4$, $c_v = 2.5$, $\rho_0 = 1$, $p_0 = 1$, $c_s = 1$, $c_t = 1$, $\mu = 10^{-4}$, $P_r = 0.75$, $Q_c = 1$, $K_0 = 250$, $T_i = 0.25$. The results for grids of 400 and 1600 cells at time $t = 0.5$ are found in Figure 1.3 on page 26. They are to be compared with those by Hidalgo and Dumbser [38]. The simulation with 400 cells corresponds well with that found in [38], and the simulation with 1600 cells is very close to Hidalgo's total variation diminishing reference solution calculated with 10,000 cells.

The von Neumann spike is well resolved, with the thin reaction zone behind it (corresponding to the region in which the concentration decreases from 1 to 0). The CJ state is maintained correctly behind the reaction zone. The spurious wave in the density is explained in [38] as being due to initialisation errors occurring as a result of using exact algebraic conditions for an ideal (infinitely thin) CJ detonation wave, which are solved with a viscous model with finite reaction rate.

1.4.3 Heating-Induced Deflagration

As a step towards modeling the slow cooking off problem, the GPR model is now applied to the situation presented by Clarke, Kassoy and Riley [15–17]. Here, the domain $x \in [0, 8.5 \times 10^{-6}]$

¹Zel'dovich [73], von Neumann [70], and Doring [18] independently proposed this detonation model, whereby reactive gas is compressed to high pressure by an infinitely thin shock wave into a *von Neumann spike*, initiating the reaction. The reaction zone is located behind the spike. In the reference frame of the shock, the gas moves supersonically ahead of the shock, subsonically in the reaction zone, and sonically in the region behind the reaction zone (which is described by the Chapman-Jouget state [14, 43]. The energy released in the reaction is transported acoustically to the shock to support it.

1.4 Numerical Results

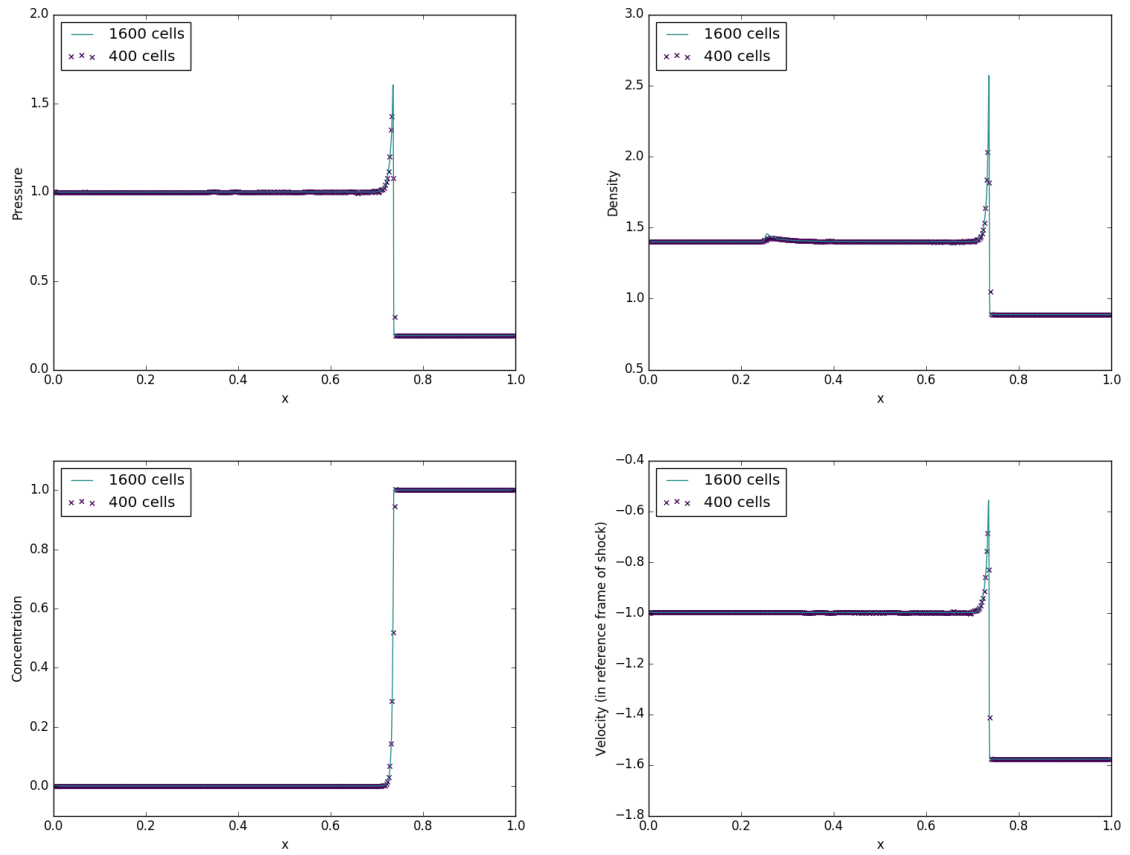


Figure 1.3: Pressure, density, concentration of reactant, and velocity (in the reference frame of the shock) in the viscous shock-induced detonation test

is occupied by an ideal gas with initial conditions $\rho = \rho_0 = 1.176$, $p = p_0 = 101325$, $\mathbf{v} = \mathbf{0}$, $A = I_3$, $\mathbf{J} = \mathbf{0}$ and material parameters $\gamma = 1.4$, $c_v = 718$, $c_s = 55$, $c_t = 500$, $\mu = 1.98 \times 10^{-5}$, $P_r = 0.72$. These values are chosen to be similar to air at room temperature.

Thermal energy is added at the left boundary at a high power of $\frac{\gamma p_0 c_0}{P_r(\gamma-1)}$ (around $1.7 \times 10^8 \text{ W m}^{-2}$). The test is performed with both a combustible and an inert gas. In the former case, the initial concentration is set to $\lambda = 1$. Arrhenius reaction kinetics are used, with $Q_c = 6\gamma c_v T_0$, $B_c = 7 \times 10^{10}$, $\epsilon = \frac{1}{20}$. The subsequent evolutions of the systems for 400 cells are shown in Figure 1.4 on page 28. Nondimensionalised time and length variables t^* , x^* are used, as in [16]:

$$t = \frac{\mu}{p_0 \gamma} t^* \quad (1.38a)$$

$$x = \frac{\mu c_0}{p_0 \gamma} x^* \quad (1.38b)$$

There are no analogues for c_t and c_s in the models used by Clarke et al. c_s is given the experimentally-derived value for CH_3Cl at 30°C given in [24]. c_t is chosen by trial and error so that the GPR results corresponded with those in [16]. The results presented here are thus close, but not identical to those of Clarke et al.

Note that heating the inert gas produces an acoustic wave of constant pressure, propagating ahead of the temperature curve. This pressure wave is also present in the heating of the combustible gas, where it proceeds in front of the combustion wave. The temperature increase accompanying this acoustic wave is not enough to ignite the reactive gas, and the thin reaction zone lags behind the acoustic wavefront. Although the combustion wave is referred to as a detonation wave in [16], it would now commonly be called a deflagration wave, as it travels subsonically and is not coincident with the shock wave. This phenomenon of a second, faster shock overtaking the combustion wave demonstrated experimentally by Kapila et al. [44], with a full mathematical analysis provided by Short [67], where it is shown to result from the steep temperature gradient at the time of ignition.

1.4.4 Heating-Induced Detonation

It is now demonstrated that the heating-induced deflagration test can result in detonation if the temperature gradient upon ignition is less steep. This test is identical to the previous

1.4 Numerical Results

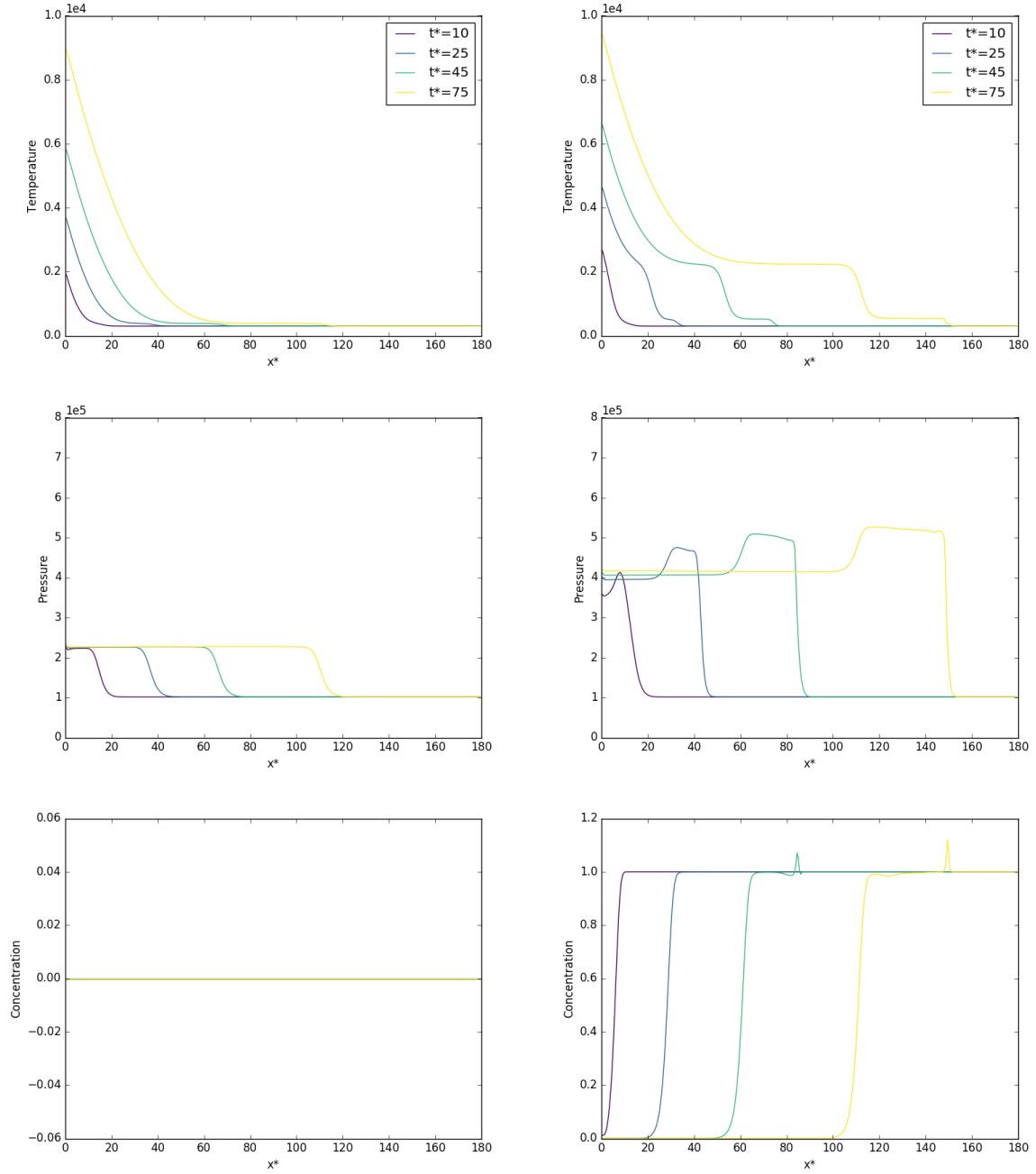


Figure 1.4: Temperature, pressure, and concentration of reactant in the heating-induced deflagration test with inert gas (left) / reactive gas (right)

test, with one exception: ϵ is given the higher value of $\frac{1}{15}$. Thus, the activation energy is effectively lower, or equivalently, the whole gas volume is relatively closer to the ignition temperature when the gas at the left boundary ignites. The results of this test are shown in Figure 1.5 on page 30.

The von Neumann spike is present and well resolved, with a thin reaction zone appearing behind it in the concentration plot. Unlike in 1.4.2, the system does not relax to the CJ state behind the detonation wave, as thermal energy is continually added to the reflective left boundary. The region behind the reaction zone is thus complex.

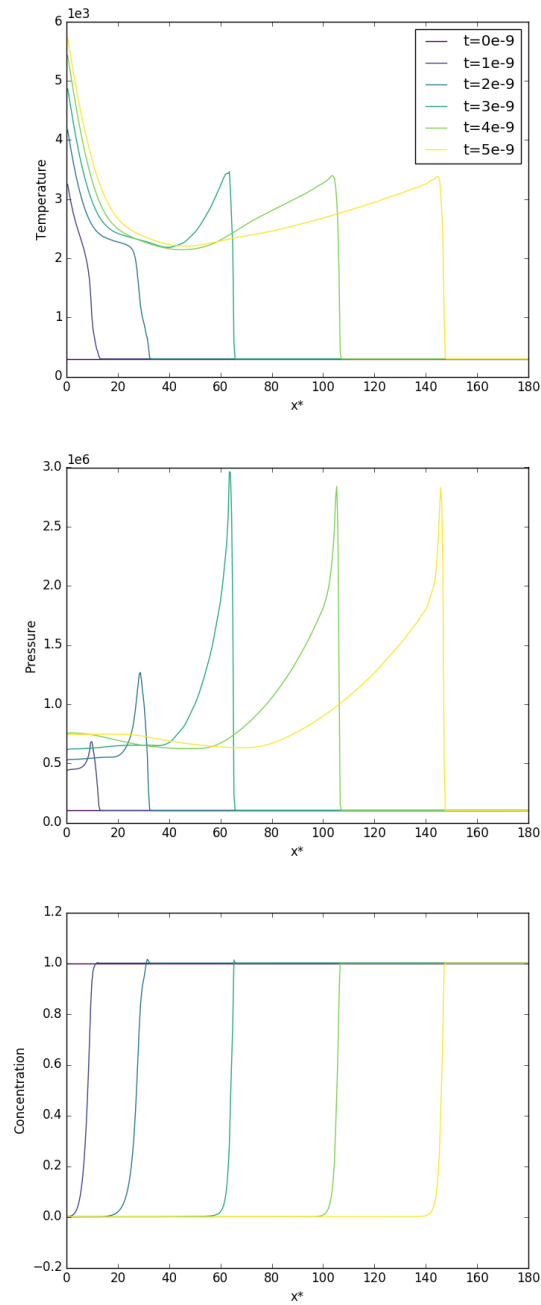


Figure 1.5: Temperature, pressure, and concentration of reactant in the heating-induced detonation test

Chapter 2

Objective 2: Improved Numerical Methods

2.1 Extending the Montecinos-Balsara ADER Method

The material in this section is published in [40?].

[54] have proposed a new, more efficient class of basis polynomials. While the method was given for conservative, one-dimensional systems in the original paper, it is extended here to general non-conservative, multidimensional systems.

Take a non-homogeneous, non-conservative, hyperbolic system of the form:

$$\frac{\partial \mathbf{Q}}{\partial t} + \nabla \cdot \vec{\mathbf{F}}(\mathbf{Q}) + \vec{\mathbf{B}}(\mathbf{Q}) \cdot \nabla \mathbf{Q} = \mathbf{S}(\mathbf{Q}) \quad (2.1)$$

where \mathbf{Q} is the vector of conserved variables, $\vec{\mathbf{F}} = (F_1, F_2, F_3)$ and $\vec{\mathbf{B}} = (B_1, B_2, B_3)$ are respectively the conservative nonlinear fluxes and matrices corresponding to the purely non-conservative components of the system, and $\mathbf{S}(\mathbf{Q})$ is the algebraic source vector.

Define spatial variables $x^{(1)}, x^{(2)}, x^{(3)}$. Take the space-time cell $C = [x_{i_1}^{(1)}, x_{i_1+1}^{(1)}] \times [x_{i_2}^{(2)}, x_{i_2+1}^{(2)}] \times [x_{i_3}^{(3)}, x_{i_3+1}^{(3)}] \times [t_n, t_{n+1}]$. Define the scaled spatial and temporal variables:

$$\chi^{(k)} = \frac{x^{(k)} - x_{i_k}^{(k)}}{x_{i_k+1}^{(k)} - x_{i_k}^{(k)}} \quad (2.2a)$$

$$\tau = \frac{t - t_n}{t_{n+1} - t_n} \quad (2.2b)$$

Thus, C becomes:

$$(\chi^{(1)}, \chi^{(2)}, \chi^{(3)}, \tau) \in [0, 1]^4 \quad (2.3)$$

2.1 Extending the Montecinos-Balsara ADER Method

By rescaling \vec{F} , \vec{B} , S by the appropriate constant factors, and defining $\tilde{\nabla} = (\partial_{\chi^{(1)}}, \partial_{\chi^{(2)}}, \partial_{\chi^{(3)}})$, within C equation (2.1) becomes:

$$\frac{\partial Q}{\partial \tau} + \tilde{\nabla} \cdot \vec{F}(Q) + \vec{B}(Q) \cdot \tilde{\nabla} Q = S(Q) \quad (2.4)$$

A basis $\{\psi_0, \dots, \psi_N\}$ of P_N and inner product $\langle \cdot, \cdot \rangle$ are now required to produce a polynomial reconstruction of Q within C . Traditionally, this basis has been chosen to be either nodal ($\psi_i(\alpha_j) = \delta_{ij}$ where $\{\alpha_0, \dots, \alpha_N\}$ are a set of nodes, e.g. the Gauss-Legendre abscissae - see [22]), or modal (e.g. the Legendre polynomials - see [5]).

[54] take the following approach. $\langle \cdot, \cdot \rangle$ is taken to be the usual integral product on $[0, 1]$. Supposing that $N = 2n + 1$ for some $n \in \mathbb{N}$, Gauss-Legendre nodes $\{\alpha_0, \dots, \alpha_n\}$ are taken. The basis $\Psi = \{\psi_0, \dots, \psi_N\} \subset P_N$ is taken with the following properties for $i = 0, \dots, n$:

$$\begin{cases} \psi_i(\alpha_j) = \delta_{ij} & \psi'_i(\alpha_j) = 0 \\ \psi_{n+1+i}(\alpha_j) = 0 & \psi'_{n+1+i}(\alpha_j) = \delta_{ij} \end{cases} \quad (2.5)$$

Define the following subsets:

$$\Psi^0 = \{\psi_i : 0 \leq i \leq n\} \quad (2.6a)$$

$$\Psi^1 = \{\psi_i : n + 1 \leq i \leq 2n + 1\} \quad (2.6b)$$

The WENO method (as used in [20]) produces an order- N polynomial reconstruction $w(\chi^{(1)}, \chi^{(2)}, \chi^{(3)})$ of the data at time t_n in $[x_{i_1}^{(1)}, x_{i_1+1}^{(1)}] \times [x_{i_2}^{(2)}, x_{i_2+1}^{(2)}] \times [x_{i_3}^{(3)}, x_{i_3+1}^{(3)}]$. It is used as initial data in the problem of finding the Galerkin predictor. Taking representation $w = w_{abc} \psi_a(\chi^{(1)}) \psi_b(\chi^{(2)}) \psi_c(\chi^{(3)})$ we have for $0 \leq i, j, k \leq n$:

$$w_{ijk} = w(\alpha_i, \alpha_j, \alpha_k) \quad (2.7a)$$

$$w_{(n+i+1)jk} = \partial_{\chi^{(1)}} w(\alpha_i, \alpha_j, \alpha_k) \quad (2.7b)$$

$$w_{i(n+j+1)k} = \partial_{\chi^{(2)}} w(\alpha_i, \alpha_j, \alpha_k) \quad (2.7c)$$

$$w_{ij(n+k+1)} = \partial_{\chi^{(3)}} w(\alpha_i, \alpha_j, \alpha_k) \quad (2.7d)$$

Take the following temporal nodes, where τ_1, \dots, τ_N are the usual Legendre-Gauss nodes on $[0, 1]$ and $\tau_0 = 0$ or $\tau_0 = 1$ if we are performing a Continuous Galerkin / Discontinuous

2.1 Extending the Montecinos-Balsara ADER Method

Galerkin reconstruction, respectively:

$$\{\tau_0, \dots, \tau_N\} \quad (2.8)$$

Define $\Phi = \{\phi_0, \dots, \phi_N\} \subset P_N$ to be the set of Lagrange interpolating polynomials on the temporal nodes. We now define the spatio-temporal polynomial basis $\Theta = \Phi \otimes \Psi \otimes \Psi \otimes \Psi = \{\theta_\beta\}$ for $0 \leq \beta \leq (N+1)^4 - 1$. Define subsets $\Theta^{\iota\xi\kappa} = \Phi \otimes \Psi^\iota \otimes \Psi^\xi \otimes \Psi^\kappa = \{\theta_\mu^{\iota\xi\kappa}\}$ where $\iota, \xi, \kappa \in \{0, 1\}$ for $0 \leq \mu \leq (N+1)(n+1)^3 - 1$.

Denoting the Galerkin predictor by \mathbf{q} , take the following set of approximations:

$$\mathbf{Q} \approx \theta_\beta \mathbf{q}_\beta = \theta_\mu^{\iota\xi\kappa} \mathbf{q}_\mu^{\iota\xi\kappa} \quad (2.9a)$$

$$\vec{\mathbf{F}}(\mathbf{Q}) \approx \theta_\beta \vec{\mathbf{F}}_\beta = \theta_\mu^{\iota\xi\kappa} \vec{\mathbf{F}}_\mu^{\iota\xi\kappa} \quad (2.9b)$$

$$\vec{\mathbf{B}}(\mathbf{Q}) \cdot \tilde{\nabla} \mathbf{Q} \approx \theta_\beta \mathbf{B}_\beta = \theta_\mu^{\iota\xi\kappa} \mathbf{B}_\mu^{\iota\xi\kappa} \quad (2.9c)$$

$$\mathbf{S}(\mathbf{Q}) \approx \theta_\beta \mathbf{S}_\beta = \theta_\mu^{\iota\xi\kappa} \mathbf{S}_\mu^{\iota\xi\kappa} \quad (2.9d)$$

for some coefficients $\mathbf{q}_\beta, \vec{\mathbf{F}}_\beta, \mathbf{B}_\beta, \mathbf{S}_\beta$. The *nodal basis representation* is used for the coefficients of Θ^{000} :

$$\vec{\mathbf{F}}_\mu^{000} = \vec{\mathbf{F}}(\mathbf{q}_\mu^{000}) \quad (2.10a)$$

$$\mathbf{B}_\mu^{000} = B_1(\mathbf{q}_\mu^{000}) \mathbf{q}_\mu^{100} + B_2(\mathbf{q}_\mu^{000}) \mathbf{q}_\mu^{010} + B_3(\mathbf{q}_\mu^{000}) \mathbf{q}_\mu^{001} \quad (2.10b)$$

$$\mathbf{S}_\mu^{000} = \mathbf{S}(\mathbf{q}_\mu^{000}) \quad (2.10c)$$

In general, we have:

$$\vec{\mathbf{F}}_\mu^{\iota\xi\kappa} = \partial_\chi^\iota \partial_v^\xi \partial_\zeta^\kappa (\vec{\mathbf{F}}(\mathbf{Q})) \quad (2.11a)$$

$$\mathbf{B}_\mu^{\iota\xi\kappa} = \partial_\chi^\iota \partial_v^\xi \partial_\zeta^\kappa (\vec{\mathbf{B}}(\mathbf{Q}) \cdot \tilde{\nabla} \mathbf{Q}) \quad (2.11b)$$

$$\mathbf{S}_\mu^{\iota\xi\kappa} = \partial_\chi^\iota \partial_v^\xi \partial_\zeta^\kappa (\mathbf{S}(\mathbf{Q})) \quad (2.11c)$$

where the right-hand-side is evaluated at the nodal point corresponding to μ . The full

2.1 Extending the Montecinos-Balsara ADER Method

expressions are omitted here for brevity's sake, but note that for a one-dimensional system:

$$\mathbf{F}_{1\mu}^{100} = \frac{\partial \mathbf{F}(\mathbf{q}_\mu^{000})}{\partial \mathbf{Q}} \cdot \mathbf{q}_\mu^{100} \quad (2.12a)$$

$$\begin{aligned} \mathbf{B}_\mu^{100} = & \left(\frac{\partial B_1(\mathbf{q}_\mu^{000})}{\partial \mathbf{Q}} \cdot \mathbf{q}_\mu^{100} \right) \cdot \mathbf{q}_\mu^{100} \\ & + B_1(\mathbf{q}_\mu^{000}) \cdot \left(\frac{\partial^2 \theta_\kappa^{000}(\chi_\mu, \tau_\mu)}{\partial \chi^2} \mathbf{q}_\mu^{000} + \frac{\partial^2 \theta_\kappa^{100}(\chi_\mu, \tau_\mu)}{\partial \chi^2} \mathbf{q}_\mu^{100} \right) \end{aligned} \quad (2.12b)$$

$$\mathbf{S}_\mu^{100} = \frac{\partial \mathbf{S}(\mathbf{q}_\mu^{000})}{\partial \mathbf{Q}} \cdot \mathbf{q}_\mu^{100} \quad (2.12c)$$

where χ_μ, τ_μ are the spatial and temporal coordinates where $\theta_\mu^{100} = 0$ and $\partial_\chi \theta_\mu^{100} = 1$. Note that $\frac{\partial B_1}{\partial \mathbf{Q}}$ is a rank 3 tensor.

Consider functions f, g of the following form:

$$f(\tau, \chi^{(1)}, \chi^{(2)}, \chi^{(3)}) = f_\tau(\tau) f_1(\chi^{(1)}) f_2(\chi^{(2)}) f_3(\chi^{(3)}) \quad (2.13a)$$

$$g(\tau, \chi^{(1)}, \chi^{(2)}, \chi^{(3)}) = g_\tau(\tau) g_1(\chi^{(1)}) g_2(\chi^{(2)}) g_3(\chi^{(3)}) \quad (2.13b)$$

Define the following integral operators:

$$[f, g]^t = f_\tau(t) g_\tau(t) \langle f_1, g_1 \rangle \langle f_2, g_2 \rangle \langle f_3, g_3 \rangle \quad (2.14a)$$

$$\{f, g\} = \langle f_\tau, g_\tau \rangle \langle f_1, g_1 \rangle \langle f_2, g_2 \rangle \langle f_3, g_3 \rangle \quad (2.14b)$$

Multiplying (2.9b) by test function θ_α , using the polynomial approximations for $\mathbf{Q}, \vec{\mathbf{F}}, \vec{\mathbf{B}}, \mathbf{S}$, and integrating over space and time gives:

$$\left\{ \theta_\alpha, \frac{\partial \theta_\beta}{\partial \tau} \right\} \mathbf{q}_\beta = \{ \theta_\alpha, \theta_\beta \} (\mathbf{S}_\beta - \mathbf{B}_\beta) - \left\{ \theta_\alpha, \frac{\partial \theta_\beta}{\partial \chi^{(k)}} \right\} \mathbf{F}_{k\beta} \quad (2.15)$$

2.1.1 The Discontinuous Galerkin Method

This method of computing the Galerkin predictor allows solutions to be discontinuous at temporal cell boundaries, and is also suitable for stiff source terms. Integrating (2.15) by parts in time gives:

2.1 Extending the Montecinos-Balsara ADER Method

$$\begin{aligned} \left([\theta_\alpha, \theta_\beta]^1 - \left\{ \frac{\partial \theta_\alpha}{\partial \tau}, \theta_\beta \right\} \right) \mathbf{q}_\beta &= [\theta_\alpha, \mathbf{w}]^0 + \{\theta_\alpha, \theta_\beta\} (\mathbf{S}_\beta - \mathbf{B}_\beta) \\ &\quad - \left\{ \theta_\alpha, \frac{\partial \theta_\beta}{\partial \chi^{(k)}} \right\} \mathbf{F}_{k,\beta} \end{aligned} \quad (2.16)$$

where \mathbf{w} is the reconstruction obtained at the start of the time step with the WENO method. Take the following ordering:

$$\theta_{(N+1)^3 h + (N+1)^2 i + (N+1) j + k}(\tau, \chi, v, \zeta) = \phi_h(\tau) \psi_i(\chi) \psi_j(v) \psi_k(\zeta) \quad (2.17)$$

where $0 \leq h, i, j, k \leq N$. Thus, define the following:

$$U_{\alpha\beta} = [\theta_\alpha, \theta_\beta]^1 - \left\{ \frac{\partial \theta_\alpha}{\partial \tau}, \theta_\beta \right\} = (R^1 - M^{\tau,1}) \otimes (M^\chi)^3 \quad (2.18a)$$

$$V_{\alpha\beta}^k = \left\{ \theta_\alpha, \frac{\partial \theta_\beta}{\partial \chi^{(k)}} \right\} = M^\tau \otimes (M^\chi)^{k-1} \otimes M^{\chi,1} \otimes (M^\chi)^{3-k} \quad (2.18b)$$

$$\mathbf{W}_\alpha = [\theta_\alpha, \Psi_\gamma]^0 \mathbf{w}_\gamma = R^0 \otimes (M^\chi)^3 \quad (2.18c)$$

$$Z_{\alpha\beta} = \{\theta_\alpha, \theta_\beta\} = M^\tau \otimes (M^\chi)^3 \quad (2.18d)$$

where $\{\Psi_\gamma\} = \Psi \otimes \Psi \otimes \Psi$ and:

$$\begin{cases} M_{ij}^\tau = \langle \phi_i, \phi_j \rangle & M_{ij}^{\tau,1} = \langle \phi'_i, \phi_j \rangle \\ M_{ij}^\chi = \langle \psi_i, \psi_j \rangle & M_{ij}^{\chi,1} = \langle \psi_i, \psi'_j \rangle \\ R_{ij}^1 = \phi_i(1) \phi_j(1) & \mathbf{R}_i^0 = \phi_i(0) \end{cases} \quad (2.19)$$

Thus:

$$U_{\alpha\beta} \mathbf{q}_\beta = \mathbf{W}_\alpha + Z_{\alpha\beta} (\mathbf{S}_\beta - \mathbf{B}_\beta) - V_{\alpha\beta}^{(k)} \mathbf{F}_{k,\beta} \quad (2.20)$$

Take the definitions:

$$\begin{cases} D &= (M^\chi)^{-1} M^{\chi,1} \\ E &= (R^1 - M^{\tau,1}) \end{cases} \quad (2.21)$$

Noting that $E\mathbf{1} = \mathbf{R}^0$, we have, by inversion of U :

2.1 Extending the Montecinos-Balsara ADER Method

$$\begin{aligned} \mathbf{q} = & \left(\mathbf{1} \otimes I^3 \right) \mathbf{w} + \left(E^{-1} M^\tau \otimes I^3 \right) (\mathbf{S} - \mathbf{B}) \\ & - \left(E^{-1} M^\tau \otimes I^{k-1} \otimes D \otimes I^{3-k} \right) \mathbf{F}_k \end{aligned} \quad (2.22)$$

Thus, we have:

$$\begin{aligned} \mathbf{q}_{hijk} = & \mathbf{w}_{ijk} + \left(E^{-1} M^\tau \right)_{hm} (\mathbf{S}_{mijk} - \mathbf{B}_{mijk}) \\ & - \left(E^{-1} M^\tau \right)_{hm} \left(D_{in} (\mathbf{F}_1)_{mnjk} + D_{jn} (\mathbf{F}_2)_{mink} + D_{kn} (\mathbf{F}_3)_{mijn} \right) \end{aligned} \quad (2.23)$$

Note then that $\mathbf{q}^{\iota\xi\kappa}$ is a function of $\mathbf{S}^{\iota\xi\kappa}, \mathbf{B}^{\iota\xi\kappa}, \vec{\mathbf{F}}$:

$$\mathbf{q}^{\iota\xi\kappa} = \mathcal{F}(\mathbf{S}^{\iota\xi\kappa}) + \mathcal{F}(\mathbf{B}^{\iota\xi\kappa}) + \mathcal{G}_{\iota\xi\kappa}(\vec{\mathbf{F}}^{000}, \dots, \vec{\mathbf{F}}^{111}) \quad (2.24)$$

where $\mathcal{F}, \mathcal{G}_{\iota\xi\kappa}$ are linear functions. Note in turn that, by (2.11c):

$$\mathbf{S}^{\iota\xi\kappa} = \mathcal{H} \left(\bigcup_{(0,0,0) \leq (a,b,c) \leq (\iota,\xi,\kappa)} \mathbf{q}^{abc} \right) \quad (2.25)$$

where \mathcal{H} is a nonlinear function.

In the case of stiff source terms, the following Picard iteration procedure can be used to solve (2.23), as adapted from [54]:

$$\begin{aligned} (\mathbf{q}^{\iota\xi\kappa})_{m+1} = & \mathcal{F} \left(\mathcal{H} \left((\mathbf{q}^{\iota\xi\kappa})_{m+1} \cup \bigcup_{\substack{(0,0,0) \leq (a,b,c) \leq (\iota,\xi,\kappa) \\ (a,b,c) \neq (\iota,\xi,\kappa)}}} (\mathbf{q}^{abc})_m \right) \right) \\ & + \mathcal{F} \left((\mathbf{B}^{\iota\xi\kappa})_m \right) + \mathcal{G}_{\iota\xi\kappa} \left((\vec{\mathbf{F}}^{000})_m, \dots, (\vec{\mathbf{F}}^{111})_m \right) \end{aligned} \quad (2.26)$$

2.1.2 The Continuous Galerkin Method

This method of computing the Galerkin predictor is not suitable for stiff source terms, but is less computationally expensive and ensures continuity across temporal cell boundaries. The

2.1 Extending the Montecinos-Balsara ADER Method

first $N + 1$ elements of \mathbf{q} are fixed by imposing the following condition:

$$\mathbf{q}(\chi, 0) = \mathbf{w}(\chi) \quad (2.27)$$

For $\mathbf{v} \in \mathbb{R}^{(N+1)^2}$ and $X \in M_{(N+1)^2, (N+1)^2}(\mathbb{R})$, let $\mathbf{v} = (\mathbf{v}^0, \mathbf{v}^1)$ and $X = \begin{pmatrix} X^{00} & X^{01} \\ X^{10} & X^{11} \end{pmatrix}$ where \mathbf{v}^0, X^{00} are the components relating solely to the first $N + 1$ components of \mathbf{v} . We only need to find the latter components of \mathbf{q} , and thus, from (2.15), we have:

$$\begin{aligned} \left\{ \theta_\alpha, \frac{\partial \theta_\beta}{\partial \tau} \right\}^{11} \mathbf{q}_\beta^1 &= \{\theta_\alpha, \theta_\beta\}^{11} (\mathbf{S}_\beta^1 - \mathbf{B}_\beta^1) - \left\{ \theta_\alpha, \frac{\partial \theta_\beta}{\partial \chi^{(k)}} \right\}^{11} \mathbf{F}_{k\beta}^1 \\ &+ \{\theta_\alpha, \theta_\beta\}^{10} (\mathbf{S}_\beta^0 - \mathbf{B}_\beta^0) - \left\{ \theta_\alpha, \frac{\partial \theta_\beta}{\partial \chi^{(k)}} \right\}^{10} \mathbf{F}_{k\beta}^0 \end{aligned} \quad (2.28)$$

Define the following:

$$U_{\alpha\beta} = \left\{ \theta_\alpha, \frac{\partial \theta_\beta}{\partial \tau} \right\}^{11} \quad (2.29a)$$

$$V_{\alpha\beta}^k = \left\{ \theta_\alpha, \frac{\partial \theta_\beta}{\partial \chi^{(k)}} \right\}^{11} \quad (2.29b)$$

$$\mathbf{W}_\alpha = \{\theta_\alpha, \theta_\beta\}^{10} (\mathbf{S}_\beta - \mathbf{B}_\beta)^0 - \left\{ \theta_\alpha, \frac{\partial \theta_\beta}{\partial \chi^{(k)}} \right\}^{10} \mathbf{F}_{k\beta}^0 \quad (2.29c)$$

$$Z_{\alpha\beta} = \{\theta_\alpha, \theta_\beta\}^{11} \quad (2.29d)$$

Thus:

$$U_{\alpha\beta} \mathbf{q}_\beta^1 = \mathbf{W}_\alpha + Z_{\alpha\beta} (\mathbf{S}_\beta^1 - \mathbf{B}_\beta^1) - V_{\alpha\beta}^k \mathbf{F}_{k\beta}^1 \quad (2.30)$$

Note that, as with the discontinuous Galerkin method, \mathbf{W} has no dependence on the degrees of freedom in \mathbf{q} . As the source terms are not stiff, the following iteration is used:

$$U_{\alpha\beta} (\mathbf{q}_\beta^1)_{m+1} = \mathbf{W}_\alpha + Z_{\alpha\beta} \left((\mathbf{S}_\beta^1)_m - (\mathbf{B}_\beta^1)_m \right) - V_{\alpha\beta}^k (\mathbf{F}_{k\beta}^1)_m \quad (2.31)$$

2.1.3 Convergence Properties

In [40] it was proved that for traditional choices of polynomial bases, the eigenvalues of $U^{-1}V^i$ are all 0 for any $N \in \mathbb{N}$, for $i = 1, 2, 3$. This implies that in the conservative,

2.1 Extending the Montecinos-Balsara ADER Method

homogeneous case ($\vec{B} = S = 0$), owing to the Banach Fixed Point Theorem, existence and uniqueness of a solution are established, and convergence to this solution is guaranteed. As noted in [27], in the linear case it is implied that the iterative procedure converges after at most $N + 1$ iterations. A proof of this result for the Montecinos-Balsara polynomial basis class is now provided here. For the theory in linear algebra required for this section, please consult a standard textbook on the subject, such as [57].

Take the definitions (2.19), (2.21). Consider that:

$$U^{-1}V^k = E^{-1}M^\tau \otimes I^{k-1} \otimes D \otimes I^{3-k} \quad (2.32)$$

Therefore:

$$(U^{-1}V^k)^m = (E^{-1}M^\tau)^m \otimes (I^{k-1})^m \otimes D^m \otimes (I^{3-k})^m \quad (2.33)$$

A matrix X is nilpotent ($X^k = 0$ for some $k \in \mathbb{N}$) if and only if all its eigenvalues are 0. Note that $U^{-1}V^k$ is nilpotent if $D^m = 0$ for some $m \in \mathbb{N}$.

Note that if $p \in P_N$ then $p = a_j \psi_j$ for some unique coefficient vector \mathbf{a} . Thus, taking inner products with ψ_i , we have $\langle \psi_i, \psi_j \rangle a_j = \langle \psi_i, p \rangle$ for $i = 0, \dots, N$. This produces the following result:

$$p = a_j \psi_j \Leftrightarrow \mathbf{a} = (M^X)^{-1} \mathbf{x}, \quad x_i = \langle \psi_i, p \rangle \quad (2.34)$$

Taking $\mathbf{a} \in \mathbb{R}^{N+1}$, define:

$$p = a_0 \psi_0 + \dots + a_N \psi_N \in P_N \quad (2.35)$$

Note that:

$$(M^{X,1} \mathbf{a})_i = \langle \psi_i, \psi'_0 \rangle a_0 + \dots + \langle \psi_i, \psi'_N \rangle a_N = \langle \psi_i, p' \rangle \quad (2.36)$$

Thus, by (2.34):

$$\left((M^X)^{-1} M^{X,1} \mathbf{a} \right)_i \psi_i = (D\mathbf{a})_i \psi_i = p' \quad (2.37)$$

By induction:

$$(D^m \mathbf{a})_i \psi_i = p^{(m)} \quad (2.38)$$

for any $m \in \mathbb{N}$. As $p \in P_N$, $D^{N+1} \mathbf{a} = \mathbf{0}$. As \mathbf{a} was chosen arbitrarily, $D^{N+1} = 0$. No specific choice has been made for $N \in \mathbb{N}$ and thus the result holds in general.

Thus, in the case that $\vec{\mathbf{B}} = \mathbf{S} = \mathbf{0}$, existence and uniqueness of a solution are established, and convergence to this solution is guaranteed for the iterative solution to (2.20) in the Discontinuous Galerkin case, and (2.30) in the Continuous Galerkin case.

2.2 Operator Splitting Methods

The material in this section is published in [39].

Note that (1a), (1b), (1c), (1d), (3) can be written in the following form:

$$\frac{\partial \mathbf{Q}}{\partial t} + \nabla \cdot \mathbf{F}(\mathbf{Q}) + \mathbf{B}(\mathbf{Q}) \cdot \nabla \mathbf{Q} = \mathbf{S}(\mathbf{Q}) \quad (2.39)$$

As described in [69], a viable way to solve inhomogeneous systems of PDEs is to employ an operator splitting. That is, the following subsystems are solved:

$$\frac{\partial \mathbf{Q}}{\partial t} + \nabla \cdot \mathbf{F}(\mathbf{Q}) + \mathbf{B}(\mathbf{Q}) \cdot \nabla \mathbf{Q} = \mathbf{0} \quad (2.40a)$$

$$\frac{d\mathbf{Q}}{dt} = \mathbf{S}(\mathbf{Q}) \quad (2.40b)$$

The advantage of this approach is that specialized solvers can be employed to compute the results of the different subsystems. Let $H^{\delta t}, S^{\delta t}$ be the operators that take data $\mathbf{Q}(x, t)$ to $\mathbf{Q}(x, t + \delta t)$ under systems (2.40a) and (2.40b) respectively. A second-order scheme (in time) for solving the full set of PDEs over time step $[0, \Delta t]$ is obtained by calculating $\mathbf{Q}_{\Delta t}$ using a Strang splitting:

$$\mathbf{Q}_{\Delta t} = S^{\frac{\Delta t}{2}} H^{\Delta t} S^{\frac{\Delta t}{2}} \mathbf{Q}_0 \quad (2.41)$$

2.2 Operator Splitting Methods

In the scheme proposed here, the homogeneous subsystem will be solved using a WENO reconstruction of the data, followed by a finite volume update, and the temporal ODEs will be solved with appropriate ODE solvers. This new scheme will be referred to here as *the Split-WENO method*.

Noting that $\frac{d\rho}{dt} = 0$ over the ODE time step, the operator S entails solving the following systems:

$$\frac{dA}{dt} = \frac{-3}{\tau_1} |A|^{\frac{5}{3}} A \operatorname{dev}(G) \quad (2.42a)$$

$$\frac{d\mathbf{J}}{dt} = -\frac{1}{\tau_2} \frac{T\rho_0}{T_0\rho} \mathbf{J} \quad (2.42b)$$

These systems can be solved concurrently with a stiff ODE solver. The Jacobians of these two systems to be used in an ODE solver are given in A.2 and A.2. However, these systems can also be solved separately, using the analytical results presented in 2.2.2 and 2.2.3, under specific assumptions. The second-order Strang splitting is then:

$$\mathbf{Q}_{\Delta t} = D^{\frac{\Delta t}{2}} T^{\frac{\Delta t}{2}} H^{\Delta t} T^{\frac{\Delta t}{2}} D^{\frac{\Delta t}{2}} \mathbf{Q}_0 \quad (2.43)$$

where $D^{\delta t}, T^{\delta t}$ are the operators solving the distortion and thermal impulse ODEs respectively, over time step δt . This allows us to bypass the relatively computationally costly process of solving these systems numerically.

2.2.1 The Homogeneous System

A WENO reconstruction of the cell-averaged data is performed at the start of the time step (as described in 0.4.1). Focusing on a single cell C_i at time t_n , we have $\mathbf{w}^n(\mathbf{x}) = \mathbf{w}_p^n \Psi_p(\chi(\mathbf{x}))$ in C_i where Ψ_p is a tensor product of basis functions in each of the spatial dimensions. The flux in C is approximated by $\mathbf{F}(\mathbf{x}) \approx \mathbf{F}(\mathbf{w}_p) \Psi_p(\chi(\mathbf{x}))$. \mathbf{w}_p are stepped forwards half a time step using the update formula:

$$\frac{\mathbf{w}_p^{n+\frac{1}{2}} - \mathbf{w}_p^n}{\Delta t/2} + \mathbf{F}(\mathbf{w}_k^n) \cdot \nabla \Psi_k(\chi_p) + \mathbf{B}(\mathbf{w}_p^n) \cdot (\mathbf{w}_k^n \nabla \Psi_k(\chi_p)) = 0 \quad (2.44)$$

i.e.

$$\mathbf{w}_p^{n+\frac{1}{2}} = \mathbf{w}_p^n - \frac{\Delta t}{2\Delta x} \left(\mathbf{F}(\mathbf{w}_k^n) \cdot \nabla \Psi_k(\chi_p) + \mathbf{B}(\mathbf{w}_p^n) \cdot (\mathbf{w}_k^n \nabla \Psi_k(\chi_p)) \right) \quad (2.45)$$

where χ_p is the node corresponding to Ψ_p . This evolution to the middle of the time step is similar to that used in the second-order MUSCL and SLIC schemes (see [69]) and, as with those schemes, it is integral to giving the method presented here its second-order accuracy.

Integrating (2.40a) over C gives:

$$\mathbf{Q}_i^{n+1} = \mathbf{Q}_i^n - \Delta t_n \left(\mathbf{P}_i^{n+\frac{1}{2}} + \mathbf{D}_i^{n+\frac{1}{2}} \right) \quad (2.46)$$

where

$$\mathbf{Q}_i^n = \frac{1}{V} \int_C \mathbf{Q}(\mathbf{x}, t_n) d\mathbf{x} \quad (2.47a)$$

$$\mathbf{P}_i^{n+\frac{1}{2}} = \frac{1}{V} \int_C \mathbf{B}(\mathbf{Q}(\mathbf{x}, t_{n+\frac{1}{2}})) \cdot \nabla \mathbf{Q}(\mathbf{x}, t_{n+\frac{1}{2}}) d\mathbf{x} \quad (2.47b)$$

$$\mathbf{D}_i^{n+\frac{1}{2}} = \frac{1}{V} \oint_{\partial C} \mathcal{D}(\mathbf{Q}^-(\mathbf{s}, t_{n+\frac{1}{2}}), \mathbf{Q}^+(\mathbf{s}, t_{n+\frac{1}{2}})) d\mathbf{s} \quad (2.47c)$$

where V is the volume of C and $\mathbf{Q}^-, \mathbf{Q}^+$ are the interior and exterior extrapolated states at the boundary of C , respectively.

Note that (2.40a) can be rewritten as:

$$\frac{\partial \mathbf{Q}}{\partial t} + \mathbf{M}(\mathbf{Q}) \cdot \nabla \mathbf{Q} = \mathbf{0} \quad (2.48)$$

where $\mathbf{M} = \frac{\partial \mathbf{F}}{\partial \mathbf{Q}} + \mathbf{B}$. Let \mathbf{n} be the normal to the boundary at point $\mathbf{s} \in \partial C$. For the GPR model, $\hat{\mathbf{M}} = \mathbf{M}(\mathbf{Q}(\mathbf{s})) \cdot \mathbf{n}$ is a diagonalizable matrix with decomposition $\hat{\mathbf{M}} = \hat{\mathbf{R}} \hat{\Lambda} \hat{\mathbf{R}}^{-1}$ where the columns of $\hat{\mathbf{R}}$ are the right eigenvectors and $\hat{\Lambda}$ is the diagonal matrix of eigenvalues. Define also $\hat{\mathbf{F}} = \mathbf{F} \cdot \mathbf{n}$ and $\hat{\mathbf{B}} = \mathbf{B} \cdot \mathbf{n}$. Using these definitions, the interface terms arising in the FV formula have the following form:

$$\mathcal{D}(\mathbf{Q}^-, \mathbf{Q}^+) = \frac{1}{2} \left(\hat{\mathbf{F}}(\mathbf{Q}^+) + \hat{\mathbf{F}}(\mathbf{Q}^-) + \tilde{\mathbf{B}}(\mathbf{Q}^+ - \mathbf{Q}^-) + \tilde{\mathbf{M}}(\mathbf{Q}^+ - \mathbf{Q}^-) \right) \quad (2.49)$$

\tilde{M} is chosen to either correspond to a Rusanov/Lax-Friedrichs flux (see [69]):

$$\tilde{M} = \max \left(\max \left| \hat{\Lambda} \left(\mathbf{Q}^+ \right) \right|, \max \left| \hat{\Lambda} \left(\mathbf{Q}^- \right) \right| \right) \quad (2.50)$$

or a simplified Osher–Solomon flux (see [25, 26]):

$$\tilde{M} = \int_0^1 \left| \hat{M} \left(\mathbf{Q}^- + z \left(\mathbf{Q}^+ - \mathbf{Q}^- \right) \right) \right| dz \quad (2.51)$$

where

$$\left| \hat{M} \right| = \hat{R} \left| \hat{\Lambda} \right| \hat{R}^{-1} \quad (2.52)$$

\tilde{B} takes the following form:

$$\tilde{B} = \int_0^1 \hat{B} \left(\mathbf{Q}^- + z \left(\mathbf{Q}^+ - \mathbf{Q}^- \right) \right) dz \quad (2.53)$$

It was found that the Osher–Solomon flux would often produce slightly less diffusive results, but that it was more computationally expensive, and also had a greater tendency to introduce numerical artefacts.

$\mathbf{P}_i^{n+\frac{1}{2}}, \mathbf{D}_i^{n+\frac{1}{2}}$ are calculated using an $N + 1$ -point Gauss-Legendre quadrature, replacing $\mathbf{Q} \left(\mathbf{x}, t_{n+\frac{1}{2}} \right)$ with $\mathbf{w}^{n+\frac{1}{2}} \left(\mathbf{x} \right)$.

2.2.2 The Thermal Impulse ODEs

Taking the EOS for the GPR model (6) and denoting by $E_2^{(A)}, E_2^{(J)}$ the components of E_2 depending on A and \mathbf{J} respectively, we have:

$$\begin{aligned} T &= \frac{E_1}{c_v} \\ &= \frac{E - E_2^{(A)}(\rho, s, A) - E_3(\mathbf{v})}{c_v} - \frac{1}{c_v} E_2^{(J)}(\mathbf{J}) \\ &= c_1 - c_2 \|\mathbf{J}\|^2 \end{aligned} \quad (2.54)$$

where:

$$c_1 = \frac{E - E_2^{(A)}(A) - E_3(\mathbf{v})}{c_v} \quad (2.55a)$$

$$c_2 = \frac{c_t^2}{2c_v} \quad (2.55b)$$

Over the time period of the ODE (2.42b), $c_1, c_2 > 0$ are constant. We have:

$$\frac{dJ_i}{dt} = - \left(\frac{1}{\tau_2} \frac{\rho_0}{T_0 \rho} \right) J_i \left(c_1 - c_2 \|\mathbf{J}\|^2 \right) \quad (2.56)$$

Therefore:

$$\frac{d}{dt} (J_i^2) = J_i^2 \left(-a + b (J_1^2 + J_2^2 + J_3^2) \right) \quad (2.57)$$

where

$$a = \frac{2\rho_0}{\tau_2 T_0 \rho c_v} \left(E - E_2^{(A)}(A) - E_3(\mathbf{v}) \right) \quad (2.58a)$$

$$b = \frac{\rho_0 c_t^2}{\tau_2 T_0 \rho c_v} \quad (2.58b)$$

Note that this is a generalized Lotka-Volterra system in $\{J_1^2, J_2^2, J_3^2\}$. It has the following analytical solution:

$$\mathbf{J}(t) = \mathbf{J}(0) \sqrt{\frac{1}{e^{at} - \frac{b}{a}(e^{at} - 1) \|\mathbf{J}(0)\|^2}} \quad (2.59)$$

2.2.3 The Distortion ODEs

Let $k_0 = \frac{3}{\tau_1} \left(\frac{\rho}{\rho_0} \right)^{\frac{5}{3}} > 0$ and let A have singular value decomposition $U\Sigma V^T$. Then:

$$G = (U\Sigma V^T)^T U\Sigma V^T = V\Sigma^2 V^T \quad (2.60)$$

$$\text{tr}(G) = \text{tr}(V\Sigma^2 V^T) = \text{tr}(\Sigma^2 V^T V) = \text{tr}(\Sigma^2) \quad (2.61)$$

Therefore:

$$\begin{aligned}
 \frac{dA}{dt} &= -k_0 U \Sigma V^T \left(V \Sigma^2 V^T - \frac{\text{tr}(\Sigma^2)}{3} I \right) \\
 &= -k_0 U \Sigma \left(\Sigma^2 - \frac{\text{tr}(\Sigma^2)}{3} I \right) V^T \\
 &= -k_0 U \Sigma \text{dev}(\Sigma^2) V^T
 \end{aligned} \tag{2.62}$$

It is a common result (see [32]) that:

$$d\Sigma = U^T dA V \tag{2.63}$$

and thus:

$$\frac{d\Sigma}{dt} = -k_0 \Sigma \text{dev}(\Sigma^2) \tag{2.64}$$

Using a fast 3×3 SVD algorithm (such as in [51]), U, V, Σ can be obtained, after which the following procedure is applied to Σ , giving $A(t) = U \Sigma(t) V^T$.

Denote the singular values of A by a_1, a_2, a_3 . Then:

$$\Sigma \text{dev}(\Sigma^2) = \begin{pmatrix} a_1 \left(a_1^2 - \frac{a_1^2 + a_2^2 + a_3^2}{3} \right) & 0 & 0 \\ 0 & a_1 \left(a_1^2 - \frac{a_1^2 + a_2^2 + a_3^2}{3} \right) & 0 \\ 0 & 0 & a_1 \left(a_1^2 - \frac{a_1^2 + a_2^2 + a_3^2}{3} \right) \end{pmatrix} \tag{2.65}$$

Letting $x_i = \frac{a_i^2}{\det(A)^{\frac{2}{3}}} = \frac{a_i^2}{\left(\frac{\rho}{\rho_0}\right)^{\frac{2}{3}}}$ we have:

$$\frac{dx_i}{d\tau} = -3x_i(x_i - \bar{x}) \tag{2.66}$$

where $\tau = \frac{2}{\tau_1} \left(\frac{\rho}{\rho_0} \right)^{\frac{7}{3}} t$ and \bar{x} is the arithmetic mean of x_1, x_2, x_3 . This ODE system travels along the surface $\Psi = \{x_1, x_2, x_3 > 0, x_1 x_2 x_3 = 1\}$ to the point $x_1, x_2, x_3 = 1$. This surface is symmetrical in the planes $x_1 = x_2, x_1 = x_3, x_2 = x_3$. As such, given that the system is autonomous, the paths of evolution of the x_i cannot cross the intersections of these planes with Ψ . Thus, any non-strict inequality of the form $x_i \geq x_j \geq x_k$ is maintained for the

whole history of the system. By considering (2.66) it is clear that in this case x_i is monotone decreasing, x_k is monotone increasing, and the time derivative of x_j may switch sign.

Note that we have:

$$\begin{cases} \frac{dx_i}{d\tau} = -x_i(2x_i - x_j - x_k) = -x_i\left(2x_i - x_j - \frac{1}{x_i x_j}\right) \\ \frac{dx_j}{d\tau} = -x_j(2x_j - x_k - x_i) = -x_j\left(2x_j - x_i - \frac{1}{x_i x_j}\right) \end{cases} \quad (2.67)$$

Thus, an ODE solver can be used on these two equations to effectively solve the ODEs for all 9 components of A . Note that:

$$\frac{dx_j}{dx_i} = \frac{x_j}{x_i} \frac{2x_j - x_i - \frac{1}{x_i x_j}}{2x_i - x_j - \frac{1}{x_i x_j}} \quad (2.68)$$

This has solution:

$$x_j = \frac{c + \sqrt{c^2 + 4(1-c)} x_i^3}{2x_i^2} \quad (2.69)$$

where

$$c = -\frac{x_{i,0}(x_{i,0}x_{j,0}^2 - 1)}{x_{i,0} - x_{j,0}} \in (-\infty, 0] \quad (2.70)$$

In the case that $x_{i,0} = x_{j,0}$, we have $x_i = x_j$ for all time. Thus, the ODE system for A has been reduced to a single ODE, as $x_j(x_i)$ can be inserted into the RHS of the equation for $\frac{dx_i}{d\tau}$. However, it is less computationally expensive to evolve the system presented in (2.67).

2.2.3.1 Bounds on the Solutions

If any of the relations in $x_i \geq x_j \geq x_k$ are in fact equalities, equality is maintained throughout the history of the system. This can be seen by noting that the time derivatives of the equal variables are in this case equal. If $x_j = x_k$ then $x_i = \frac{1}{x_j^2}$. Combining these results, the path of the system in (x_i, x_j) coordinates is in fact confined to the curved triangular region:

$$\left\{ (x_i, x_j) : x_i \leq x_i^0 \cap x_i \geq x_j \cap x_i \geq \frac{1}{x_j^2} \right\} \quad (2.71)$$

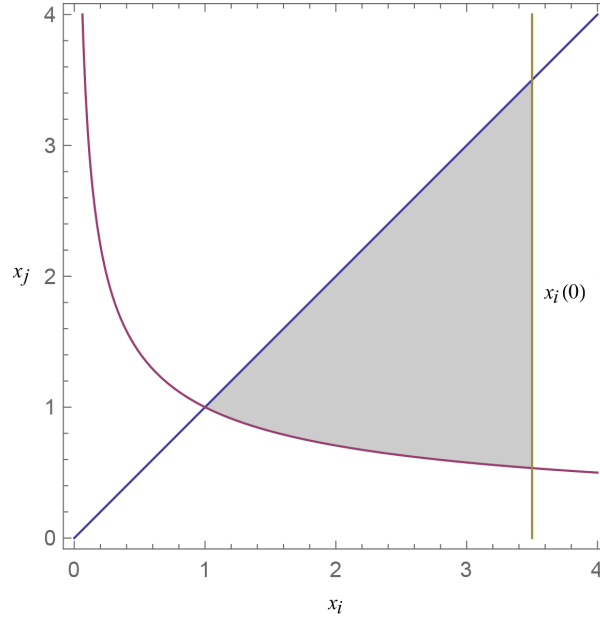


Figure 2.1: The (shaded) region to which x_i, x_j are confined in the evolution of the distortion ODEs

This is demonstrated in Figure 2.1 on page 46. By (2.67), the rate of change of x_i at a particular value $x_i = x_i^*$ is given by:

$$-x_i^* \left(2x_i^* - x_j - \frac{1}{x_i^* x_j} \right) \quad (2.72)$$

Note that:

$$\begin{aligned} \frac{d}{dx_j} \left(2x_i^* - x_j - \frac{1}{x_i^* x_j} \right) &= -1 + \frac{1}{x_i^* x_j^2} = 0 \\ \Rightarrow x_j &= \frac{1}{\sqrt{x_i^*}} \end{aligned} \quad (2.73)$$

$$\frac{d^2}{dx_j^2} \left(2x_i^* - x_j - \frac{1}{x_i^* x_j} \right) = \frac{-2}{x_i^* x_j^3} < 0 \quad (2.74)$$

Thus, x_i decreases fastest on the line $x_i = \frac{1}{x_j^2}$ (the bottom boundary of the region given in Figure 2.1 on page 46), and slowest on the line $x_i = x_j$. The rates of change of x_i along

these two lines are given respectively by:

$$\frac{dx_i}{d\tau} = -2x_i \left(x_i - \sqrt{\frac{1}{x_i}} \right) \quad (2.75a)$$

$$\frac{dx_i}{d\tau} = -x_i \left(x_i - \frac{1}{x_i^2} \right) \quad (2.75b)$$

These have implicit solutions:

$$\tau = (f(\sqrt{x_i}) + g(\sqrt{x_i})) - \left(f(\sqrt{x_i^0}) + g(\sqrt{x_i^0}) \right) \equiv F_1(x_i; x_i^0) \quad (2.76a)$$

$$\tau = (f(x_i) - g(x_i)) - \left(f(x_i^0) - g(x_i^0) \right) \equiv F_2(x_i; x_i^0) \quad (2.76b)$$

where

$$f(x_i) = \frac{1}{6} \log \left(\frac{x_i^2 + x_i + 1}{(x_i - 1)^2} \right) \quad (2.77a)$$

$$g(x_i) = \frac{1}{\sqrt{3}} \tan^{-1} \left(\frac{2x_i + 1}{\sqrt{3}} \right) \quad (2.77b)$$

As (2.66) is an autonomous system of ODEs, it has the property that its limit $x_1 = x_2 = x_3 = 1$ is never obtained in finite time, in precise arithmetic. In floating point arithmetic we may say that the system has converged when $x_i - 1 < \epsilon$ (machine epsilon) for each i . This happens when:

$$\tau > F_2(1 + \epsilon; x_i^0) \quad (2.78)$$

This provides a quick method to check whether it is necessary to run the ODE solver in a particular cell. If the following condition is satisfied then we know the system in that cell converges to the ground state over the time interval in which the ODE system is calculated:

$$\frac{2}{\tau_1} \left(\frac{\rho}{\rho_0} \right)^{\frac{7}{3}} \Delta t > F_2(1 + \epsilon; \max \{x_i^0\}) \quad (2.79)$$

If the fluid is very inviscid, resulting in a stiff ODE, the critical time is lower, and there is more chance that the ODE system in the cell reaches its limit in Δt . This check potentially saves a lot of computationally expensive stiff ODE solves. The same goes for if the flow is

slow-moving, as the system will be closer to its ground state at the start of the time step and is more likely to converge over Δt . Similarly, if the following condition is satisfied then we know for sure that an ODE solver is necessary, as the system certainly will not have converged over the timestep:

$$\frac{2}{\tau_1} \left(\frac{\rho}{\rho_0} \right)^{\frac{7}{3}} \Delta t < F_1 \left(1 + \epsilon; \max \{x_i^0\} \right) \quad (2.80)$$

2.2.3.2 Newontian Fluids

We now explore cases when even the reduced ODE system (2.67) need not be solved numerically. Define the following variables:

$$m = \frac{x_1 + x_2 + x_3}{3} \quad (2.81a)$$

$$u = \frac{(x_1 - x_2)^2 + (x_2 - x_3)^2 + (x_3 - x_1)^2}{3} \quad (2.81b)$$

It is a standard result that $m \geq \sqrt[3]{x_1 x_2 x_3}$. Thus, $m \geq 1$. Note that u is proportional to the internal energy contribution from the distortion. From (2.66) we have:

$$\frac{du}{d\tau} = -18 \left(1 - m \left(m^2 - \frac{5}{6}u \right) \right) \quad (2.82a)$$

$$\frac{dm}{d\tau} = -u \quad (2.82b)$$

Combining these equations, we have:

$$\frac{d^2 m}{d\tau^2} = -\frac{du}{d\tau} = 18 \left(1 - m \left(m^2 - \frac{5}{6}u \right) \right) \quad (2.83)$$

Therefore:

$$\begin{cases} \frac{d^2 m}{d\tau^2} + 15m \frac{dm}{d\tau} + 18(m^3 - 1) = 0 \\ m(0) = m_0 \\ m'(0) = -u_0 \end{cases} \quad (2.84)$$

2.2 Operator Splitting Methods

We make the following assumption, noting that it is true in all physical situations tested in this study:

$$m(t) = 1 + \eta(t), \quad \eta \ll 1 \quad \forall t \geq 0 \quad (2.85)$$

Thus, we have the linearized ODE:

$$\begin{cases} \frac{d^2\eta}{d\tau^2} + 15\frac{d\eta}{d\tau} + 54\eta = 0 \\ \eta(0) = m_0 - 1 \\ \eta'(0) = -u_0 \end{cases} \quad (2.86)$$

This is a Sturm-Liouville equation with solution:

$$\eta(\tau) = \frac{e^{-9\tau}}{3} \left((9m_0 - u_0 - 9)e^{3\tau} - (6m_0 - u_0 - 6) \right) \quad (2.87)$$

Thus, we also have:

$$u(\tau) = e^{-9\tau} \left(e^{3\tau} (18m_0 - 2u_0 - 18) - (18m_0 - 3u_0 - 18) \right) \quad (2.88)$$

Once $m_{\Delta t} = 1 + \eta\left(\frac{2}{\tau_1}\left(\frac{\rho}{\rho_0}\right)^{\frac{7}{3}}\Delta t\right)$ and $u_{\Delta t} = u\left(\frac{2}{\tau_1}\left(\frac{\rho}{\rho_0}\right)^{\frac{7}{3}}\Delta t\right)$ have been found, we have:

$$\frac{x_i + x_j + x_k}{3} = m_{\Delta t} \quad (2.89a)$$

$$\frac{(x_i - x_j)^2 + (x_j - x_k)^2 + (x_k - x_i)^2}{3} = u_{\Delta t} \quad (2.89b)$$

$$x_i x_j x_k = 1 \quad (2.89c)$$

This gives:

$$x_i = \frac{\sqrt[3]{6\left(\sqrt{81\Delta^2 - 6u_{\Delta t}^3} + 9\Delta\right)}}{6} + \frac{u_{\Delta t}}{\sqrt[3]{6\left(\sqrt{81\Delta^2 - 6u_{\Delta t}^3} + 9\Delta\right)}} + m_{\Delta t} \quad (2.90a)$$

$$x_j = \frac{1}{2} \left(\sqrt{\frac{x_i(3m_{\Delta t} - x_i)^2 - 4}{x_i}} + 3m_{\Delta t} - x_i \right) \quad (2.90b)$$

$$x_k = \frac{1}{x_i x_j} \quad (2.90c)$$

where

$$\Delta = -2m_{\Delta t}^3 + m_{\Delta t}u_{\Delta t} + 2 \quad (2.91)$$

Note that taking the real parts of the above expression for x_i gives:

$$x_i = \frac{\sqrt{6u_{\Delta t}}}{3} \cos\left(\frac{\theta}{3}\right) + m_{\Delta t} \quad (2.92a)$$

$$\theta = \tan^{-1}\left(\frac{\sqrt{6u_{\Delta t}^3 - 81\Delta^2}}{9\Delta}\right) \quad (2.92b)$$

At this point it is not clear which values of $\{x_i, x_j, x_k\}$ are taken by x_1, x_2, x_3 . However, this can be inferred from the fact that any relation $x_i \geq x_j \geq x_k$ is maintained over the lifetime of the system. Thus, the stiff ODE solver has been obviated by a few arithmetic operations.

2.2.3.3 Power Law Fluids

The stress-strain relationships for various kinds of fluids are shown in Figure 2.2 on page 51. Dilatants and pseudoplastics may be modelled using the following power law, with $n > 1$ and $0 < n < 1$, respectively:

$$\boldsymbol{\sigma} = K |\dot{\boldsymbol{\gamma}}|^{n-1} \dot{\boldsymbol{\gamma}} \quad (2.93)$$

$$\dot{\boldsymbol{\gamma}} = \nabla \mathbf{v} + \nabla \mathbf{v}^T - \frac{2 \operatorname{tr}(\nabla \mathbf{v})}{3} \mathbf{I} \quad (2.94)$$

$K > 0$ is known as the *consistency*, and $K |\dot{\boldsymbol{\gamma}}|^{n-1}$ is the *apparent viscosity*. The norm is taken to be:

$$|\mathbf{X}| = \sqrt{\frac{1}{2} X_{ij} X_{ij}} = \frac{\|\mathbf{X}\|_F}{\sqrt{2}} \quad (2.95)$$

In [24] it was noted that when expressing the state variables as an asymptotic expansion in the relaxation parameter τ_1 , to first order we have:

$$\boldsymbol{\sigma} = \frac{1}{6} \tau_1 \rho_0 c_s^2 \left(\nabla \mathbf{v} + \nabla \mathbf{v}^T - \frac{2}{3} \operatorname{tr}(\nabla \mathbf{v}) \mathbf{I} \right) \quad (2.96)$$

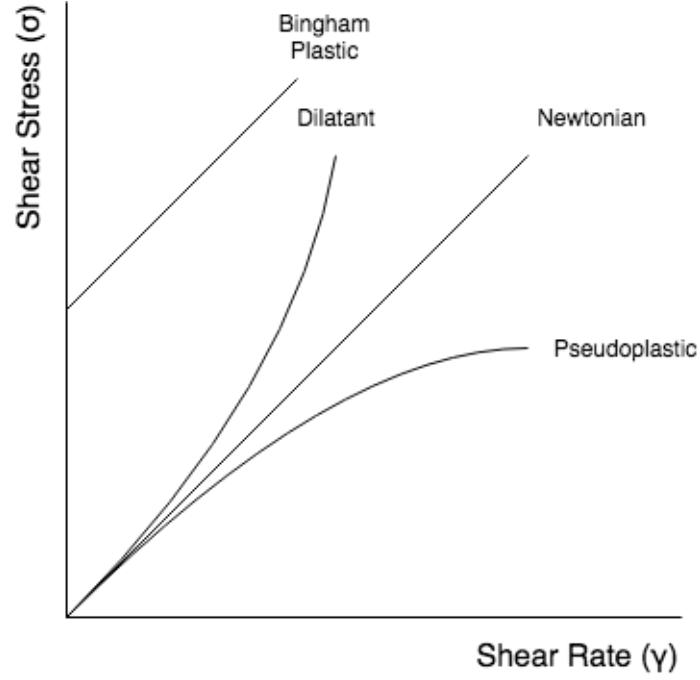


Figure 2.2: The stress-strain relationships for different kinds of fluids (source [REF])

Thus, for a power law fluid, we require that:

$$\frac{1}{6}\tau_1\rho_0c_s^2 = K|\dot{\gamma}|^{n-1} \quad (2.97)$$

Taking moduli of both sides of (2.96), we also have:

$$|\sigma| = \frac{1}{6}\tau_1\rho_0c_s^2|\dot{\gamma}| \quad (2.98)$$

Combining these two relationships, we obtain:

$$\tau_1 = \frac{6K^{\frac{1}{n}}}{\rho_0c_s^2} \left| \frac{1}{\sigma} \right|^{\frac{1-n}{n}} := \tau_0 \left| \frac{1}{\sigma} \right|^{\frac{1-n}{n}} \quad (2.99)$$

Take the singular value decomposition $A = U\Sigma V^T$. Note that:

$$\sigma = -\rho c_s^2 A^T A \operatorname{dev} (A^T A) = -\rho c_s^2 V \Sigma^2 \operatorname{dev} (\Sigma^2) V^T \quad (2.100)$$

Thus:

$$\|\sigma\|_F^k = \rho^k c_s^{2k} \|\Sigma^2 \operatorname{dev}(\Sigma^2)\|_F^k \quad (2.101)$$

Letting $k = \frac{1-n}{n}$:

$$\frac{d\Sigma}{dt} = -\frac{3}{\tau_0} \left(\frac{\rho}{\rho_0}\right)^{\frac{5}{3}} \frac{\rho^k c_s^{2k}}{2^{\frac{k}{2}}} \|\Sigma^2 \operatorname{dev}(\Sigma^2)\|_F^k \Sigma \operatorname{dev}(\Sigma^2) \quad (2.102)$$

Letting $x_i = \frac{a_i^2}{\det(A)^{\frac{2}{3}}} = \frac{a_i^2}{\left(\frac{\rho}{\rho_0}\right)^{\frac{2}{3}}}$ then $\Sigma^2 = \det(A)^{\frac{2}{3}} X$ where $X = \operatorname{diag}(x_1, x_2, x_3)$. Thus, we have:

$$\frac{dx_i}{d\tilde{t}} = -3 \|X \operatorname{dev}(X)\|_F^k x_i (x_i - \bar{x}) \quad (2.103)$$

where:

$$\tilde{t} = \frac{2}{\tau_0} \left(\frac{\rho}{\rho_0}\right)^{\frac{4k+7}{3}} \left(\frac{\rho c_s^2}{\sqrt{2}}\right)^k t \quad (2.104)$$

Note that:

$$\begin{aligned} 9 \|X \operatorname{dev}(X)\|_F^2 &= 4(x_1^4 + x_2^4 + x_3^4) \\ &+ 2(x_2 x_3 x_1^2 + x_2 x_3^2 x_1 + x_2^2 x_3 x_1) \\ &- 2(x_1^2 x_2^2 + x_3^2 x_2^2 + x_1^2 x_3^2) \\ &- 4(x_2 x_1^3 + x_3 x_1^3 + x_2^3 x_1 + x_3^3 x_1 + x_2 x_3^3 + x_2^3 x_3) \end{aligned} \quad (2.105)$$

Defining m, u as before, we have:

$$\|X \operatorname{dev}(X)\|_F^2 = \frac{1}{2} u^2 + 4m^2 u - 6m^4 + 6m \quad (2.106)$$

This leads to the following coupled system of ODEs:

$$\frac{du}{d\tilde{t}} = -18 \left(\frac{1}{2} u^2 + 4m^2 u - 6m^4 + 6m\right)^{\frac{k}{2}} \left(1 - m \left(m^2 - \frac{5}{6} u\right)\right) \quad (2.107a)$$

$$\frac{dm}{d\tilde{t}} = -\left(\frac{1}{2} u^2 + 4m^2 u - 6m^4 + 6m\right)^{\frac{k}{2}} u \quad (2.107b)$$

Define the the variable τ by:

$$\frac{d\tau}{d\tilde{t}} = \left(\frac{1}{2}u^2 + 4m^2u - 6m^4 + 6m \right)^{\frac{n}{2}} \quad (2.108)$$

$$m(\tau) = 1 + \frac{e^{-9\tau}}{3} (ae^{3\tau} - b) \quad (2.109a)$$

$$u(\tau) = e^{-9\tau} (2ae^{3\tau} - 3b) \quad (2.109b)$$

It is straightforward to verify that:

$$\frac{d\tau}{d\tilde{t}} = \frac{1}{54^{\frac{k}{2}}} \begin{pmatrix} 108ae^{-6\tau} - 324be^{-9\tau} + 180a^2e^{-12\tau} \\ -612abe^{-15\tau} + 459b^2e^{-18\tau} - 24a^2be^{-21\tau} \\ + (48ab^2 - 4a^4)e^{-24\tau} + (16a^3b - 24b^3)e^{-27\tau} \\ -24a^2b^2e^{-30\tau} + 16ab^3e^{-33\tau} - 4b^4e^{-36\tau} \end{pmatrix}^{\frac{k}{2}} \equiv \frac{f(\tau)^{\frac{k}{2}}}{54^{\frac{k}{2}}} \quad (2.110)$$

$f(\tau)$ is approximated by $g(\tau) \equiv ce^{-\lambda\tau}$, where:

$$c = 108a - 324b + 180a^2 - 612ab + 459b^2 - 24(a^2b - 2ab^2 + b^3) - 4(a - b)^4 \quad (2.111a)$$

$$\lambda = \frac{c}{18a - 36b + 15a^2 - \frac{204ab}{5} + \frac{51b^2}{2} - \frac{8a^2b}{7} + 2ab^2 - \frac{8b^3}{9} - \frac{a^4}{6} + \frac{16a^3b}{27} - \frac{4a^2b^2}{5} + \frac{16ab^3}{33} - \frac{b^4}{9}} \quad (2.111b)$$

Note that $f(0) = g(0)$ and $\int_0^\infty (f(\tau) - g(\tau)) d\tau = 0$. Thus, we have:

$$\frac{d\tau}{d\tilde{t}} \approx \left(\frac{c}{54} \right)^{\frac{k}{2}} e^{-\frac{k\lambda}{2}\tau} \quad (2.112)$$

Therefore:

$$\begin{aligned} \tau &\approx \frac{2}{k\lambda} \log \left(\frac{k\lambda}{2} \left(\frac{c}{54} \right)^{\frac{k}{2}} \tilde{t} + 1 \right) \\ &= \frac{2}{k\lambda} \log \left(\frac{k\lambda}{\tau_0} \left(\frac{\rho}{\rho_0} \right)^{\frac{4k+7}{3}} \left(\frac{\sqrt{c}\rho c_s^2}{6\sqrt{3}} \right)^k t + 1 \right) \end{aligned} \quad (2.113)$$

2.2.3.4 Elastoplastic Solids

For elastoplastic materials governed by the power law described in (12a):

$$\frac{d\Sigma}{dt} = -\frac{3}{\tau_0} \left(\frac{\rho}{\rho_0} \right)^{\frac{5}{3}} \frac{\left(\frac{3}{2} \right)^{\frac{n}{2}} \rho^n c_s^{2n} \|\text{dev}(\Sigma^2 \text{dev}(\Sigma^2))\|_F^n}{\sigma_0^n} \Sigma \text{dev}(\Sigma^2) \quad (2.114)$$

Thus, we have:

$$\frac{dx_i}{d\tilde{t}} = -3 \|\text{dev}(X \text{dev}(X))\|_F^n x_i (x_i - \bar{x}) \quad (2.115)$$

where:

$$\tilde{t} = \frac{2}{\tau_0} \left(\frac{\rho}{\rho_0} \right)^{\frac{4n+7}{3}} \left(\sqrt{\frac{3}{2}} \frac{\rho c_s^2}{\sigma_0} \right)^n t \quad (2.116)$$

Note that:

$$\begin{aligned} \frac{27}{2} \|\text{dev}(X \text{dev}(X))\|_F^2 &= 3 \left(x_2 x_3 x_1^2 + x_2 x_3^2 x_1 + x_2^2 x_3 x_1 \right) \\ &\quad - 3 \left(x_1^2 x_2^2 + x_3^2 x_2^2 + x_1^2 x_3^2 \right) \\ &\quad - 2 \left(x_2 x_1^3 + x_3 x_1^3 + x_2^3 x_1 + x_3^3 x_1 + x_2 x_3^3 + x_2^3 x_3 \right) \\ &\quad + 4 \left(x_1^4 + x_2^4 + x_3^4 \right) \end{aligned} \quad (2.117)$$

Thus we have:

$$\|\text{dev}(X \text{dev}(X))\|_F^2 = \frac{1}{6} u^2 + 4m^2 u - 6m^4 + 6m \quad (2.118)$$

This leads to the following coupled system of ODEs:

$$\frac{du}{d\tilde{t}} = -18 \left(\frac{1}{6} u^2 + 4m^2 u - 6m^4 + 6m \right)^{\frac{n}{2}} \left(1 - m \left(m^2 - \frac{5}{6} u \right) \right) \quad (2.119a)$$

$$\frac{dm}{d\tilde{t}} = - \left(\frac{1}{6} u^2 + 4m^2 u - 6m^4 + 6m \right)^{\frac{n}{2}} u \quad (2.119b)$$

Define the the variable τ by:

$$\frac{d\tau}{d\tilde{t}} = \left(\frac{1}{6}u^2 + 4m^2u - 6m^4 + 6m \right)^{\frac{n}{2}} \quad (2.120)$$

Then we have:

$$\frac{du}{d\tau} = -18 \left(1 - m \left(m^2 - \frac{5}{6}u \right) \right) \quad (2.121a)$$

$$\frac{dm}{d\tau} = -u \quad (2.121b)$$

Using the approximate solution from before:

$$m(\tau) = 1 + \frac{e^{-9\tau}}{3} \left((9m_0 - u_0 - 9)e^{3\tau} - (6m_0 - u_0 - 6) \right) \quad (2.122a)$$

$$u(\tau) = e^{-9\tau} \left(e^{3\tau} (18m_0 - 2u_0 - 18) - (18m_0 - 3u_0 - 18) \right) \quad (2.122b)$$

Denoting $a = 9m_0 - u_0 - 9$, $b = 6m_0 - u_0 - 6$, it is straightforward to verify that:

$$\frac{d\tau}{d\tilde{t}} = \frac{1}{54^{\frac{n}{2}}} \left(\begin{array}{c} 108ae^{-6\tau} - 324be^{-9\tau} + 108a^2e^{-12\tau} \\ -396abe^{-15\tau} + 297b^2e^{-18\tau} - 24a^2be^{-21\tau} \\ + (48ab^2 - 4a^4)e^{-24\tau} + (16a^3b - 24b^3)e^{-27\tau} \\ -24a^2b^2e^{-30\tau} + 16ab^3e^{-33\tau} - 4b^4e^{-36\tau} \end{array} \right)^{\frac{n}{2}} \equiv \frac{f(\tau)^{\frac{n}{2}}}{54^{\frac{n}{2}}} \quad (2.123)$$

$f(\tau)$ is approximated by $g(\tau) \equiv ce^{-\lambda\tau}$, where:

$$c = 108a - 324b + 108a^2 - 396ab + 297b^2 - 24(a^2b - 2ab^2 + b^3) - 4(a - b)^4 \quad (2.124a)$$

$$\lambda = \frac{c}{18a - 36b + 9a^2 - \frac{132ab}{5} + \frac{33b^2}{2} - \frac{8a^2b}{7} + 2ab^2 - \frac{8b^3}{9} - \frac{a^4}{6} + \frac{16a^3b}{27} - \frac{4a^2b^2}{5} + \frac{16ab^3}{33} - \frac{b^4}{9}} \quad (2.124b)$$

Note that $f(0) = g(0)$ and $\int_0^\infty (f(\tau) - g(\tau)) d\tau = 0$. Thus, we have:

$$\frac{d\tau}{d\tilde{t}} \approx \left(\frac{c}{54} \right)^{\frac{n}{2}} e^{-\frac{n\lambda}{2}\tau} \quad (2.125)$$

Therefore:

$$\begin{aligned}\tau &\approx \frac{2}{n\lambda} \log \left(\frac{n\lambda}{2} \left(\frac{c}{54} \right)^{\frac{n}{2}} \tilde{t} + 1 \right) \\ &= \frac{2}{n\lambda} \log \left(\frac{n\lambda}{\tau_0} \left(\frac{\rho}{\rho_0} \right)^{\frac{4n+7}{3}} \left(\frac{\sqrt{c}}{6} \frac{\rho c_s^2}{\sigma_0} \right)^n t + 1 \right)\end{aligned}\quad (2.126)$$

Thus, the value of A at time Δt is found by substituting the following into (2.122a),(2.122b):

$$\tau = \frac{2}{n\lambda} \log \left(\frac{n\lambda}{\tau_0} \left(\frac{\rho}{\rho_0} \right)^{\frac{4n+7}{3}} \left(\frac{\sqrt{c}}{6} \frac{\rho c_s^2}{\sigma_0} \right)^n \Delta t + 1 \right) \quad (2.127)$$

The results are in turn substituted into (2.92a), (2.90b), (2.90c).

2.2.4 Distortion Correction in Fluids

Owing to the linearization step in (2.86), the method presented will perform poorly if the mean of the normalized singular values of the distortion tensor, m , deviates significantly from 1. To avert this, the following resetting procedure was applied globally for fluid flow problems when $m > 1.03$:

$$E \mapsto E - \frac{c_s^2}{4} \|\text{dev}(G)\|_F^2 \quad (2.128a)$$

$$A \mapsto \left(\frac{\rho}{\rho_0} \right)^{1/3} I \quad (2.128b)$$

This is justified by the fact that the distortion tensor is not a macroscopically-measurable quantity. This transformation leaves the density, pressure, and velocity of the fluid unchanged, and was found to improve the stability of the numerical scheme, while at the same time producing correct results, as demonstrated in the following section.

	ρ	p	\mathbf{v}	A	\mathbf{J}
$x < 0$	1	$1/\gamma$	$(0, -0.1, 0)$	I_3	$\mathbf{0}$
$x \geq 0$	1	$1/\gamma$	$(0, 0.1, 0)$	I_3	$\mathbf{0}$

Table 2.1: Initial conditions for the slow opposing shear flow test

2.3 Numerical Results

2.3.1 Newtonian Fluids & Elastic Solids

2.3.1.1 Strain Relaxation

In this section, the approximate analytic solver for the distortion ODEs, presented in 2.2.3.2, is compared with a numerical ODE solver. Initial data was taken from [6]:

$$A = \begin{pmatrix} 1 & 0 & 0 \\ -0.01 & 0.95 & 0.02 \\ -0.015 & 0 & 0.9 \end{pmatrix}^{-1} \quad (2.129)$$

Additionally, the following parameter values were used: $\rho_0 = 1, c_s = 1, \mu = 10^{-2}$, giving $\tau_1 = 0.06$. As can be seen in Figure 2.3 on page 58, Figure 2.4 on page 58, and Figure 2.5 on page 58, the approximate analytic solver compares well with the numerical solver in its results for the distortion tensor A , and thus also the internal energy and stress tensor. The numerical ODE solver was the odeint solver from SciPy 0.18.1, based on the LSODA solver from the FORTRAN library ODEPACK (see [58]).

2.3.1.2 Stokes' First Problem

This problem is one of the few test cases with an analytic solution for the Navier-Stokes equations. It consists of two ideal gases in an infinite domain, meeting at the plane $x = 0$, initially flowing with equal and opposite velocity ± 0.1 in the y -axis. The initial conditions are given in Table 2.1 on page 57.

The flow has a low Mach number of 0.1, and this test case is designed to demonstrate the efficacy of the numerical methods in this flow regime. The exact solution to the Navier-Stokes

2.3 Numerical Results

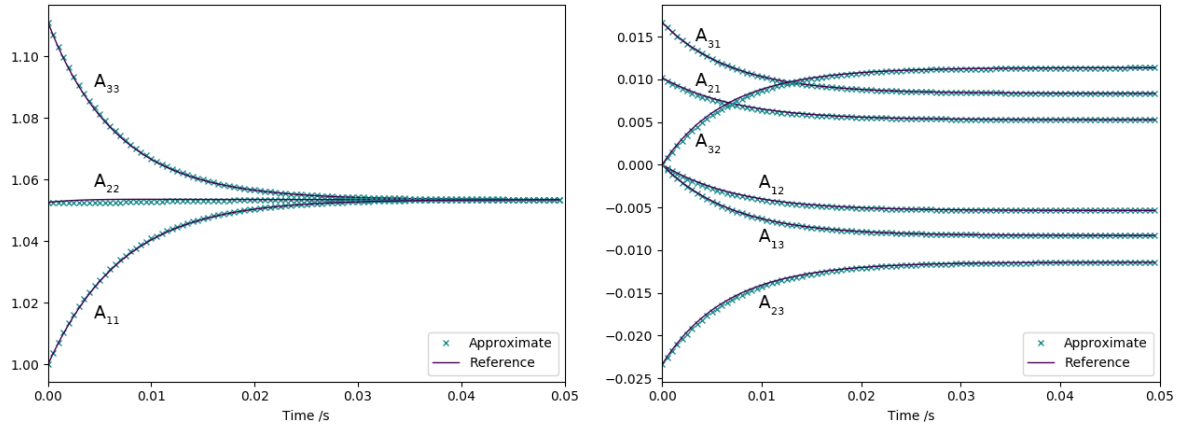


Figure 2.3: The components of the distortion tensor in the Strain Relaxation Test

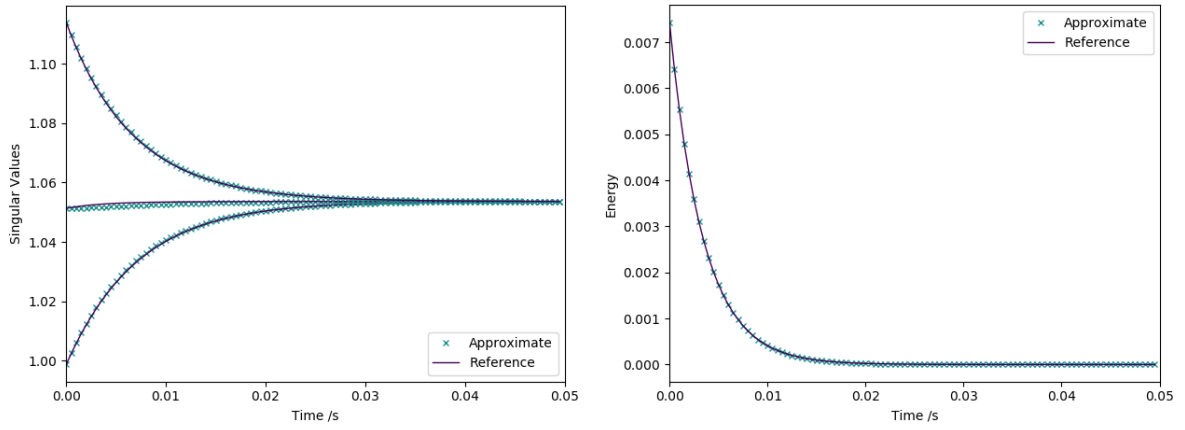


Figure 2.4: The singular values of the distortion tensor and the energy in the Strain Relaxation Test

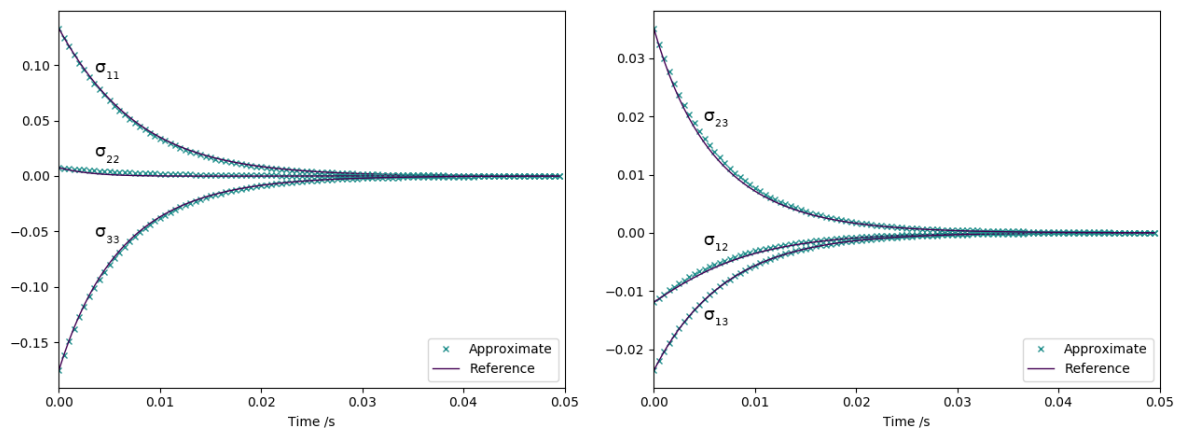


Figure 2.5: The components of the stress tensor in the Strain Relaxation Test

equations is given by¹:

$$v = v_0 \operatorname{erf} \left(\frac{x}{2\sqrt{\mu t}} \right) \quad (2.130)$$

Heat conduction is neglected, and $\gamma = 1.4$, $c_v = 1$, $\rho_0 = 1$, $c_s = 1$. The viscosity is variously taken to be $\mu = 10^{-2}$, $\mu = 10^{-3}$, $\mu = 10^{-4}$ (resulting in $\tau_1 = 0.06$, $\tau_1 = 0.006$, $\tau_1 = 0.0006$, respectively). Due to the stiffness of the source terms in the equations governing A in the case that $\mu = 10^{-4}$, the step (2.45) in the WENO reconstruction under the Split-WENO method was not performed, and $w_p^{n+\frac{1}{2}} \equiv w_p^n$ was taken instead. This avoided the numerical diffusion that otherwise would have emerged at the interface at $x = 0$.

The results of simulations with 200 cells at time $t = 1$, using reconstruction polynomials of order $N = 2$, are presented in Figure 2.6 on page 60. The GPR model solved with both the ADER-WENO and Split-WENO methods closely matches the exact Navier-Stokes solution. Note that at $\mu = 10^{-2}$ and $\mu = 10^{-3}$, the ADER-WENO and Split-WENO methods are almost indistinguishable. At $\mu = 10^{-4}$ the Split-WENO method matches the curve of the velocity profile more closely, but overshoots slightly at the boundaries of the center region. This overshoot phenomenon is not visible in the ADER-WENO results.

2.3.1.3 Viscous Shock

This test is designed to demonstrate that the numerical methods used are also able to cope with fast flows. First demonstrated by Becker [10], the Navier-Stokes equations have an analytic solution for $P_r = 0.75$ (see Johnson [42] for a full analysis). As noted by Dumbser et al. [24], if the wave has nondimensionalised upstream velocity $\bar{v} = 1$ and Mach number M_c , then its nondimensionalised downstream velocity is:

$$a = \frac{1 + \frac{\gamma-1}{2} M_c^2}{\frac{\gamma+1}{2} M_c^2} \quad (2.131)$$

¹In this problem, the Navier-Stokes equations reduce to $v_t = \mu v_{xx}$. Defining $\eta = \frac{x}{2\sqrt{\mu t}}$, and assuming $v = f(\eta)$, this becomes $f'' + 2\eta f' = 0$. The result follows by solving this equation with the boundary conditions $v(\pm\infty) = \pm v_0$.

2.3 Numerical Results

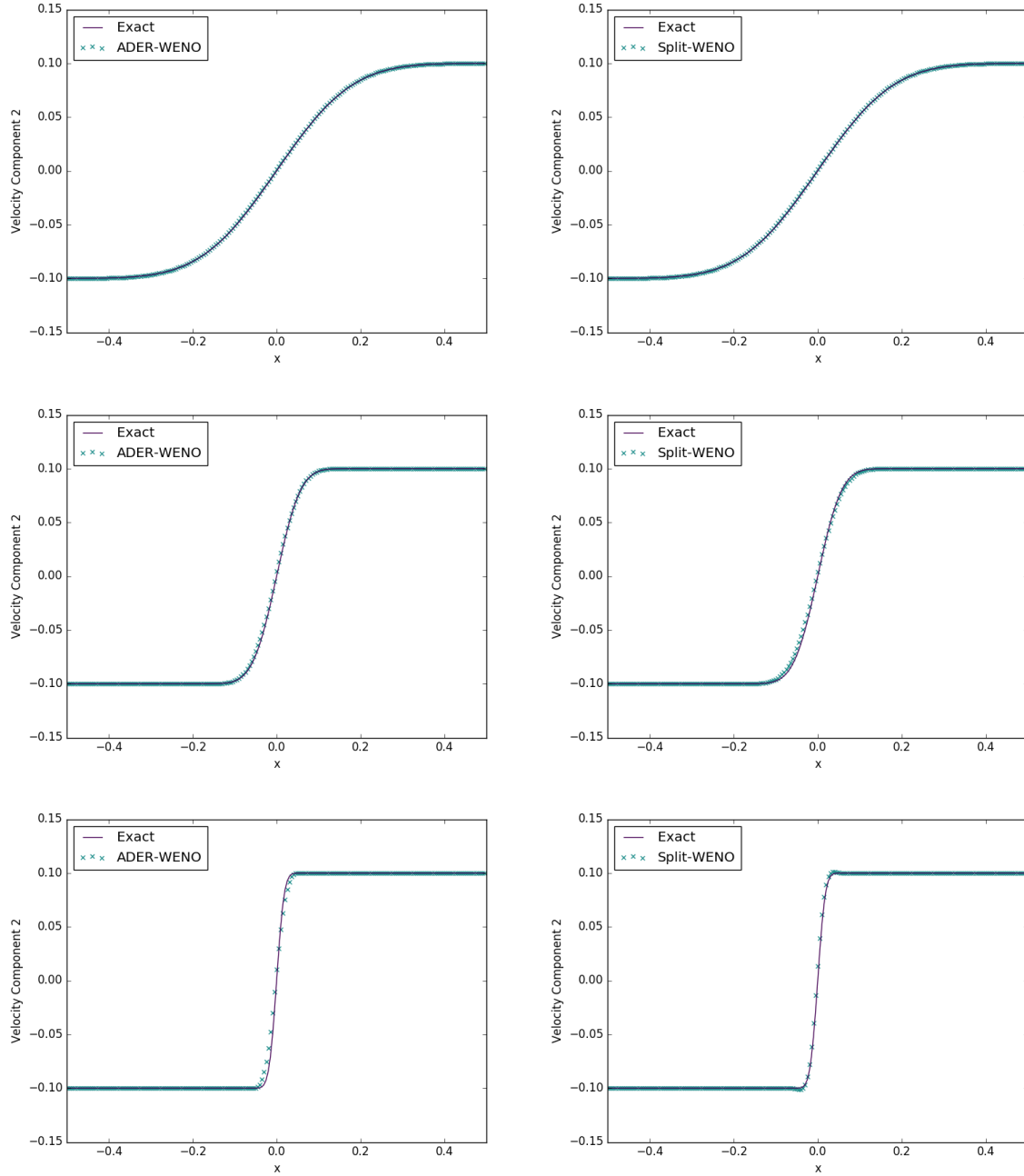


Figure 2.6: Results of solving Stokes' First Problem ($\mu = 10^{-2}, \mu = 10^{-3}, \mu = 10^{-4}$) with an ADER-WENO scheme and a Split-WENO scheme ($N = 2$)

The wave's velocity profile $\bar{v}(x)$ is given by the roots of the following equation:

$$\frac{1 - \bar{v}}{(\bar{v} - a)^a} = c_1 \exp(-c_2 x) \quad (2.132a)$$

$$c_1 = \left(\frac{1 - a}{2} \right)^{1-a} \quad (2.132b)$$

$$c_2 = \frac{3}{4} R_e \frac{M_c^2 - 1}{\gamma M_c^2} \quad (2.132c)$$

c_1, c_2 are constants that affect the position of the center of the wave, and its stretch factor, respectively. Following the analysis of Morduchow and Libby [55], the nondimensional pressure and density profiles are given by:

$$\bar{p} = \frac{1}{\bar{v}} \left(1 + \frac{\gamma - 1}{2} M_c^2 (1 - \bar{v}^2) \right) \quad (2.133)$$

$$\bar{\rho} = \frac{1}{\bar{v}} \quad (2.134)$$

To obtain an unsteady shock traveling into a region at rest, a constant velocity field $v = M_c c_0$ is imposed on the traveling wave solution presented here (where c_0 is the adiabatic sound speed). Thus, if p_0, ρ_0 are the downstream (reference) values for pressure and density:

$$v = M_c c_0 (1 - \bar{v}) \quad (2.135a)$$

$$p = p_0 \bar{p} \quad (2.135b)$$

$$\rho = \rho_0 \bar{\rho} \quad (2.135c)$$

These functions are used as initial conditions, along with $A = \sqrt[3]{\bar{\rho}} I$ and $\mathbf{J} = \mathbf{0}$. The downstream density and pressure are taken to be $\rho_0 = 1$ and $p_0 = \frac{1}{\gamma}$ (so that $c_0 = 1$). $M_c = 2$ and $R_e = 100$. The material parameters are taken to be: $\gamma = 1.4$, $p_\infty = 0$, $c_v = 2.5$, $c_s = 5$, $c_t = 5$, $\mu = 2 \times 10^{-2}$, $\kappa = \frac{28}{3} \times 10^{-2}$ (resulting in $\tau_1 = 0.0048$, $\tau_2 = 0.00522\dot{6}$).

The results of a simulation with 200 cells at time $t = 0.2$, using reconstruction polynomials of order $N = 2$, are presented in Figure 2.7 on page 63 and Figure 2.8 on page 64. The shock was initially centered at $x = 0.25$, reaching $x = 0.65$ at the final time. Note that the density, velocity, and pressure results for both methods match the exact solution well,

	ρ	p	\mathbf{v}	A	\mathbf{J}
$x < 0$	2	1	$\mathbf{0}$	$\sqrt[3]{2} \cdot I_3$	$\mathbf{0}$
$x \geq 0$	0.5	1	$\mathbf{0}$	$\frac{1}{\sqrt[3]{2}} \cdot I_3$	$\mathbf{0}$

Table 2.2: Initial conditions for the heat conduction test

with the ADER-WENO method appearing to produce a slightly more accurate solution. The results for the two methods for the stress tensor and heat flux are close.

2.3.1.4 Heat Conduction in a Gas

This is a simple test case to ensure that the heat transfer terms in the implementation are working correctly. Two ideal gases at different temperatures are initially in contact at position $x = 0$. The initial conditions for this problem are given in Table 2.2 on page 62.

The material parameters are taken to be: $\gamma = 1.4$, $c_v = 2.5$, $\rho_0 = 1$, $p_0 = 1$, $c_s = 1$, $c_t = 2$, $\mu = 10^{-2}$, $\kappa = 10^{-2}$ (resulting in $\tau_1 = 0.06$, $\tau_2 = 0.0025$). The results of a simulation with 200 cells at time $t = 1$, using reconstruction polynomials of order $N = 2$, are presented in Figure 2.9 on page 64. The ADER-WENO and Split-WENO methods are in perfect agreement for both the temperature and heat flux profiles. As demonstrated in [24], this means that they in turn agree very well with a reference Navier-Stokes-Fourier solution.

2.3.1.5 Elastic Riemann Problems

These tests are taken from [13].

2.3.1.6 Speed

Both the ADER-WENO scheme and the Split-WENO scheme used in this study were implemented in Python3. All array functions were precompiled with Numba's JIT capabilities and the root-finding procedure in the Galerkin predictor was performed using SciPy's Newton-Krylov solver, compiled against the Intel MKL. Clear differences in computational cost between the ADER-WENO and Split-WENO methods were apparent, as is to be expected, owing to the lack of Galerkin method in the Split-WENO scheme. The wall times

2.3 Numerical Results

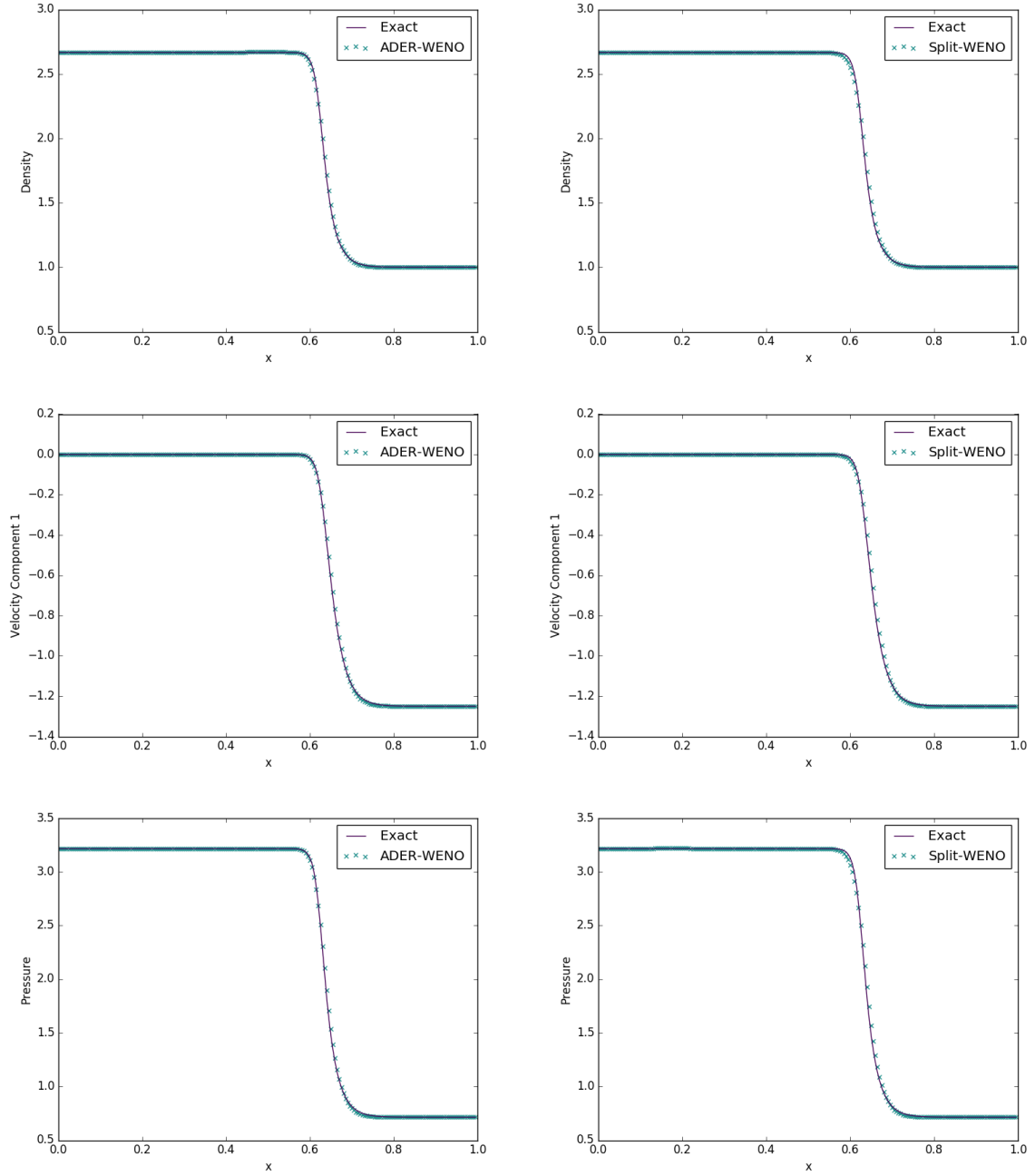


Figure 2.7: Density, velocity, and pressure for the Viscous Shock problem, solved with an ADER-WENO scheme and a Split-WENO scheme ($N = 2$)

2.3 Numerical Results

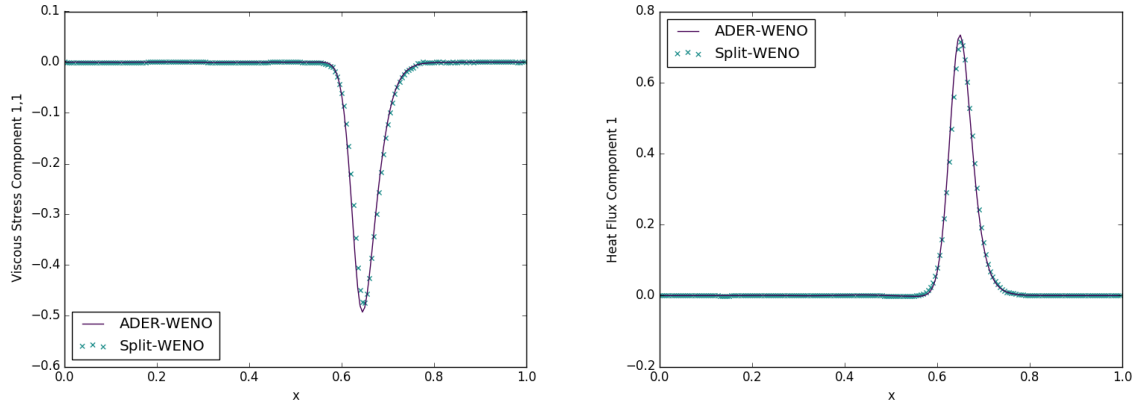


Figure 2.8: Viscous stress and heat flux for the Viscous Shock problem, solved with both an ADER-WENO scheme and a Split-WENO scheme ($N = 2$)

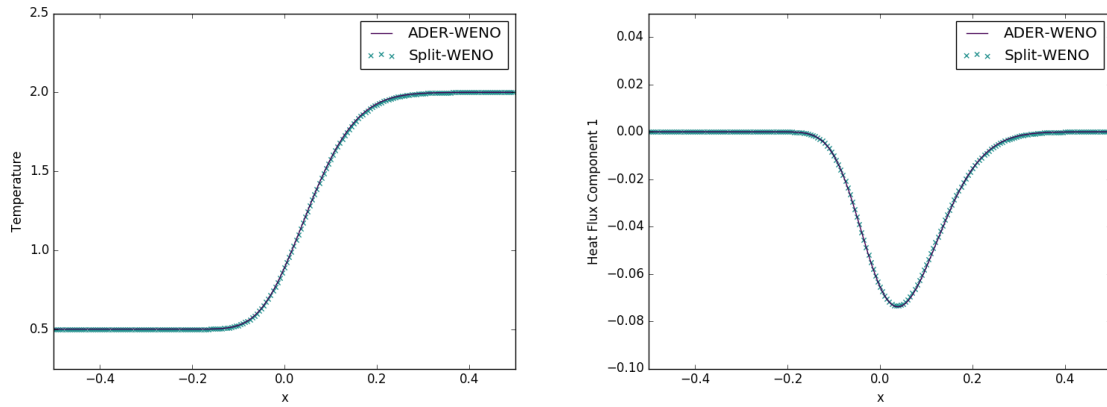


Figure 2.9: Results of solving the problem of Heat Conduction in Gas with both an ADER-WENO scheme and a Split-WENO scheme ($N = 2$)

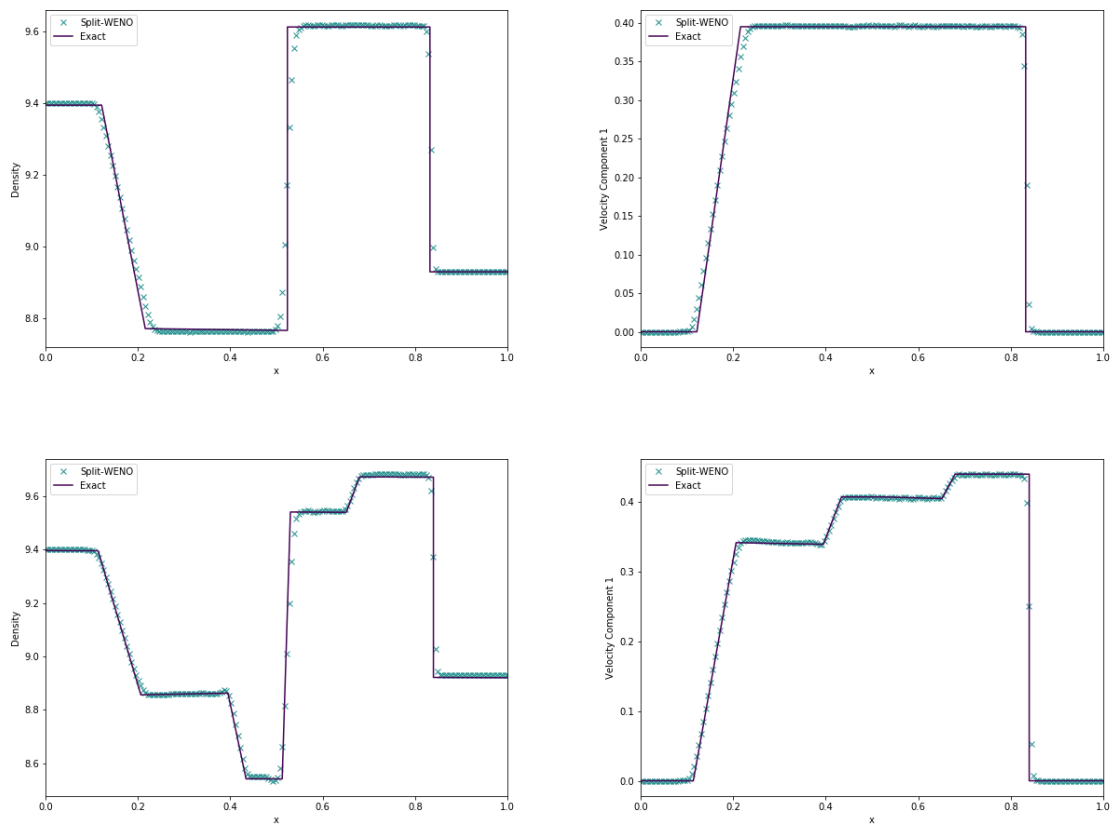


Figure 2.10: Results for the 3-wave and 5-wave purely elastic Riemann problems

for the various tests undertaken in this study are given in Table 2.3 on page 68, comparing the combined WENO and Galerkin methods of the ADER-WENO scheme to the combined WENO and ODE methods of the Split-WENO scheme. All computations were performed using an Intel Core i7-4910MQ, on a single core. The number of time steps taken are given in Table 2.4 on page 68. The differences between the methods in terms of the number of time steps taken in each test result from the fact that, for numerical stability, CFL numbers of 0.8 and 0.7 were required by the ADER-WENO method and the Split-WENO method, respectively.

Note that, unlike with the ADER-WENO scheme, the wall time for the Split-WENO scheme is unaffected by a decrease in the viscosity in Stokes' First Problem (and the corresponding increase in the stiffness of the source terms). This is because the analytic approximation to the distortion ODEs obviates the need for a stiff solver. The large difference in ADER-WENO solver times between the $\mu = 10^{-3}$ and $\mu = 10^{-4}$ cases is due to the fact that, in the latter case, a stiff solver must be employed for the initial guess to the root of the nonlinear system produced by the Discontinuous Galerkin method (as described in [38]).

2.3.1.7 Convergence

To assess the rate of convergence of the Split-WENO method, the convected isentropic vortex convergence study from [24] was performed. The initial conditions are given as $\rho = 1 + \delta\rho$, $p = 1 + \delta p$, $\mathbf{v} = (1, 1, 0) + \delta\mathbf{v}$, $A = \sqrt[3]{\rho}I$, $\mathbf{J} = \mathbf{0}$, where:

$$\delta T = -\frac{(\gamma - 1)\epsilon^2}{8\gamma\pi^2}e^{1-r^2} \quad (2.136a)$$

$$\delta\rho = (1 + \delta T)^{\frac{1}{\gamma-1}} - 1 \quad (2.136b)$$

$$\delta p = (1 + \delta T)^{\frac{\gamma}{\gamma-1}} - 1 \quad (2.136c)$$

$$\delta\mathbf{v} = \frac{\epsilon}{2\pi}e^{\frac{1-r^2}{2}} \begin{pmatrix} -(y-5) \\ x-5 \\ 0 \end{pmatrix} \quad (2.136d)$$

The 2D domain is taken to be $[0, 10]^2$. ϵ is taken to be 5. The material parameters are taken to be: $\gamma = 1.4$, $c_v = 2.5$, $\rho_0 = 1$, $p_0 = 1$, $c_s = 0.5$, $c_t = 1$, $\mu = 10^{-6}$, $\kappa = 10^{-6}$ (resulting in $\tau_1 = 2.4 \times 10^{-5}$, $\tau_2 = 10^{-6}$). Thus, this can be considered to be a stiff test case.

The convergence rates in the L_1 , L_2 , L_∞ norms for the density variable are given in Table 2.5 on page 68 and Table 2.6 on page 68 for WENO reconstruction polynomial orders of $N = 2$ and $N = 3$, respectively. As expected, both sets of tests attain roughly second order convergence. For comparison, the corresponding results for this test from [24] - solved using a third-order P2P2 scheme - are given in Table 2.7 on page 69 for comparison.

2.3.2 Non-Newtonian Fluids & Elastoplastic Solids

2.3.2.1 Strain Relaxation Test

Take initial data used by Barton:

$$A = \begin{pmatrix} 1 & 0 & 0 \\ -0.01 & 0.95 & 0.02 \\ -0.015 & 0 & 0.9 \end{pmatrix}^{-1} \quad (2.137)$$

The following parameter values were used: $\rho_0 = 1$, $c_s = 0.219$, $n = 4$, $\sigma_0 = 9 \times 10^{-4}$, $\tau_0 = 0.1$. As can be seen in Figure 2.11 on page 69, Figure 2.12 on page 69, and Figure 2.13 on page 71, the approximate analytic solver compares well with the exact solution for the distortion tensor A , and thus also the stress tensor and the energy.

2.3.2.2 Poiseuille Flow

This test consists of a fluid traveling down a channel of constant width L , with a constant pressure gradient Δp along the length of the channel. No-slip boundary conditions are imposed on the channel walls. For a non-Newtonian fluid obeying a power law, the steady-state velocity profile across the channel is given by [30]:

$$v = \frac{\rho}{k} \left(\frac{\Delta p}{K} \right)^{1/n} \left(\left(\frac{L}{2} \right)^k - \left(x - \frac{L}{2} \right)^k \right) \quad (2.138a)$$

$$k = \frac{n+1}{n} \quad (2.138b)$$

where $x \in [0, L]$.

2.3 Numerical Results

	ADER-WENO	Split-WENO	Speed-up
Stokes' First Problem ($\mu = 10^{-2}$)	265s	38s	7.0
Stokes' First Problem ($\mu = 10^{-3}$)	294s	38s	7.7
Stokes' First Problem ($\mu = 10^{-4}$)	536s	38s	14.1
Viscous Shock	297s	56s	5.3
Heat Conduction in a Gas	544s	94s	5.8

Table 2.3: Wall time for various tests (all with 200 cells) under the ADER-WENO method and the Split-WENO method

	Timesteps (ADER-WENO)	Timesteps (Split-WENO)
Stokes' First Problem ($\mu = 10^{-2}$)	385	442
Stokes' First Problem ($\mu = 10^{-3}$)	386	443
Stokes' First Problem ($\mu = 10^{-4}$)	385	442
Viscous Shock	562	645
Heat Conduction in a Gas	942	1077

Table 2.4: Time steps taken for various tests (all with 200 cells) under the ADER-WENO method and the Split-WENO method

Grid Size	$\epsilon(L_1)$	$\epsilon(L_2)$	$\epsilon(L_\infty)$	$\mathcal{O}(L_1)$	$\mathcal{O}(L_2)$	$\mathcal{O}(L_\infty)$
20	2.87×10^{-3}	7.15×10^{-3}	6.21×10^{-2}			
40	5.81×10^{-4}	1.62×10^{-3}	1.73×10^{-2}	2.30	2.14	1.85
60	1.98×10^{-4}	5.39×10^{-4}	5.94×10^{-3}	2.65	2.70	2.63
80	1.23×10^{-4}	3.47×10^{-4}	3.41×10^{-3}	1.67	1.52	1.92

Table 2.5: Convergence rates for the Split-WENO method ($N = 2$)

Grid Size	$\epsilon(L_1)$	$\epsilon(L_2)$	$\epsilon(L_\infty)$	$\mathcal{O}(L_1)$	$\mathcal{O}(L_2)$	$\mathcal{O}(L_\infty)$
10	1.01×10^{-2}	2.58×10^{-2}	1.27×10^{-1}			
20	1.68×10^{-3}	4.02×10^{-3}	2.93×10^{-2}	2.59	2.68	2.11
30	5.34×10^{-4}	1.57×10^{-3}	1.70×10^{-2}	2.83	2.32	1.34
40	3.32×10^{-4}	8.94×10^{-4}	7.55×10^{-3}	1.65	1.95	2.82

Table 2.6: Convergence rates for the Split-WENO method ($N = 3$)

Grid Size	$\epsilon(L_1)$	$\epsilon(L_2)$	$\epsilon(L_\infty)$	$\mathcal{O}(L_1)$	$\mathcal{O}(L_2)$	$\mathcal{O}(L_\infty)$
20	9.44×10^{-3}	2.20×10^{-3}	2.16×10^{-3}			
40	1.95×10^{-3}	4.50×10^{-4}	4.27×10^{-4}	2.27	2.29	2.34
60	7.52×10^{-4}	1.74×10^{-4}	1.48×10^{-4}	2.35	2.35	2.61
80	3.72×10^{-4}	8.66×10^{-5}	7.40×10^{-5}	2.45	2.42	2.41

Table 2.7: Convergence rates for the ADER-DG PNPM method ($N, M = 2$)

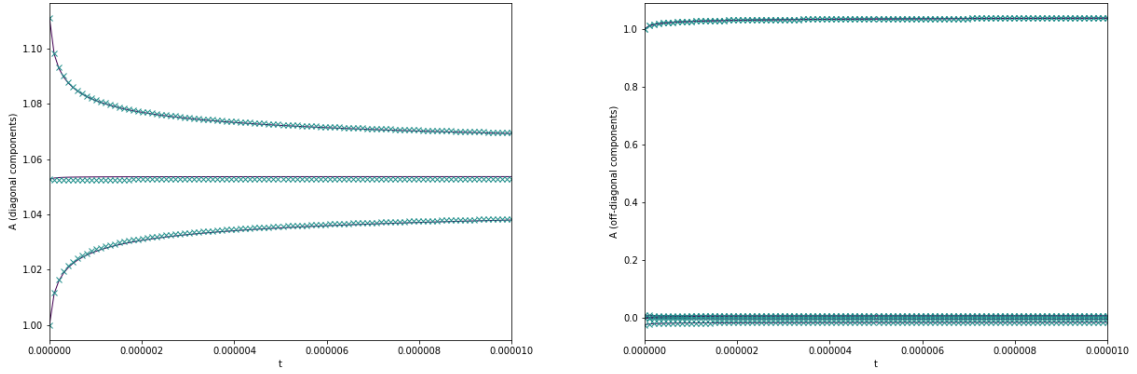


Figure 2.11: Components of the distortion tensor during the Strain Relaxation Test: approximate analytical solution (crosses) is compared with numerical ODE solution (solid line)

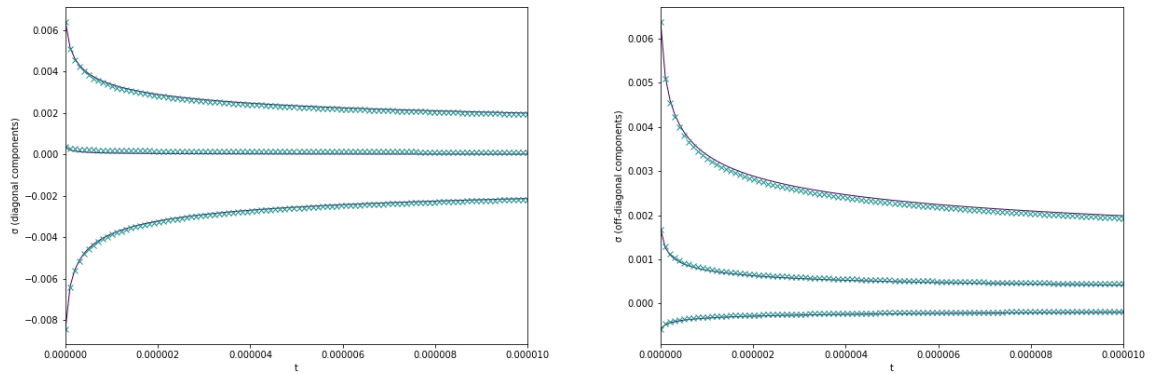


Figure 2.12: Stress tensor during the Strain Relaxation Test: approximate analytical solution (crosses) is compared with numerical ODE solution (solid line)

In this case, $L = 0.25$, $\Delta p = 0.48$, $K = 10^{-2}$. The fluid is initially at rest, with $\rho_0 = 1$, $A = I$, $p = 100/\gamma$. It follows an ideal gas EOS with $\gamma = 1.4$, $c_s = 1$. The pressure gradient is imposed by means of a body force, implemented as a constant source term to the momentum equation. The final time was taken to be 20, with 100 cells taken across the width of the channel.

Results for various values of n are shown in Figure 2.14 on page 71. The exact solutions are shown as dotted lines, with the numerical solutions in solid colors.

2.3.2.3 Lid-Driven Cavity

As detailed in [68], this test consists of a square grid, with one side at a constant velocity of 1, and the other three stationary, with no-slip boundary conditions imposed. Here, the grid is chosen to have size 100×100 . The fluid obeys an ideal gas EOS with $\gamma = 1.4$, and a viscosity power law with $K = 10^{-2}$, for various n . We have $c_s = 1$. The fluid is initially at rest, with $\rho = 1$, $p = 1$, $A = I$.

Figure 2.15 on page 72 and Figure 2.16 on page 72 show the results of running the system to steady state, for $n = 1.5$ and $n = 0.5$, respectively. The results are compared with those of Bell [11] and Neofytou [56]. As can be seen, there is good agreement between their results and those of the split solver; especially so for the case $n = 1.5$.

2.3.2.4 Elastoplastic Piston

This test is taken from [60], with exact solutions found in [49]. In this test, a piston with speed $20ms^{-1}$ is driven into copper initially at rest. An elastic shock wave develops, followed by a plastic shock wave. The following parameters were used: $\rho_0 = 8930$, $c_s = 2244$, $\sigma_0 = 9 \times 10^7$, $\tau_0 = 1$. The shock Mie-Gruneisen EOS is used for the internal energy, with $p_0 = 0$, $c_0 = 3940$, $\Gamma_0 = 2$, $s = 1.48$. 400 grid cells were used, with a third order WENO method.

Figure 2.18 on page 73 and Figure 2.19 on page 75 demonstrate the results using the split solver for various values of n . These results are compared with the exact solution to the problem under ideal plasticity (to which the former results should converge as $n \rightarrow \infty$). The nature of the split solver enables larger values of n to be used than those found in [60]. The results here are correspondingly closer to the ideal plasticity solution that they approximate.

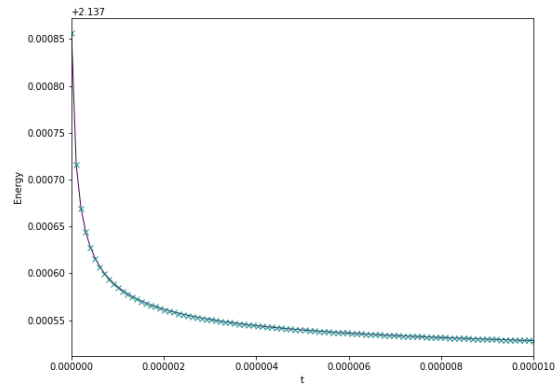


Figure 2.13: Total energy during the Strain Relaxation Test: approximate analytical solution (crosses) is compared with numerical ODE solution (solid line)

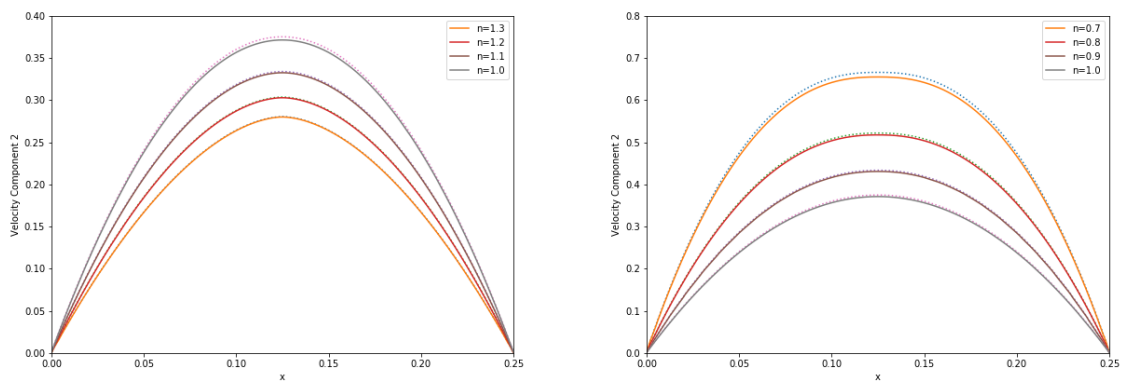


Figure 2.14: Velocity profiles for different dilatants (left) and pseudoplastics (right), in steady Poiseuille flow

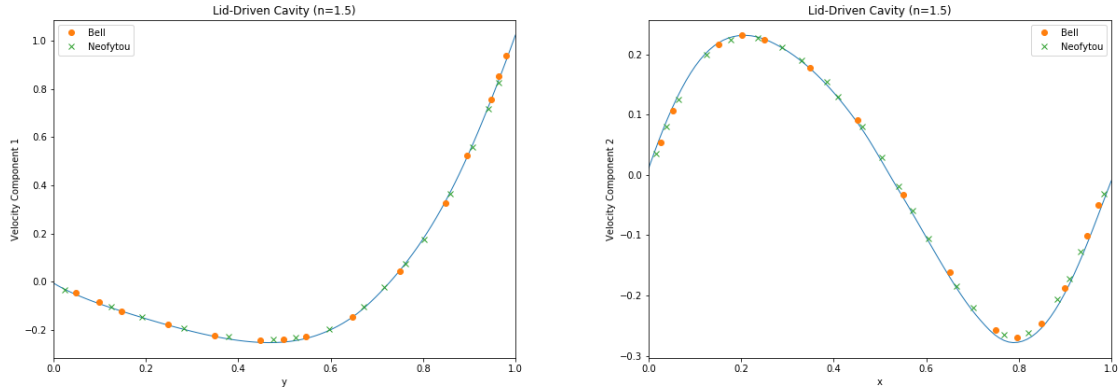


Figure 2.15: Velocity profiles for the Lid-Driven Cavity Test under the new formulation (solid line), for a dilatant with $n=1.5$. Slices are taken through the center of the domain, in both axes, and compared with those of [11] and [56].

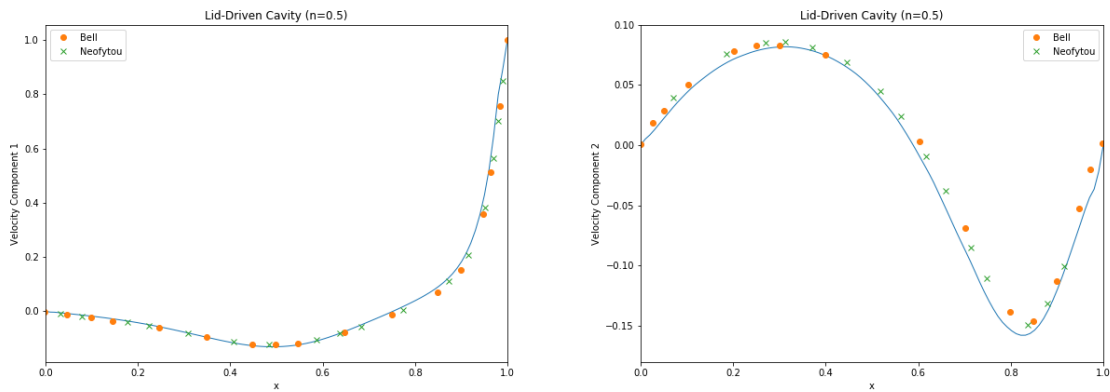


Figure 2.16: Velocity profiles for the Lid-Driven Cavity Test under the new formulation (solid line), for a pseudoplastic with $n=0.5$. Slices are taken through the center of the domain, in both axes, and compared with those of [11] and [56].

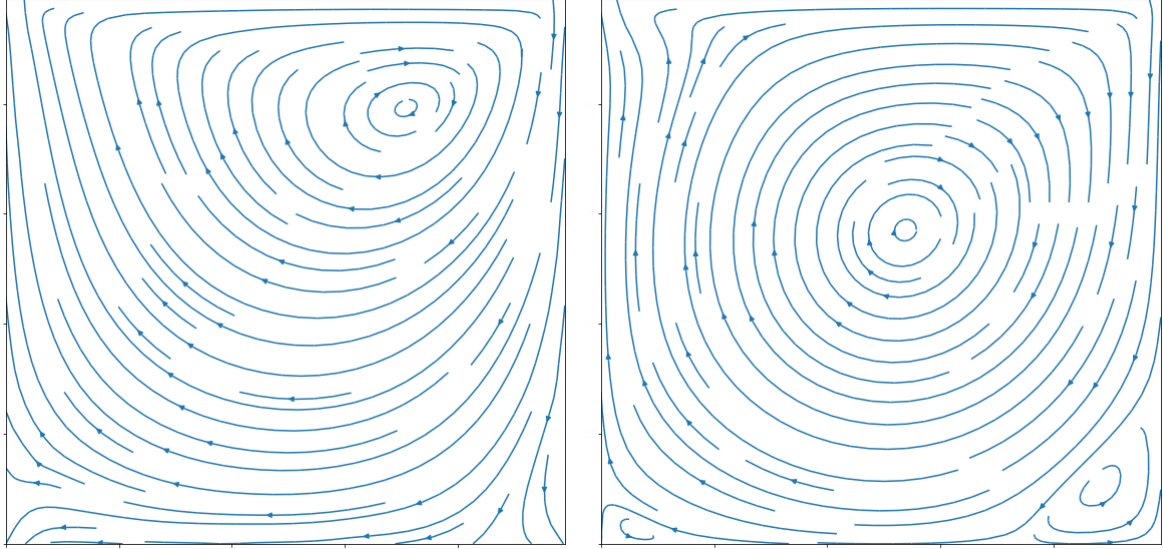


Figure 2.17: Streamplots for the Lid-Driven Cavity Test, for a pseudoplastic with $n=0.5$ (left) and a dilatant with $n=1.5$ (right)

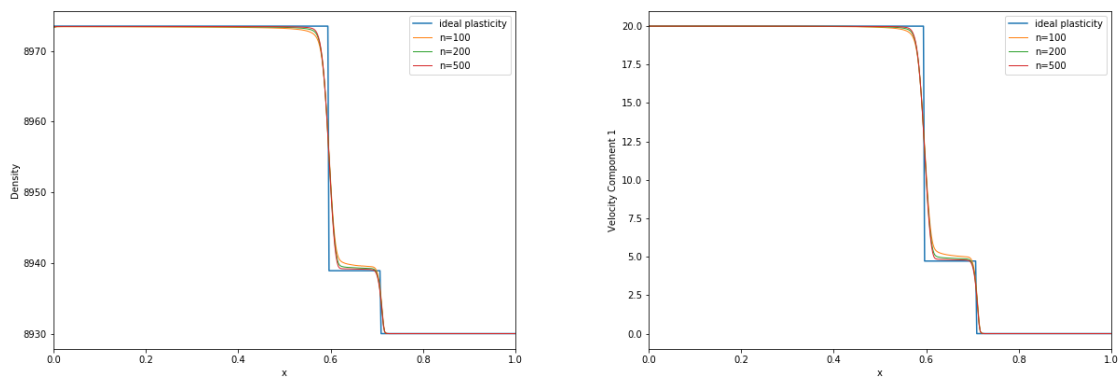


Figure 2.18: Density and velocity in the elastoplastic piston test, for various values of power-law parameter n

2.3.2.5 Cylindrical Shock

This test is taken from [8]. It consists of a slab of copper, occupying the domain $[0, 20]^2$, initially at rest. The region $r \leq 2$ is at ambient conditions, with zero pressure. The region $r > 2$ is at raised pressure 10^{10} and temperature 600.

The simulation is run to $t = 10^{-5}$ on a grid of shape 500×500 . A fourth order WENO scheme is used, with a CFL number of 0.8. The resulting radial density, velocity, stress tensor, and temperature profiles are given in Figure 2.20 on page 75, Figure 2.21 on page 76, Figure 2.22 on page 76, Figure 2.23 on page 77, and 2D heatmaps for density and speed are given in Figure 2.24 on page 77.

The results are compared with those of the 1D radially-symmetric scheme found in [8], which are in turn compared with the 2D results from the same publication. As can be seen, the 2D results computed using the new split solver for the GPR model more closely match the 1D radially-symmetric results than the 2D results from the aforementioned publication, with the spikes in both variables around $r = 2$ and the wave around $r = 6$ being more accurately resolved.

2.4 Conclusions

In summary, a new numerical method based on an operator splitting, and including some analytical results, has been proposed for the GPR model of continuum mechanics. It has been demonstrated that this method is able to match current ADER-WENO methods in terms of accuracy on a range of test cases. It is significantly faster than the other currently available methods, and it is easier to implement. The author would recommend that if very high order-of-accuracy is required, and computational cost is not important, then ADER-WENO methods may present a better option, as by design the new method cannot achieve better than second-order accuracy. This new method clearly has applications in which it will prove useful, however.

In a similar manner to the operator splitting method presented in [45], the Split-WENO method is second-order accurate and stable even for very stiff problems (in particular, the reader is referred to the results of the $\mu = 10^{-4}$ variation of Stokes' First Problem in 2.3.1.2 and the convergence study in 2.3.1.7). However, it will inevitably suffer from the incorrect

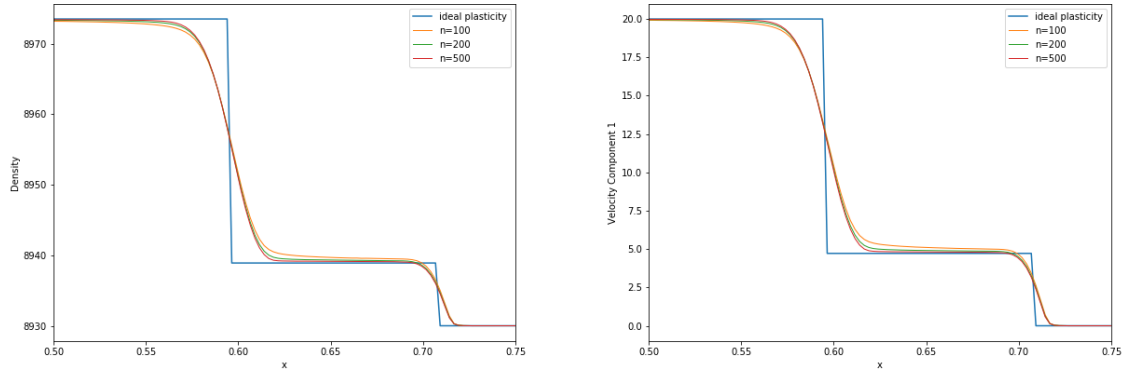


Figure 2.19: Zoom view of density and velocity in the elastoplastic piston test, for various values of power-law parameter n

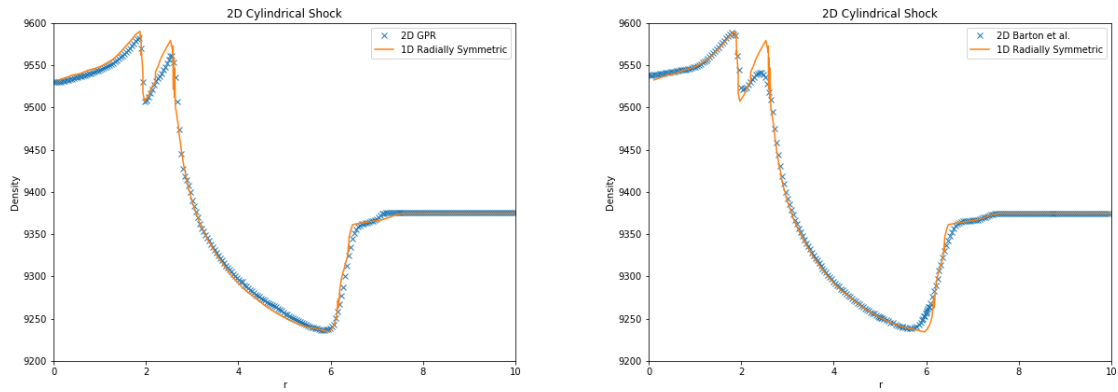


Figure 2.20: 1D density profiles for the 2D Cylindrical Shock Test, comparing the GPR model w/ split solver (left) with the results from [8] (right)

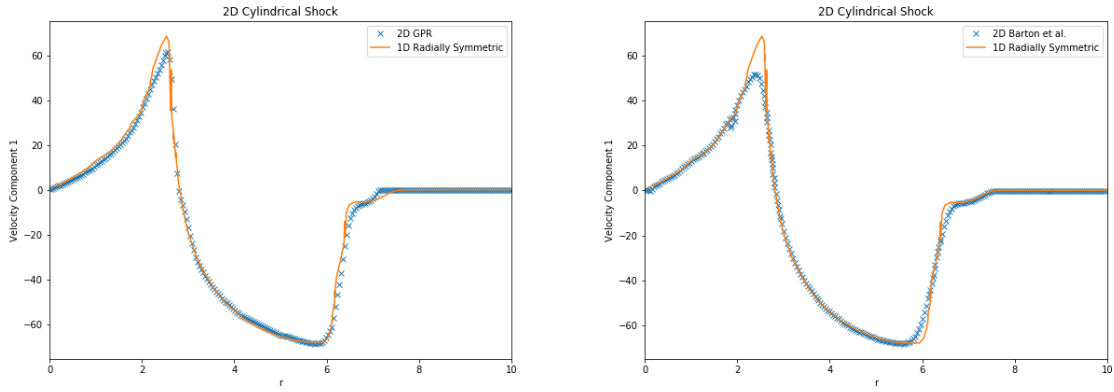


Figure 2.21: 1D velocity profiles for the 2D Cylindrical Shock Test, comparing the GPR model w/ split solver (left) with the results from [8] (right)

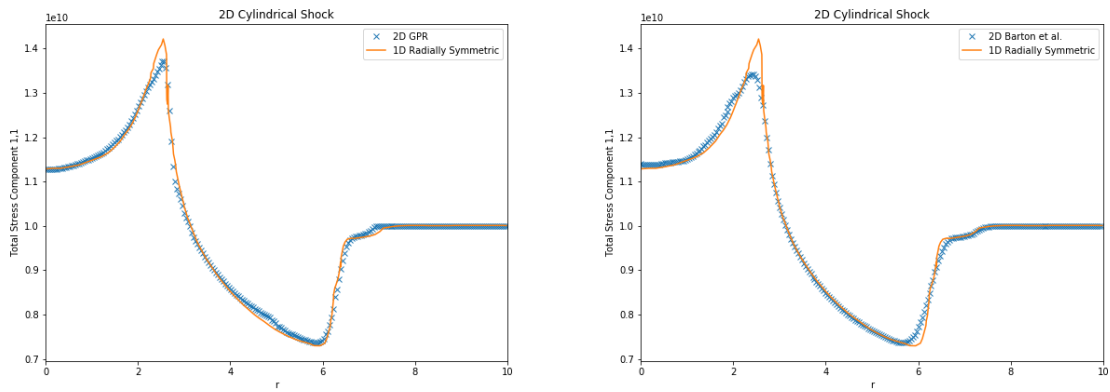


Figure 2.22: 1D stress tensor profiles for the 2D Cylindrical Shock Test, comparing the GPR model w/ split solver (left) with the results from [8] (right)

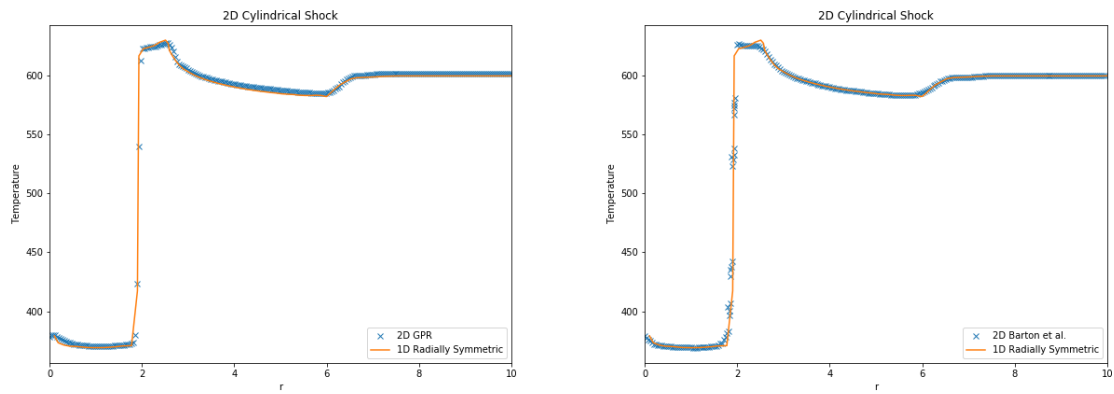


Figure 2.23: 1D temperature profiles for the 2D Cylindrical Shock Test, comparing the GPR model w/ split solver (left) with the results from [8] (right)

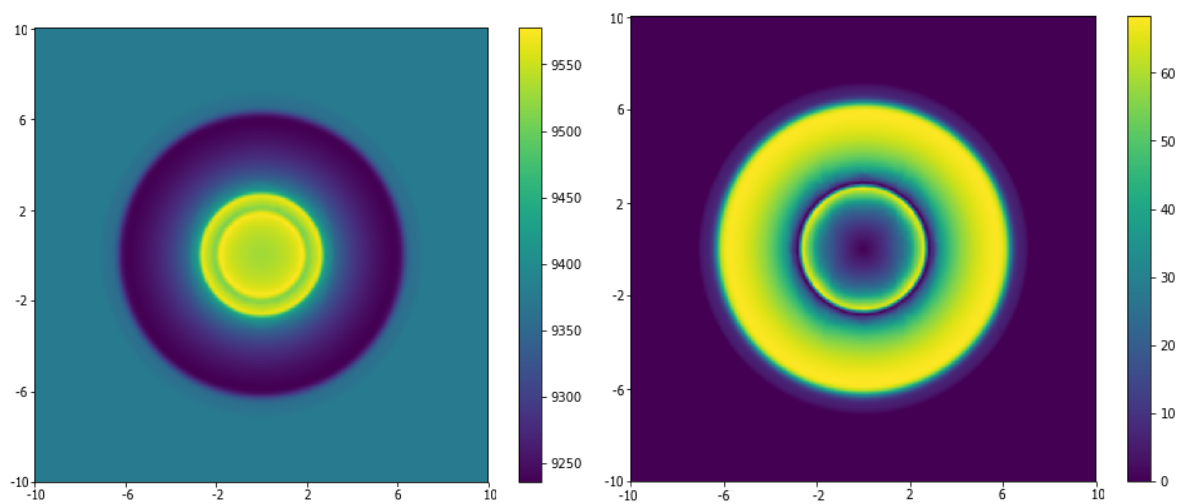


Figure 2.24: 2D plots of density and speed for the Cylindrical Shock Test

speed of propagation of discontinuities on regular, structured grids. This is due to a lack of spatial resolution in evaluating the source terms, as detailed in [45]. This issue can be rectified by the use of some form of shock tracking or mesh refinement, as noted in the cited paper. It is noted in [22] that operator splitting-based methods can result in schemes that are neither well-balanced nor asymptotically consistent. The extent to which these two conditions are violated by the Split-WENO method - and the severity in practice of any potential violation - is a topic of further research.

It should be noted that the assumption (2.85) used to derive the approximate analytical solver may break down for situations where the flow is compressed heavily in one direction but not the others. The reason for this is that one of the singular values of the distortion tensor will be much larger than the others, and the mean of the squares of the singular values will not be close to its geometric mean, meaning that the subsequent linearization of the ODE governing the mean of the singular values fails. It should be noted that none of the situations covered in this study presented problems for the approximate analytical solver, and situations which may be problematic are in some sense unusual. In any case, a stiff ODE solver can be used to solve the system (2.67) if necessary, utilizing the Jacobians derived in the appendix, and so the Split-WENO method is still very much usable in these situations, albeit slightly slower.

It should be noted that both the ADER-WENO and Split-WENO methods, as described in this study, are trivially parallelizable on a cell-wise basis. Thus, given a large number of computational cores, deficiencies in the Split-WENO method in terms of its order of accuracy may be overcome by utilizing a larger number of computational cells and cores. The computational cost of each time step is significantly smaller than with the ADER-WENO method, and the number of grid cells that can be used scales roughly linearly with number of cores, at constant time per iteration.

Chapter 3

Objective 3: Simulating Material Interfaces

3.1 Ghost Fluid Methods

3.1.1 Level Set Methods

Given a function $\phi : \mathbb{R}^n \rightarrow \mathbb{R}$, the level set of ϕ at level c is defined as:

$$\Gamma_c = \{\mathbf{x} : \phi(\mathbf{x}) = c\} \quad (3.1)$$

In this study, problems involving m different materials were assigned the functions $\phi_1, \dots, \phi_{m-1} : \mathbb{R}^n \rightarrow \mathbb{R}$, such that the region occupied by material i is considered to be exactly that in which $\phi_1, \dots, \phi_{i-1} > 0$, $\phi_i, \dots, \phi_{m-1} < 0$. The locations of the zero level sets correspond to the locations of the interfaces.

Given the local velocity field $\mathbf{v} : \mathbb{R}^n \rightarrow \mathbb{R}^3$, the functions ϕ are advected according to the level set equation [59]:

$$\frac{\partial \phi}{\partial t} = \mathbf{v} \cdot \nabla \phi \quad (3.2)$$

$\phi_1, \dots, \phi_{m-1}$ are renormalized to resemble a straight line at every time step, to avoid unwanted distortions such as becoming a multivalued function.

3.1.2 The Original Ghost Fluid Method

The Original Ghost Fluid Method of Fedkiw et al. [29] (an adaptation of the work of Glimm et al. [33]) is a numerical method for the Euler equations for simulating interfaces between multiple materials. The primitive variables for the Euler equations in 1D are given by $\mathbf{P} = \left(\rho \ v \ p \right)^T$.

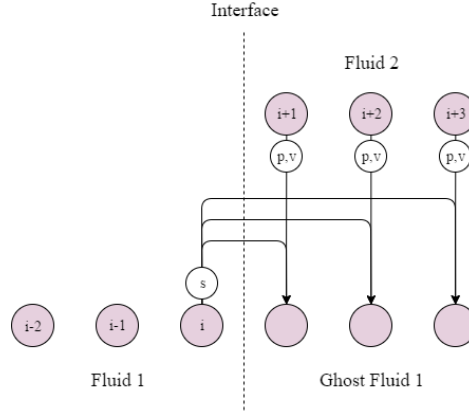


Figure 3.1: The Original Ghost Fluid Method

Suppose the interface between two fluids is modeled on spatial domain $[0, 1]$, divided into N cells with width $\Delta x = \frac{1}{N}$. Let the time step be Δt and let \mathbf{P}_i^n be the set of primitive variables in cell i at time $t_n = n\Delta t$. Let the level set function f have root x_n where $x_n \in \left[\left(i + \frac{1}{2}\right)\Delta x, \left(i + \frac{3}{2}\right)\Delta x\right]$. Thus, at time t_n the interface lies between the cells with primitive variables $\mathbf{P}_i^n, \mathbf{P}_{i+1}^n$. Define two sets of primitive variables:

$$\mathbf{P}_j^{(1)} = \begin{cases} \mathbf{P}_j^n & j \leq i \\ \left(\rho(s_i^n, p_j^n, \gamma_i^n) \ v_j^n \ p_j^n \right) & j > i \end{cases} \quad (3.3)$$

$$\mathbf{P}_j^{(2)} = \begin{cases} \mathbf{P}_j^n & j \geq i+1 \\ \left(\rho(s_{i+1}^n, p_j^n, \gamma_{i+1}^n) \ v_j^n \ p_j^n \right) & j < i+1 \end{cases} \quad (3.4)$$

where:

$$\rho(s, p, \gamma) = \left(\frac{p}{s}\right)^{\frac{1}{\gamma}} \quad (3.5)$$

All cells in $\mathbf{P}^{(1)}$ to the left of the interface have the same state variables as those of \mathbf{P}^n . All cells to the right have the same pressure and velocity as their counterparts in \mathbf{P}^n , but the same entropy as \mathbf{P}_i^n . This affects their density. The situation is analogous for $\mathbf{P}^{(2)}$. This is demonstrated in Figure 3.1 on page 80.

$\mathbf{P}^{(1)}, \mathbf{P}^{(2)}$ are stepped forward by time step Δt using a standard Eulerian method. f is advected using (3.2), taking the velocity in each cell to be that of \mathbf{P}^n . Now let $f(x_{n+1}) = 0$

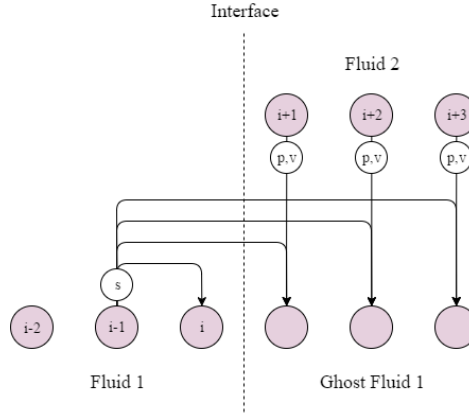


Figure 3.2: The Original Ghost Fluid Method, with the isobaric fix

where $x_{n+1} \in \left[\left(k + \frac{1}{2}\right) \Delta x, \left(k + \frac{3}{2}\right) \Delta x \right]$ for some k . Define:

$$P_j^{n+1} = \begin{cases} P_j^{(1)} & j \leq k \\ P_j^{(2)} & j > k \end{cases} \quad (3.6)$$

The rationale behind the original GFM is that in most applications, pressure and velocity are continuous across the interface, and thus the ghost cells may take the real pressure and velocity values. Entropy is generally discontinuous at a contact discontinuity, resulting in large truncation errors if a standard finite difference scheme is used to solve the system. Thus, entropy is extrapolated as a constant from the interface boundary cell into the ghost region.

Fedkiw et al. advised to use the *isobaric fix* technique. This involves setting the entropy of cell i , and all cells in the right ghost region, to that of cell $i - 1$, and setting the entropy of cell $i + 1$, and all cells in the left ghost region, to that of cell $i + 2$. This is demonstrated in Figure 3.2 on page 81.

Effectively, the ghost regions behave like they are composed of the same fluid as the regions they extend (as they have the same entropy), facilitating calculation of the next time step, but they have the same pressure and velocity profiles as the real fluids they replace, meaning the boundary conditions at the interface are upheld.

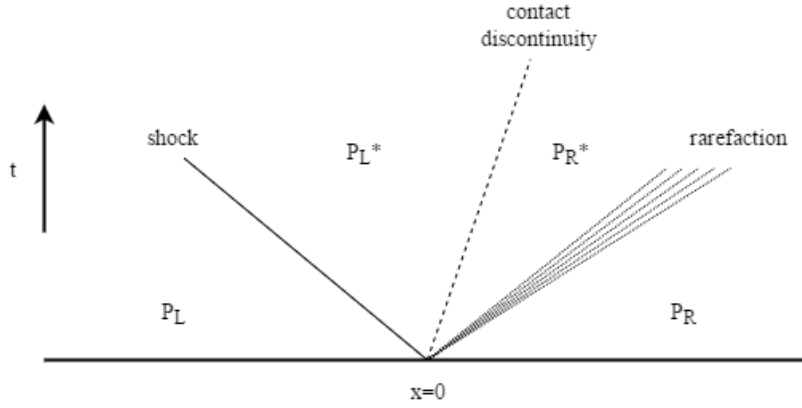


Figure 3.3: The qualitative structure of the solution to the Riemann Problem, showing the different possible types of waves

3.1.3 The Riemann Ghost Fluid Method

The Riemann Problem in its general form is the solution of the following initial value problem. Given a set of variables \mathbf{P} dependent on space and time, and a hyperbolic set of equations which govern their spatio-temporal evolution, $\mathbf{P}(x, t)$ is sought for $t > 0$, given the initial condition:

$$\mathbf{P}(x, 0) = \begin{cases} \mathbf{P}_L & x < 0 \\ \mathbf{P}_R & x > 0 \end{cases} \quad (3.7)$$

This problem is denoted by $RP(\mathbf{P}_L, \mathbf{P}_R)$. Exact solvers exist for the Riemann Problem for various sets of governing equations, such as the Euler equations [69], the equations of non-linear elasticity [7], or the shallow water equations [1], among others. There also exist approximate solvers for general conservative [47, 53] or non-conservative [19] hyperbolic systems of PDEs. The references given here form a very small sample of the work that has been done in this area.

The solution of the Riemann Problem usually takes the form of a set of waves, between which \mathbf{P} is constant. The waves can either be a contact discontinuity (across which pressure and velocity are continuous), a shock (across which all variables may be discontinuous), or a rarefaction (along which the variables vary continuously between their values on either side of the wave). The number and form of the waves are determined by the governing equations and the initial conditions. The states of the variables either side of the contact discontinuity

3.2 A Riemann Ghost Fluid Method for the GPR Model

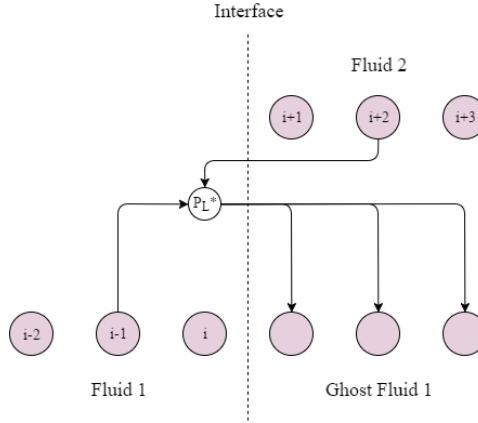


Figure 3.4: The Riemann Ghost Fluid Method

in the middle are known as the *star states*. This qualitative description is depicted in Figure 3.3 on page 82.

Liu et al. [46] demonstrated that the original GFM fails to resolve strong shocks at material interfaces. This is because the method effectively solves two separate single-fluid Riemann problems. The waves present in these Riemann problems do not necessarily correspond to those in the real Riemann problem across the interface. The Riemann Ghost Fluid Method of Sambasivan et al. [65, 66] aims to rectify this.

Given \mathbf{P}^n and $x_n \in \left[\left(i + \frac{1}{2}\right) \Delta x, \left(i + \frac{3}{2}\right) \Delta x\right]$, the ghost cells for fluid 1 are populated with the left star state of $RP(\mathbf{P}_{i-1}^n, \mathbf{P}_{i+2}^n)$, and the ghost cells for fluid 2 are populated with the right star state. $RP(\mathbf{P}_{i-1}^n, \mathbf{P}_{i+2}^n)$ is solved rather than $RP(\mathbf{P}_i^n, \mathbf{P}_{i+1}^n)$, as $\mathbf{P}_i^n, \mathbf{P}_{i+1}^n$ often contain errors generated by the fact that they lie on the material interface. \mathbf{P}^{n+1} is then generated as before from the newly formed $\mathbf{P}^{(1)}, \mathbf{P}^{(2)}$. This process is demonstrated in Figure 3.4 on page 83.

3.2 A Riemann Ghost Fluid Method for the GPR Model

3.2.1 Solving the Riemann Problem

Barton et al. have presented an RGFM for the equations of non-linear elasticity [6, 9]. Owing to the similarity of the structure of the non-linear elasticity equations to those of the GPR model (differing only in the presence of source terms, the form of the shear stress tensor,

3.2 A Riemann Ghost Fluid Method for the GPR Model

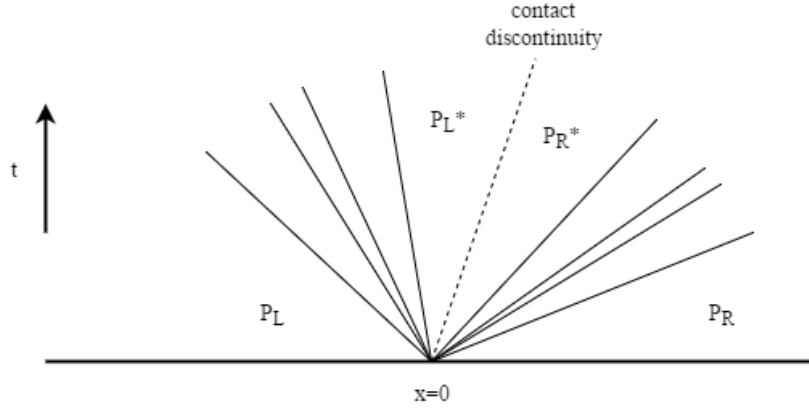


Figure 3.5: The Riemann Problem for the GPR model, assuming all waves are distinct

and possibly the EOS), their method is built upon here. The resulting method is named the *GPR-RGFM*.

The Riemann Problem of the GPR model takes the form demonstrated in Figure 3.5 on page 84. Assuming all waves are distinct, there are four waves on either side of the contact discontinuity. On each side, one wave corresponds to the thermal impulse (manifesting as a heat wave) and the other three correspond to the distortion components in the axis in which the Riemann Problem is considered (manifesting as two shear waves and one longitudinal pressure wave). It is important to note that - owing to the source terms - the star states are not constant in the spacetime region in which they reside, so the method presented here produces only an approximation to them.

The method is presented here along the first spatial axis. It can easily be adapted along any axis by taking the components of all relevant vector quantities (velocity, distortion, and thermal impulse) in the direction normal to the interface.

Denote the vector of primitive variables by \mathbf{P} . Take the set of left eigenvectors L (B.25) with eigenvalues $\{\lambda_i\}$. We have the standard set of relations along characteristics (curves along which $\frac{dx}{dt} = \lambda_i$):¹

$$L \cdot d\mathbf{P} = dt \cdot L \cdot \mathbf{S} \quad (3.8)$$

In what follows, we enact an operator splitting of the two processes present in the system

¹Take the hyperbolic system $\frac{\partial \mathbf{P}}{\partial t} + M \frac{\partial \mathbf{P}}{\partial x} = \mathbf{S}$. Let $\mathbf{l}_i^T M = \lambda_i \mathbf{l}_i^T$. Along characteristics corresponding to λ_i :

3.2 A Riemann Ghost Fluid Method for the GPR Model

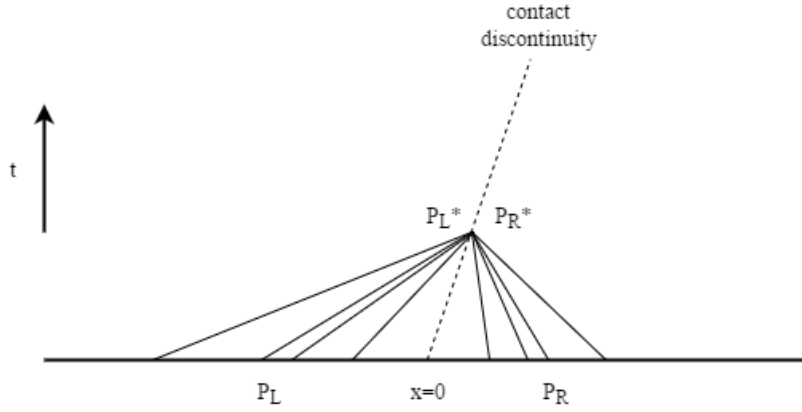


Figure 3.6: Different sets of characteristic curves, traveling from their respective initial points to the star region

(3.8):

$$L \cdot d\mathbf{P} = 0 \quad (3.9a)$$

$$\frac{d\mathbf{P}}{dt} = \mathbf{S} \quad (3.9b)$$

\mathbf{P}^{*K} is now sought, where $K = L$ or $K = R$, denoting the left or right sides of the interface, respectively. Take the following linearization:

$$d\mathbf{P}^K \approx \mathbf{P}^{*K} - \mathbf{P}^K \quad (3.10)$$

13 relations from (3.9a) are taken: four regarding the 4 sets of characteristics traveling into the contact discontinuity from side K (with speeds greater or less than v for $K = L$ or $K = R$, respectively), and nine relating to the contact discontinuity itself. This is demonstrated in Figure 3.6 on page 85. Four more relations must be derived to solve the

$$\begin{aligned} l_i^T \left(\frac{\partial \mathbf{P}}{\partial t} + M \frac{\partial \mathbf{P}}{\partial x} \right) &= l_i^T \left(\frac{\partial \mathbf{P}}{\partial t} + \frac{dx}{dt} \frac{\partial \mathbf{P}}{\partial x} \right) \\ &= l_i^T \frac{d\mathbf{P}}{dt} = l_i^T \mathbf{S} \end{aligned}$$

3.2 A Riemann Ghost Fluid Method for the GPR Model

system for \mathbf{P}^{*K} . Expanding the Taylor series of Σ^*, T^* :

$$\Sigma^* = \Sigma + (\rho^* - \rho) \frac{\partial \Sigma}{\partial \rho} + (p^* - p) \frac{\partial \Sigma}{\partial p} + (A_{mn}^* - A_{mn}) \frac{\partial \Sigma}{\partial A_{mn}} + O(d\mathbf{P}^2) \quad (3.11a)$$

$$T^* = T + (\rho^* - \rho) \frac{\partial T}{\partial \rho} + (p^* - p) \frac{\partial T}{\partial p} + O(d\mathbf{P}^2) \quad (3.11b)$$

Thus, we have:

$$\Sigma^* - \Sigma \approx (p^* - p) I - (\rho^* - \rho) \frac{\partial \sigma}{\partial \rho} - (A_{mn}^* - A_{mn}) \frac{\partial \sigma}{\partial A_{mn}} \quad (3.12a)$$

$$T^* - T \approx (\rho^* - \rho) \frac{\partial T}{\partial \rho} + (p^* - p) \frac{\partial T}{\partial p} \quad (3.12b)$$

These are the extra required relations. Thus we have:

$$\hat{L}^K \cdot (\mathbf{P}^{*K} - \mathbf{P}^K) = \mathbf{c}^K \quad (3.13)$$

where \hat{L}^K takes the form found in (3.28), with $\xi = -1$ for $K = R$ and $\xi = 1$ for $K = L$, and:

$$\mathbf{c}^K = \begin{pmatrix} \Sigma_1^{*K} - \Sigma_1^K \\ T^{*K} - T^K \\ \mathbf{0} \end{pmatrix} \quad (3.14)$$

The inverse of \hat{L}^K takes the form found in (3.29).

\hat{L}^K, \hat{L}^{K-1} are evaluated at \mathbf{P}^K . It remains to find expressions for Σ^* and T^* in terms of $\mathbf{P}^L, \mathbf{P}^R$ to close the system. The obtained values depend on the boundary conditions chosen, as explained below.

3.2 A Riemann Ghost Fluid Method for the GPR Model

3.2.1.1 Stick Boundary Conditions

The following boundary conditions are used:

$$\Sigma_1^{*L} = \Sigma_1^{*R} \quad (3.15a)$$

$$T^{*L} = T^{*R} \quad (3.15b)$$

$$\mathbf{v}^{*L} = \mathbf{v}^{*R} \quad (3.15c)$$

$$q_1^{*L} = q_1^{*R} \quad (3.15d)$$

Taking the relevant rows of $\mathbf{P}^{*K} = \mathbf{P}^K + \hat{L}^{K-1} \mathbf{c}^K$:

$$\begin{pmatrix} \mathbf{v}^* \\ J_1^* \end{pmatrix} = \begin{pmatrix} \mathbf{v}^K \\ J_1^K \end{pmatrix} + Y^K \left(\begin{pmatrix} \Sigma_1^* \\ T^* \end{pmatrix} - \begin{pmatrix} \Sigma_1^K \\ T^K \end{pmatrix} \right) \quad (3.16)$$

Thus:

$$\begin{pmatrix} \Sigma_1^* \\ T^* \end{pmatrix} = (Y^L - Y^R)^{-1} \left(\begin{pmatrix} \mathbf{v}^R \\ J_1^R \end{pmatrix} - \begin{pmatrix} \mathbf{v}^L \\ J_1^L \end{pmatrix} + Y^L \begin{pmatrix} \Sigma_1^L \\ T^L \end{pmatrix} - Y^R \begin{pmatrix} \Sigma_1^R \\ T^R \end{pmatrix} \right) \quad (3.17)$$

3.2.1.2 Slip Boundary Conditions

The following boundary conditions are used:

$$\Sigma_{11}^{*L} = \Sigma_{11}^{*R} \quad (3.18a)$$

$$\Sigma_{12}^{*L}, \Sigma_{12}^{*R} = 0 \quad (3.18b)$$

$$\Sigma_{13}^{*L}, \Sigma_{13}^{*R} = 0 \quad (3.18c)$$

$$T^{*L} = T^{*R} \quad (3.18d)$$

$$v_1^{*L} = v_1^{*R} \quad (3.18e)$$

$$q_1^{*L} = q_1^{*R} \quad (3.18f)$$

3.2 A Riemann Ghost Fluid Method for the GPR Model

Taking the relevant rows of $\mathbf{P}^{*K} = \mathbf{P}^K + \hat{L}^{K-1} \mathbf{c}^K$:

$$\begin{pmatrix} v_1^* \\ J_1^* \end{pmatrix} = \begin{pmatrix} v_1^K \\ J_1^K \end{pmatrix} + \tilde{Y}^K \left(\begin{pmatrix} \Sigma_{11}^* \\ 0 \\ 0 \\ T^* \end{pmatrix} - \begin{pmatrix} \Sigma_{11}^K \\ \Sigma_{12}^K \\ \Sigma_{13}^K \\ T^K \end{pmatrix} \right) \quad (3.19)$$

where

$$\tilde{Y}^K = \begin{pmatrix} \mathbf{Y}_1^K \\ \mathbf{Y}_4^K \end{pmatrix} \quad (3.20)$$

Thus:

$$\begin{pmatrix} \Sigma_{11}^* \\ T^* \end{pmatrix} = (\hat{Y}^L - \hat{Y}^R)^{-1} \left(\begin{pmatrix} v_1^R \\ J_1^R \end{pmatrix} - \begin{pmatrix} v_1^K \\ J_1^K \end{pmatrix} + Y^L \begin{pmatrix} \Sigma_1^L \\ T^L \end{pmatrix} - Y^R \begin{pmatrix} \Sigma_1^R \\ T^R \end{pmatrix} \right) \quad (3.21)$$

where

$$\hat{Y}^K = \begin{pmatrix} Y_{11}^K & Y_{14}^K \\ Y_{41}^K & Y_{44}^K \end{pmatrix} \quad (3.22)$$

3.2.1.3 Vacuum Boundary Conditions

The following boundary conditions are used:

$$\Sigma_1^* = 0 \quad (3.23a)$$

$$q_1^* = 0 \quad (3.23b)$$

Taking the relevant row of $\mathbf{P}^{*K} = \mathbf{P}^K + \hat{L}^{K-1} \mathbf{c}^K$:

$$J_1^* = J_1^K + \mathbf{Y}_4^K \cdot \left(\begin{pmatrix} 0 \\ T^* \end{pmatrix} - \begin{pmatrix} \Sigma_1^K \\ T^K \end{pmatrix} \right) \quad (3.24)$$

3.2 A Riemann Ghost Fluid Method for the GPR Model

As $q_1^* = 0$ implies that $J_1^* = 0$, we have:

$$T^* = \frac{1}{Y_{44}^K} \left(\mathbf{Y}_4^K \cdot \begin{pmatrix} \Sigma_1^K \\ T^K \end{pmatrix} - J_1^K \right) = T^K + \frac{\mathbf{Y}_{4,:3}^K \cdot \Sigma_1^K - J_1^K}{Y_{44}^K} \quad (3.25)$$

3.2.1.4 Iteration

(3.13) is solved for \mathbf{P}^{*K} , which is taken to be the star state if the following conditions are satisfied:

$$\frac{|\Sigma_1^{*L} - \Sigma_1^{*R}|}{\min(\rho_0^L, \rho_0^R) \times \min(c_s^L, c_s^R)^2} < TOL \quad (3.26a)$$

$$\frac{|v_1^L - v_1^R|}{\min(c_s^L, c_s^R)} < TOL \quad (3.26b)$$

$$\frac{|q_1^L - q_1^R|}{\min(\tilde{q}^L, \tilde{q}^R)} < TOL \quad (3.26c)$$

$$\frac{|T^L - T^R|}{\min(T_0^L, T_0^R)} < TOL \quad (3.26d)$$

where

$$\tilde{q} = \frac{c_t^2}{\rho_0} \sqrt{\frac{T_0^3}{c_V}} \quad (3.27)$$

These convergence criteria are chosen so that the variables required to be less than TOL are dimensionless. At every iteration, (3.9b) is solved using the ODE solvers described in 2.2.3.

3.2.2 Linear Conditions

Replacing the first four lines of (B.25) with the conditions

$$\hat{L}^K = \left\{ \begin{pmatrix} -\frac{\partial \sigma_d}{\partial \rho} \mathbf{e}_d & -\Pi_1 & -\Pi_2 & -\Pi_3 & 0_{3,6} \\ \frac{\partial T}{\partial \rho} & \frac{\partial T}{\partial p} & 0_{1,3} & 0_{1,3} & 0_{1,3} & 0_{1,6} \\ Q\Xi_1 & -\frac{1}{\rho} Q_{:,1:3} \Pi_2 & -\frac{1}{\rho} Q_{:,1:3} \Pi_3 & \xi DQ & 0_{4,2} \\ -\frac{1}{\rho} 0 & \mathbf{e}_d^T A^{-1} & \mathbf{e}_d^T A^{-1} \Pi_1^{-1} \Pi_2 & \mathbf{e}_d^T A^{-1} \Pi_1^{-1} \Pi_3 & 0_{1,6} \end{pmatrix} \right\} \quad (3.28)$$

$$\left(\begin{pmatrix} 0_{3,5} & I_3 & 0_{3,3} & 0_{3,6} \\ 0_{3,5} & 0_{3,3} & I_3 & 0_{3,6} \end{pmatrix} \right)$$

$$\left(0_{2,15} \ I_2 \right)$$

$$\hat{L}^{K-1} = \left\{ \begin{pmatrix} X \\ 0_{6,4} \\ Y \\ 0_{2,4} \end{pmatrix}, \begin{pmatrix} 0_{11,4} \\ \xi (DQ)^{-1} \\ 0_{2,4} \end{pmatrix}, \begin{pmatrix} -cT_p \\ cT_\rho \\ c\Pi_d^{-1} \mathbf{w} \\ 0_{12,1} \end{pmatrix}, \begin{pmatrix} 0_{2,3} & 0_{2,3} \\ -\Pi_1^{-1} \Pi_2 & -\Pi_1^{-1} \Pi_3 \\ I_3 & 0_{3,3} \\ 0_{3,3} & I_3 \\ 0_{6,3} & 0_{6,3} \end{pmatrix}, \begin{pmatrix} 0_{15,2} \\ I_2 \end{pmatrix} \right\} \quad (3.29)$$

where:

$$X = \begin{pmatrix} \vdots & \vdots & \ddots & \vdots & \ddots \\ -\frac{\partial \sigma_d}{\partial \rho} \mathbf{e}_d & \cdots & -\Pi_1 & \cdots \\ \vdots & \vdots & \ddots & \vdots & \ddots \\ \frac{\partial T}{\partial \rho} & \frac{\partial T}{\partial p} & 0 & 0 & 0 \\ -\frac{1}{\rho} & 0 & \cdots & \mathbf{e}_d^T A^{-1} & \cdots \end{pmatrix}^{-1} \begin{pmatrix} 1 & 0 & 0 & 0 \\ 0 & 1 & 0 & 0 \\ 0 & 0 & 1 & 0 \\ 0 & 0 & 0 & 1 \\ 0 & 0 & 0 & 0 \end{pmatrix} \quad (3.30a)$$

$$Y = -\xi Q^{-1} D^{-1} Q \Xi_1 X \quad (3.30b)$$

3.2 A Riemann Ghost Fluid Method for the GPR Model

By inversion of block matrices²:

$$\begin{pmatrix} \vdots & \vdots & \ddots & \vdots & \ddots \\ -\frac{\partial \sigma_d}{\partial \rho} \mathbf{e}_d & \cdots & -\Pi_1 & \cdots \\ \vdots & \vdots & \ddots & \vdots & \ddots \\ \frac{\partial T}{\partial \rho} & \frac{\partial T}{\partial p} & 0 & 0 & 0 \\ -\frac{1}{\rho} & 0 & \cdots & \mathbf{e}_d^T A^{-1} & \cdots \end{pmatrix}^{-1} = \begin{pmatrix} D^{-1} C Z^{-1} & D^{-1} (I - C Z^{-1} B D^{-1}) \\ -Z^{-1} & Z^{-1} B D^{-1} \end{pmatrix} \quad (3.31)$$

where

$$\begin{cases} B = \begin{pmatrix} \vdots & \vdots \\ -\frac{\partial \sigma_d}{\partial \rho} \mathbf{e}_d \\ \vdots & \vdots \end{pmatrix} & C = \begin{pmatrix} 0 & 0 & 0 \\ \cdots & \mathbf{e}_d^T A^{-1} & \cdots \end{pmatrix} \\ D = \begin{pmatrix} \frac{\partial T}{\partial \rho} & \frac{\partial T}{\partial p} \\ -\frac{1}{\rho} & 0 \end{pmatrix} & Z = \Pi_1 + \frac{\rho}{T_p} \left(T_p \frac{\partial \sigma_d}{\partial \rho} + T_p \mathbf{e}_d \right) \mathbf{e}_d^T A^{-1} \end{cases} \quad (3.32)$$

3.2.3 The Case without Heat Conduction

If the heat conduction terms are dropped from the GPR model, the eigenstructure of the system changes, along with the solution of the linear conditions. Ξ retains the same definition, but is now a 3×3 matrix (comprising the top-left corner of Ξ under heat conduction). Thus, Q, D are also 3×3 matrices. Taking the eigenvectors (B.38), the linear conditions become:

$$\hat{L}^K = \left\{ \begin{pmatrix} -\frac{\partial \sigma_d}{\partial \rho} \mathbf{e}_d - \Pi_1 - \Pi_2 - \Pi_3 \\ Q \Xi_1 - \frac{1}{\rho} Q \Pi_2 - \frac{1}{\rho} Q \Pi_3 \quad \xi D Q \\ (I - B A^{-1} C)^{-1} \begin{pmatrix} I_2 - B A^{-1} & -B A^{-1} \Pi_1^{-1} \Pi_2 & -B A^{-1} \Pi_1^{-1} \Pi_3 & 0_{2,3} \end{pmatrix} \\ \begin{pmatrix} 0_{3,5} & I_3 & 0_{3,3} & 0_{3,3} \\ 0_{3,5} & 0_{3,3} & I_3 & 0_{3,3} \end{pmatrix} \end{pmatrix} \right\} \quad (3.33)$$

² $\begin{pmatrix} A & B \\ C & D \end{pmatrix}^{-1} = \begin{pmatrix} (A - B D^{-1} C)^{-1} & -(A - B D^{-1} C)^{-1} B D^{-1} \\ -D^{-1} C (A - B D^{-1} C)^{-1} & D^{-1} (I + C (A - B D^{-1} C)^{-1} B D^{-1}) \end{pmatrix}$

3.2 A Riemann Ghost Fluid Method for the GPR Model

$$\hat{L}^{K-1} = \left\{ \begin{pmatrix} X \\ 0_{6,3} \\ Y \end{pmatrix}, \begin{pmatrix} 0_{11,3} \\ \xi (DQ)^{-1} \end{pmatrix}, \begin{pmatrix} 1 & 0 \\ 0 & 1 \\ -\Pi_1^{-1} \frac{\partial \sigma_1}{\partial \rho} & \Pi_1^{-1} \mathbf{e}_1 \\ \mathbf{0}_9 & \mathbf{0}_9 \end{pmatrix}, \begin{pmatrix} 0_{2,3} & 0_{2,3} \\ -\Pi_1^{-1} \Pi_2 & -\Pi_1^{-1} \Pi_3 \\ I_3 & 0_{3,3} \\ 0_{3,3} & I_3 \\ 0_{3,3} & 0_{3,3} \end{pmatrix} \right\} \quad (3.34)$$

where:

$$X = \begin{pmatrix} \vdots & \vdots & \ddots & \vdots & \ddots \\ -\frac{\partial \sigma_d}{\partial \rho} & \mathbf{e}_d & \cdots & -\Pi_1 & \cdots \\ \vdots & \vdots & \ddots & \vdots & \ddots \\ \vdots & \ddots & \ddots & \vdots & \ddots \\ (I - BA^{-1}C)^{-1} & \cdots & \cdots & -(I - BA^{-1}C)^{-1} BA^{-1} & \cdots \end{pmatrix}^{-1} \begin{pmatrix} 1 & 0 & 0 & 0 \\ 0 & 1 & 0 & 0 \\ 0 & 0 & 1 & 0 \\ 0 & 0 & 0 & 1 \\ 0 & 0 & 0 & 0 \end{pmatrix} \quad (3.35a)$$

$$Y = -\xi Q^{-1} D^{-1} Q \Xi_1 X \quad (3.35b)$$

By inversion of block matrices:

$$\begin{pmatrix} \vdots & \vdots & \ddots & \vdots & \ddots \\ -\frac{\partial \sigma_d}{\partial \rho} & \mathbf{e}_d & \cdots & -\Pi_1 & \cdots \\ \vdots & \vdots & \ddots & \vdots & \ddots \\ \vdots & \ddots & \ddots & \vdots & \ddots \\ (I - BA^{-1}C)^{-1} & \cdots & \cdots & -(I - BA^{-1}C)^{-1} BA^{-1} & \cdots \end{pmatrix}^{-1} \quad (3.36)$$

$$= \begin{pmatrix} -BA^{-1}Z & (I + BA^{-1}Z\tilde{B})(I - BA^{-1}\Pi_1^{-1}\tilde{B}) \\ -Z & Z\tilde{B}(I - BA^{-1}\Pi_1^{-1}\tilde{B}) \end{pmatrix}$$

where

$$Z = (\Pi_1 - \tilde{B}BA^{-1})^{-1} \quad (3.37a)$$

$$\tilde{B} = \begin{pmatrix} \cdots & -\frac{\partial \sigma_1}{\partial \rho} & \cdots \\ \cdots & \mathbf{e}_1 & \cdots \end{pmatrix}^T \quad (3.37b)$$

$$B = \begin{pmatrix} \rho & 0 & 0 \\ (\rho c_0^2 + \sigma_{11} - \rho \frac{\partial \sigma_{11}}{\partial \rho}) & (\sigma_{21} - \rho \frac{\partial \sigma_{21}}{\partial \rho}) & (\sigma_{31} - \rho \frac{\partial \sigma_{31}}{\partial \rho}) \end{pmatrix} \quad (3.37c)$$

3.3 Numerical Results

The GPR-RGFM is now assessed. The first two tests in this chapter are standard Riemann problems, exact solutions to which exist for the Euler equations. The viscosity of the GPR model smears the solutions in areas in which the solutions to the Euler equations are discontinuous or not smooth. This smearing is not the result of using a low-order solver (all results in these sections being calculated to third order). The last two tests assess the ability of the GPR-RGFM to correctly model heat conduction across interfaces.

3.3.1 Helium Bubble

The interface between two different gases is now modeled. As in Test B of Wang et al. [71], a bubble of helium - surrounded by air - initially occupies the region $x \in [0.4, 0.6]$. A shock front in the air, initially at $x = 0.05$, travels towards the helium bubble. The initial conditions are given in Table 3.1 on page 95. Realistic material parameters are taken for the helium: $\gamma = 1.66$, $c_v = 3127$, $\rho_0 = 0.163$, $\mu = 1.99 \times 10^{-5}$, $P_r = 0.688$, and for the air: $\gamma = 1.4$, $c_v = 721$, $\rho_0 = 1.18$, $\mu = 1.85 \times 10^{-5}$, $P_r = 0.714$. In both cases, $p_0 = 101325$, $c_s = 55$, and $c_t = 500$.

200 cells are used. The results for times $t = 7 \times 10^{-4}$ and $t = 14 \times 10^{-4}$ are displayed in Figure 3.7 on page 94, with reference solutions computed with 2000 cells. In the former, the shock is about to hit the helium bubble (corresponding to the region of low density). In the latter, the shock has traveled through the helium bubble, compressing it slightly, and the bubble itself has moved almost 0.1 spatial units to the right. There is good correspondence with the results in [71] and the sharp discontinuity in density is maintained.

3.3 Numerical Results

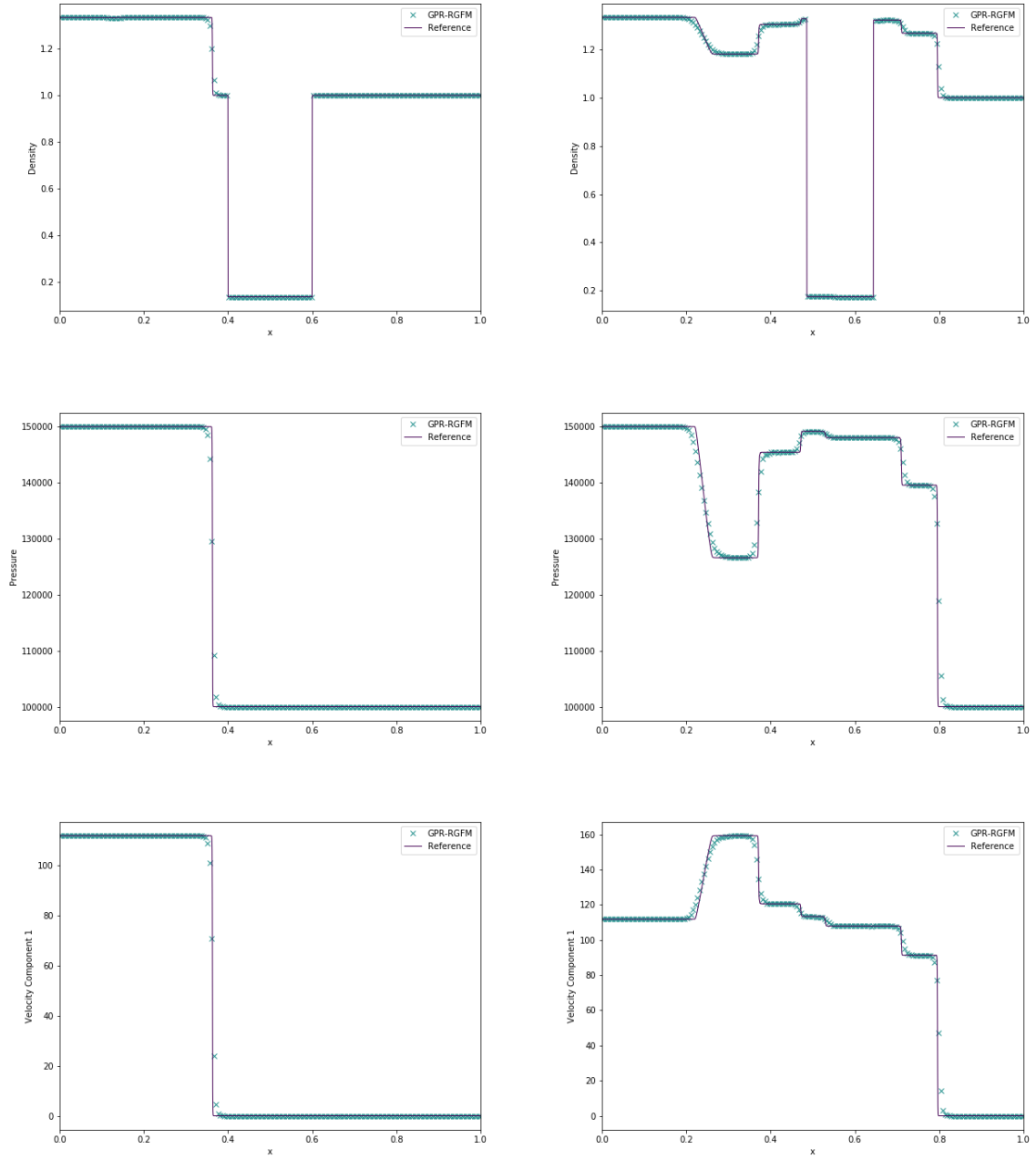


Figure 3.7: Density, pressure, and velocity for the helium bubble test with GPR-RGFM at times $t = 7 \times 10^{-4}$ (left) and $t = 14 \times 10^{-4}$ (right)

	ρ	p	\mathbf{v}	A	\mathbf{J}
$x < 0.05$	1.3333	1.5×10^5	$(35.35\sqrt{10} \ 0 \ 0)$	$\left(\frac{1.3333}{1.18}\right)^{\frac{1}{3}} I_3$	$\mathbf{0}$
$0.05 \leq x < 0.4$	1	10^5	$\mathbf{0}$	$\left(\frac{1}{1.18}\right)^{\frac{1}{3}} I_3$	$\mathbf{0}$
$0.4 \leq x < 0.6$	0.1379	10^5	$\mathbf{0}$	$\left(\frac{0.1379}{0.163}\right)^{\frac{1}{3}} I_3$	$\mathbf{0}$
$0.6 \leq x \leq 1$	1	10^5	$\mathbf{0}$	$\left(\frac{1}{1.18}\right)^{\frac{1}{3}} I_3$	$\mathbf{0}$

Table 3.1: Initial conditions for the helium bubble test

	ρ	p	\mathbf{v}	A	\mathbf{J}
$0 \leq x < 0.7$	1000	10^9	$\mathbf{0}$	I_3	$\mathbf{0}$
$0.7 \leq x \leq 1$	50	10^5	$\mathbf{0}$	$\sqrt[3]{50} \cdot I_3$	$\mathbf{0}$

Table 3.2: Initial conditions for the water-air shock tube test

3.3.2 Water-Air Shock Tube

This test comprises an interface between water and air, with initial data taken from Chinnayya et al. [REF]. Due to the large difference in state variables are qualitative characteristics of the two fluids, this is an example of a test with which the original GFM does not perform well. The results using the GPR-RGFM are shown, along with the exact solution to the Euler equations.

3.3.3 Copper-PBX Impact

This test is taken from [9].

3.3.4 Aluminium in Vacuum

This test is taken from [6].

3.3.5 Heat Conduction in a Gas

This test is based on the Heat Conduction in a Gas Test of Dumbser et al. [24]. Two ideal gases at different temperatures are initially in contact at position $x = 0$. The initial

3.3 Numerical Results

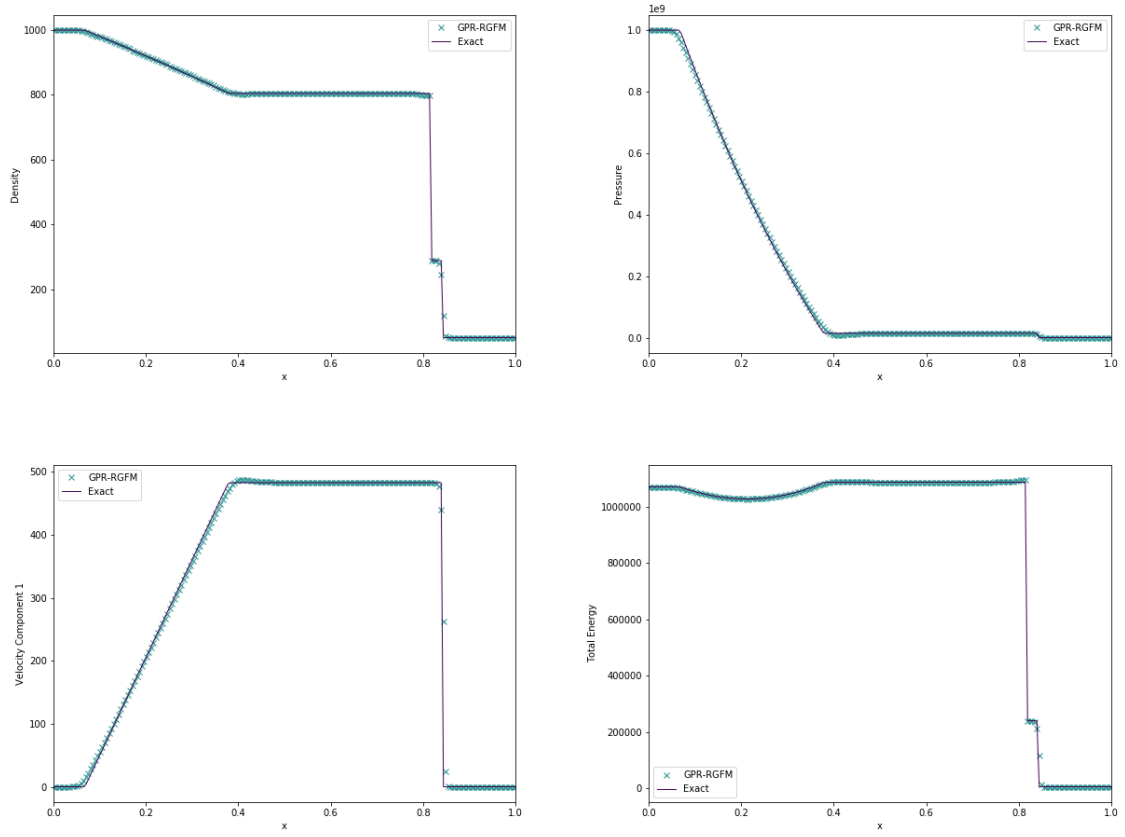


Figure 3.8: Density, pressure, velocity, and internal energy for the water-air shock tube test with GPR-RGFM

3.3 Numerical Results

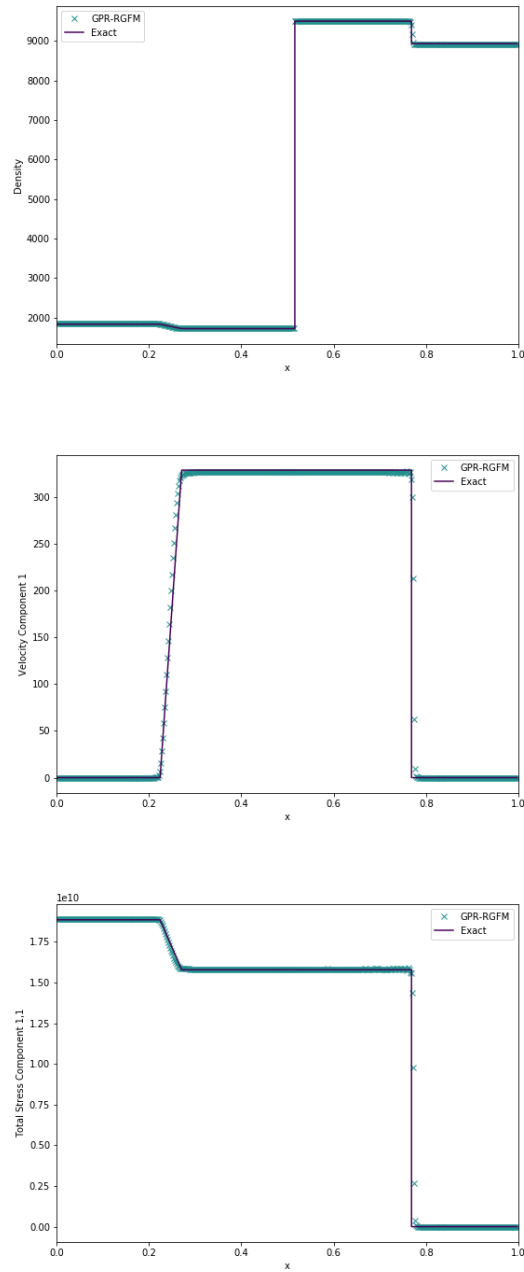


Figure 3.9: Density, velocity, and total stress for the Copper-PBX test with GPR-RGFM

3.3 Numerical Results

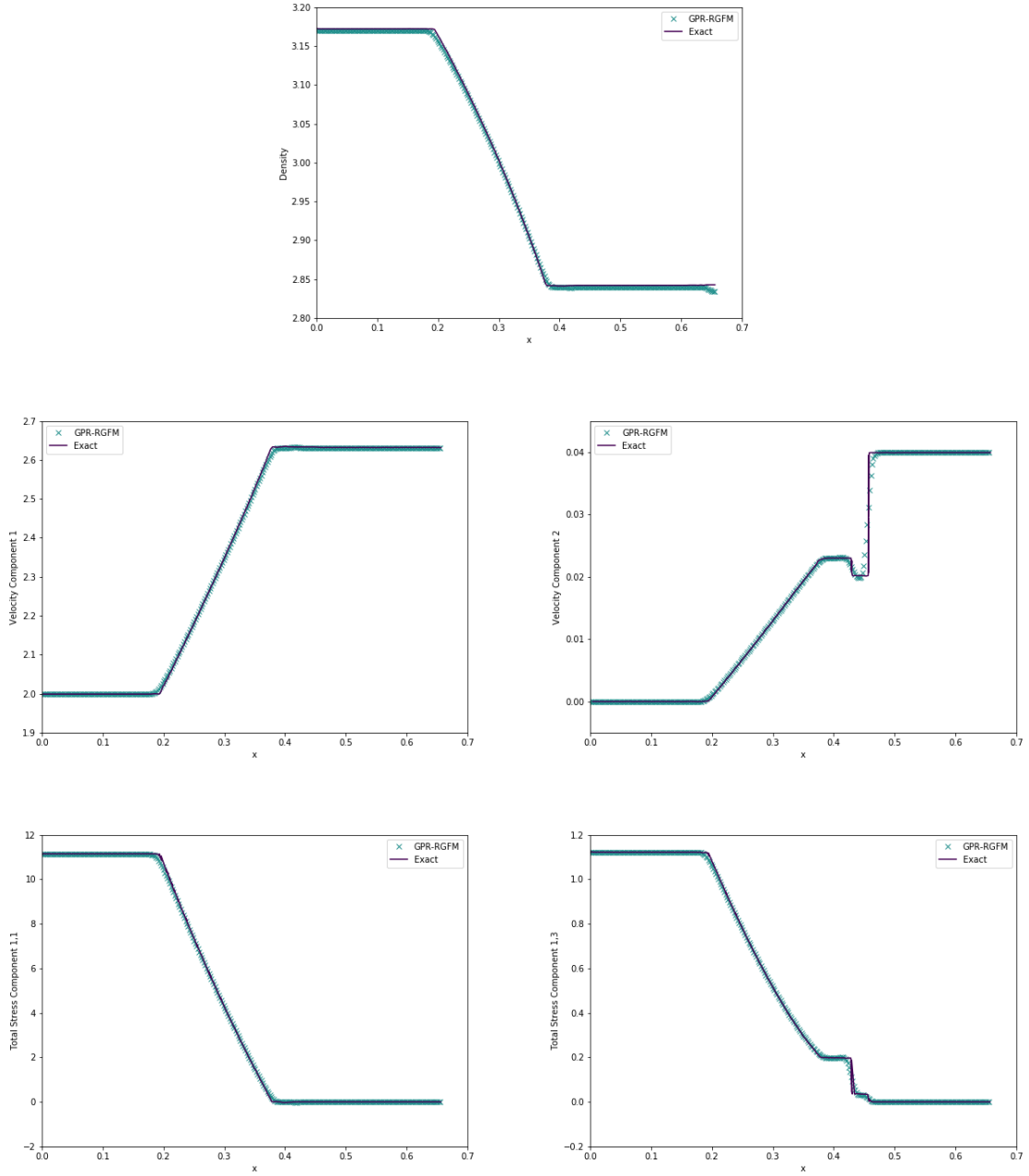


Figure 3.10: Density, velocity, and total stress for the aluminium-vacuum test with GPR-RGFM

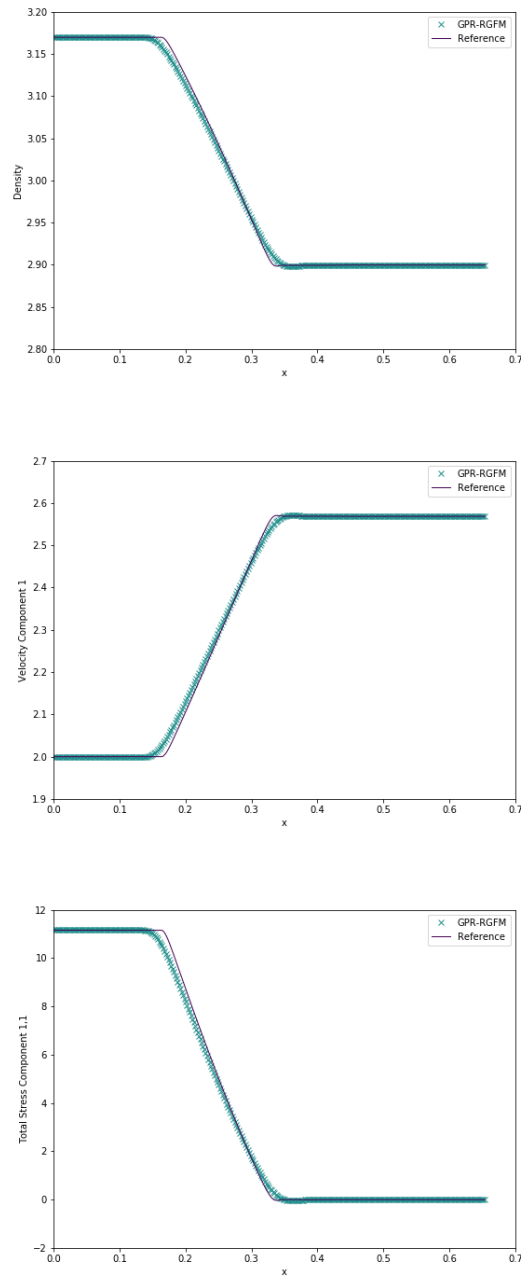


Figure 3.11: Density, velocity, and total stress for the aluminium-vacuum test with GPR-RGFM, including thermal conduction

	ρ	p	\mathbf{v}	A	\mathbf{J}
$x < 0$	2	1	$\mathbf{0}$	$\sqrt[3]{2} \cdot I_3$	$\mathbf{0}$
$x \geq 0$	0.5	1	$\mathbf{0}$	$\frac{1}{\sqrt[3]{2}} \cdot I_3$	$\mathbf{0}$

Table 3.3: Initial conditions for the heat conduction test

conditions for this problem are given in Table 3.3 on page 100.

The material parameters are taken to be: $\gamma = 1.4$, $c_v = 2.5$, $\rho_0 = 1$, $p_0 = 1$, $c_s = 1$, c_t , $\mu = 10^{-2}$, $\kappa = 10^{-2}$. An interface is initially placed between the two volumes of air at $x = 0.5$. The final time is taken to be $t = 1$, and 200 cells are used. Results are displayed in Figure 3.12 on page 101, using the results from [24] as a reference. The material interface is denoted by a dashed vertical line.

The temperature curve generated using the GPR-RGFM matches very well the reference solution. The interface has moved to $x = 0.53756$, as is to be expected, as the cooler gas on the left expands as it heats up, and the hotter gas on the right contracts as it cools. Initially, the mass of the left volume is 1 and the right volume is 0.25. At $t = 1$, these masses are 0.9997 and 0.2503, respectively. Thus, mass on either side is conserved to a good approximation. Although the GPR-RGFM results for the heat flux match the reference solution well over most of the domain, there are aberrations in a small region around the interface. Although this doesn't affect the temperature curve, these discrepancies are undesirable, and possible methods to rectify them are discussed in Chapter 5.

3.3.6 Intermaterial Heating-Induced Acoustic Wave

The test assesses the ability of the GPR-RGFM to conduct heat between two different materials. Take the material parameters for air and helium from Section 3.3.1. Take the scaled spatial variable x^* defined by:

$$x = \frac{\mu^{air} c_0^{air}}{p_0 \gamma^{air}} x^* \quad (3.38)$$

The domain $x^* \in [0, 90]$ is used. Thermal energy is added at the left boundary at a high power of $\frac{\gamma^{air} p_0 c_0^{air}}{P_r^{air} (\gamma^{air} - 1)}$ (around $1.7 \times 10^8 W m^{-2}$). Three scenarios are tested:

1. The domain is filled with air.

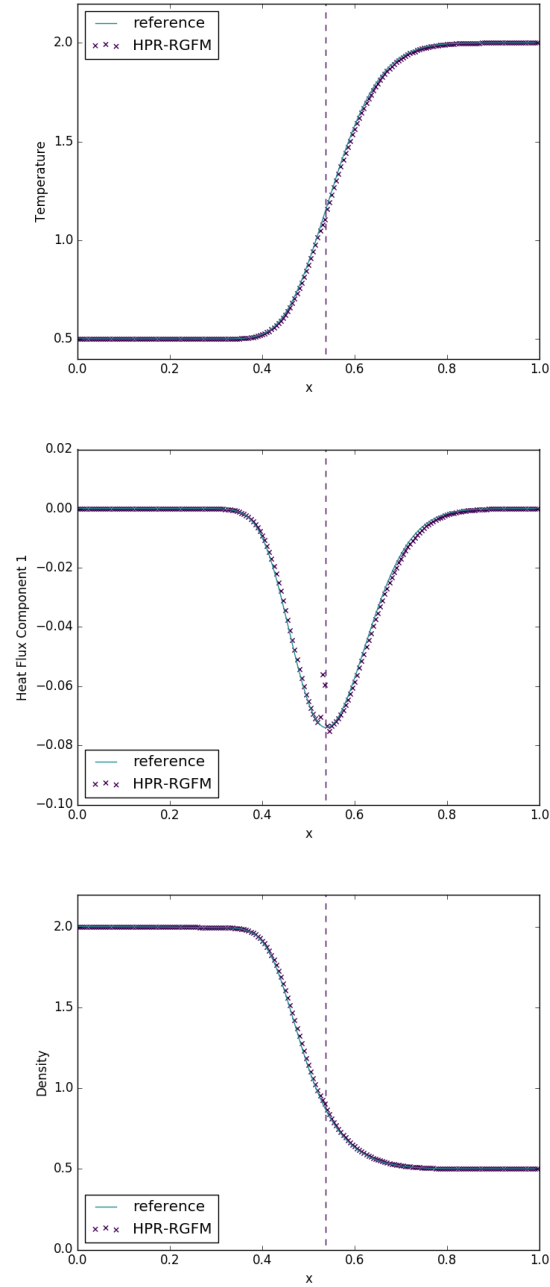


Figure 3.12: Temperature, heat flux, and density for the intermaterial heat conduction test with GPR-RGFM

	ρ	p	v	A	J
air	1.18	101325	$\mathbf{0}$	I_3	$\mathbf{0}$
helium	0.164	101325	$\mathbf{0}$	I_3	$\mathbf{0}$

Table 3.4: Initial conditions for the intermaterial heating-induced acoustic wave test

2. The domain comprises two volumes of air, initially separated at $x^* = 22.5$.
3. The domain comprises a volume of air (left) and a volume of helium (right), initially separated at $x^* = 22.5$.

The initial conditions for the two gases in all scenarios are given in Table 3.4 on page 102. The results of the test are shown in Figure 3.13 on page 103 and Figure 3.14 on page 104 for various times. The material interface is represented by a dashed vertical line in scenarios 2 and 3. All simulations used 400 cells.

As the left wall heats up, a temperature gradient develops and the acoustic wave described appears. The results for scenarios 1 and 2 are indistinguishable, as they should be, and there are no aberrations around the material interface in scenario 2. In scenario 3, the acoustic wave hits the interface at around $t = 2 \times 10^{-9}$ and then speeds up (as it should, the speed of sound in helium being around three times that of air). The heat flux wave increases in intensity after passing into the helium, owing to the fact that the wave is traveling faster. As expected, all variables displayed are continuous across the interface.

In scenarios 2 and 3 the interface moves to the right as the air heats up and expands. The masses of the air volumes in these two scenarios at various times are given in Table 3.5 on page 102, demonstrating that mass is conserved well as the interface moves.

Time ($\times 10^{-9}$)	0	1	2	3	4	5
Mass in Scenario 2 ($\times 10^{-6}$)	1.254	1.255	1.253	1.252	1.252	1.253
Mass in Scenario 3 ($\times 10^{-6}$)	1.254	1.253	1.248	1.254	1.255	1.255

Table 3.5: Mass of the air volume in scenarios 2 and 3 at various times

3.3 Numerical Results

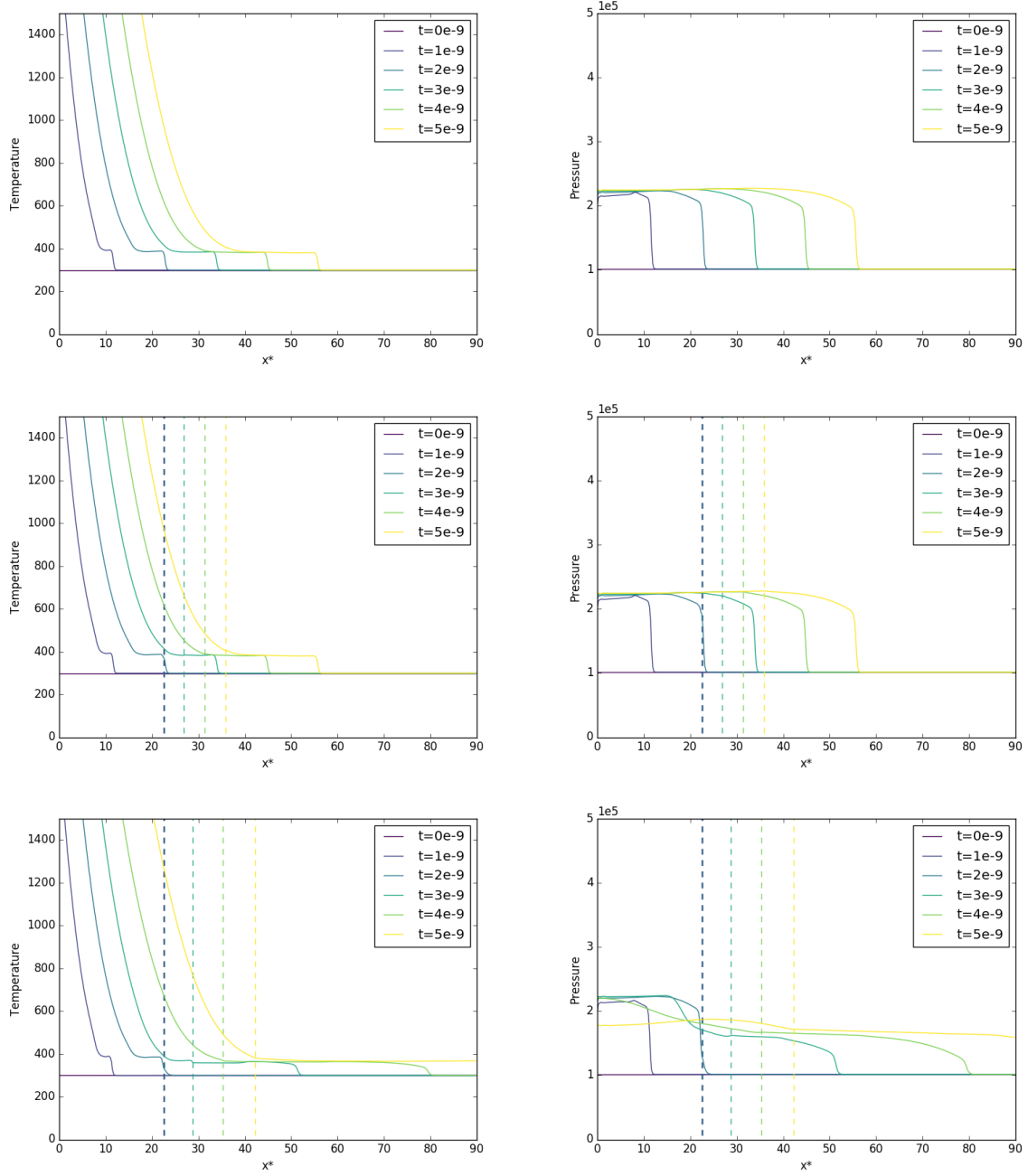


Figure 3.13: Temperature and pressure for the intermaterial heating-induced acoustic wave test with: a single volume of air (top); two volumes of air initially separated at $x^* = 22.5$ (middle); air and helium initially separated at $x^* = 22.5$ (bottom).

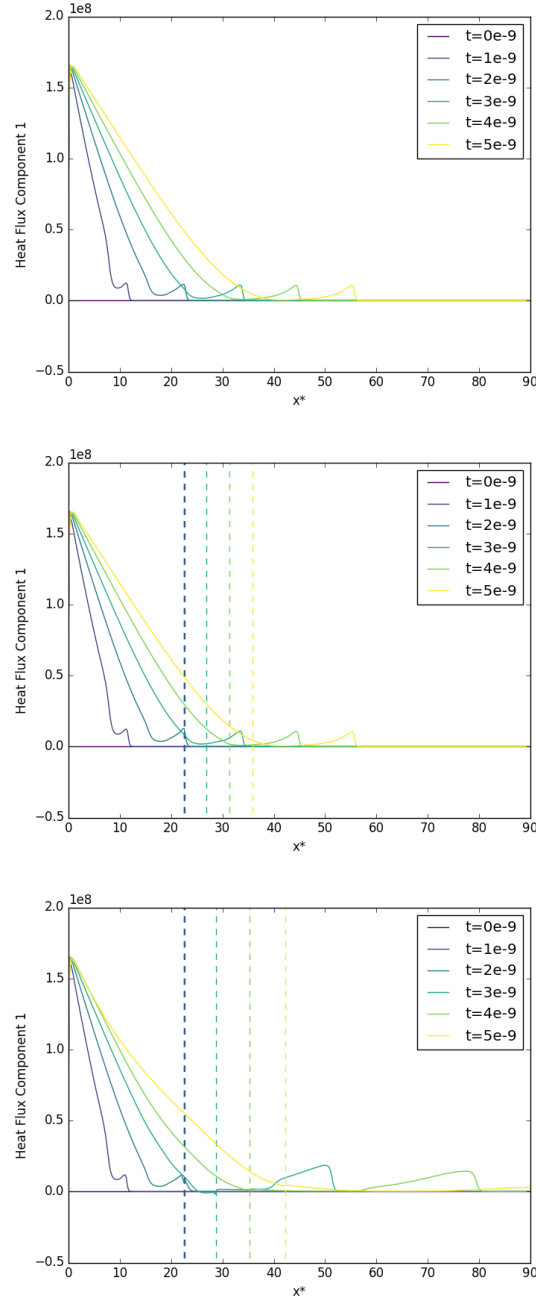


Figure 3.14: Heat flux for the intermaterial heating-induced acoustic wave test with: a single volume of air (top); two volumes of air initially separated at $x^* = 22.5$ (middle); air and helium initially separated at $x^* = 22.5$ (bottom).

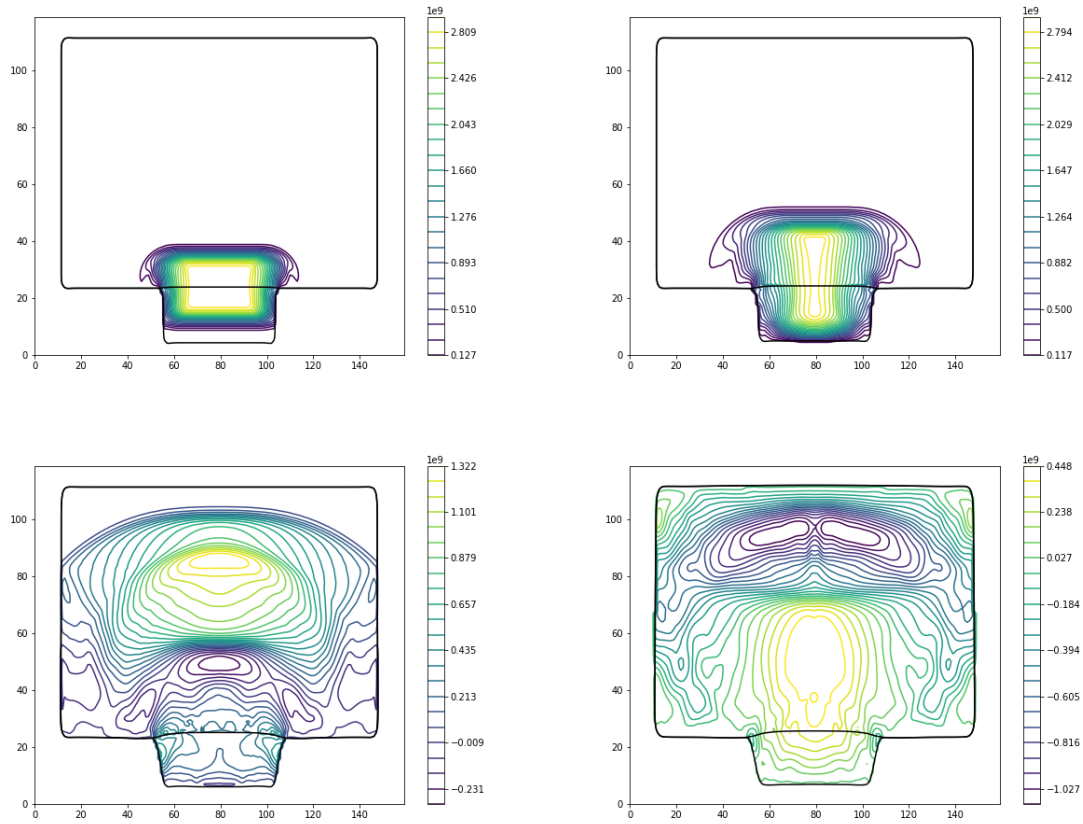


Figure 3.15: The aluminium plate impact test, at various different times

3.3.7 Aluminium Plates

In this test, an aluminium projectile impacts upon an aluminium plate at 400m/s. The domain is $[0, 0.03] \times [0, 0.04]$, with the projectile initially occupying $[0.001, 0.006] \times [0.014, 0.026]$, and the plate occupying $[0.006, 0.028] \times [0.003, 0.037]$. The surroundings are taken to be vacuum.

3.3.8 Taylor Bar

Chapter 4

Impact-Induced Detonation in an Elasto-Plastic Confiner

4.1 Reactive C4 Confined by Steel

[JWL, ignition and growth]

4.2 Reactive C4 Confined by Steel with Air Gap

4.3 Rod Impact on Copper Vessel

Chapter 5

Conclusions & Discussion

References

- [1] F. ALCRUDO AND F. BENKHALDOUN, *Exact solutions to the Riemann problem of the shallow water equations with a bottom step*, Computers & Fluids, 30 (2001), pp. 643–671.
- [2] H. ALKANDRY, I. BOYD, AND A. MARTIN, *Comparison of Models for Mixture Transport Properties for Numerical Simulations of Ablative Heat-Shields*, in 51st AIAA Aerospace Sciences Meeting including the New Horizons Forum and Aerospace Exposition, Grapevine (Dallas/Ft. Worth Region), Texas, Jan. 2013, American Institute of Aeronautics and Astronautics.
- [3] S. ARRHENIUS, *The heat of dissociation of electrolytes and the influence of temperature on the degree of dissociation*, Wilhelm Engelmann, 1889.
- [4] ———, *On the Reaction Velocity of the Inversion of Cane Sugar by Acids*, Zeitschrift für Physikalische Chemie, 4 (1889), pp. 226–248.
- [5] D. S. BALSARA, T. RUMPF, M. DUMBSER, AND C. D. MUNZ, *Efficient, high accuracy ADER-WENO schemes for hydrodynamics and divergence-free magnetohydrodynamics*, Journal of Computational Physics, 228 (2009), pp. 2480–2516.
- [6] P. T. BARTON AND D. DRIKAKIS, *An Eulerian method for multi-component problems in non-linear elasticity with sliding interfaces*, Journal of Computational Physics, 229 (2010), pp. 5518–5540.
- [7] P. T. BARTON, D. DRIKAKIS, E. ROMENSKI, AND V. A. TITAREV, *Exact and approximate solutions of Riemann problems in non-linear elasticity*, Journal of Computational Physics, 228 (2009), pp. 7046–7068.
- [8] P. T. BARTON, D. DRIKAKIS, AND E. I. ROMENSKI, *An Eulerian finite-volume scheme for large elastoplastic deformations in solids*, International Journal for Numerical Methods in Engineering, 81 (2011), pp. 453–484.
- [9] P. T. BARTON, B. OBADIA, AND D. DRIKAKIS, *A conservative level-set based method for compressible solid/fluid problems on fixed grids*, Journal of Computational Physics, 230 (2011), pp. 7867–7890.

-
- [10] R. BECKER, *Impact Waves and Detonation*, Zeitschrift fur Physik, 8 (1929), pp. 381–381.
- [11] B. C. BELL AND K. S. SURANA, *p-version least squares finite element formulation for two-dimensional, incompressible, non-Newtonian isothermal and non-isothermal fluid flow*, International Journal for Numerical Methods in Fluids, 18 (1994), pp. 127–162.
- [12] F. G. BLOTTNER, M. JOHNSON, AND M. ELLIS, *CHEMICALLY REACTING VISCOUS FLOW PROGRAM FOR MULTI-COMPONENT GAS MIXTURES.*, tech. rep., Sandia Labs., Albuquerque, N. Mex., 1971.
- [13] W. BOSCHERI, M. DUMBSER, AND R. LOUBERE, *Cell centered direct Arbitrary-Lagrangian-Eulerian ADER-WENO finite volume schemes for nonlinear hyperelasticity*, Computers and Fluids, 134-135 (2016), pp. 111–129.
- [14] D. L. CHAPMAN, *On the Rate of Explosion in Gases*, Philosophical Magazine Series 5, 47 (1899), pp. 90–104.
- [15] J. F. CLARKE, D. R. KASSOY, AND N. RILEY, *Shocks generated in a confined gas due to rapid heat addition at the boundary*, Proceedings of the Royal Society of London A, 393 (1984), pp. 309–329.
- [16] J. F. CLARKE, D. R. KASSOY, AND N. RILEY, *On the direct initiation of a plane detonation wave*, Proc. Roy. Soc. London, (1986).
- [17] J. F. CLARKE, D. R. KASSOY, AND N. RILEY, *On the evolution of plane detonations*, Proceedings of the Royal Society of London A, 429 (1990), pp. 259–283.
- [18] W. DORING, *On detonation processes in gases*, Annalen der Physik, 43 (1943), pp. 421–436.
- [19] M. DUMBSER AND D. S. BALSARA, *A new efficient formulation of the HLLEM Riemann solver for general conservative and non-conservative hyperbolic systems*, Journal of Computational Physics, 304 (2016), pp. 275–319.
- [20] M. DUMBSER AND W. BOSCHERI, *High-Order Unstructured Lagrangian One-Step WENO Finite Volume Schemes for Non-conservative Hyperbolic Systems: Applications to Compressible Multi-Phase Flows*, Elsevier Science, (2013).

-
- [21] M. DUMBSER, M. CASTRO, C. PARES, AND E. F. TORO, *ADER schemes on unstructured meshes for nonconservative hyperbolic systems: Applications to geophysical flows*, *Computers & Fluids*, 38 (2009), pp. 1731–1748.
- [22] M. DUMBSER, C. ENAUX, AND E. F. TORO, *Finite volume schemes of very high order of accuracy for stiff hyperbolic balance laws*, *Journal of Computational Physics*, 227 (2008), pp. 3971–4001.
- [23] M. DUMBSER, A. HIDALGO, AND O. ZANOTTI, *High order space-time adaptive ADER-WENO finite volume schemes for non-conservative hyperbolic systems*, *Computer Methods in Applied Mechanics and Engineering*, 268 (2014), pp. 359–387.
- [24] M. DUMBSER, I. PESHKOV, E. ROMENSKI, AND O. ZANOTTI, *High order ADER schemes for a unified first order hyperbolic formulation of continuum mechanics: viscous heat-conducting fluids and elastic solids*, *Journal of Computational Physics*, 314 (2015), pp. 824–862.
- [25] M. DUMBSER AND E. F. TORO, *On universal Osher-type schemes for general nonlinear hyperbolic conservation laws*, *Communications in Computational Physics*, 10 (2011), pp. 635–671.
- [26] M. DUMBSER AND E. F. TORO, *A simple extension of the Osher Riemann solver to non-conservative hyperbolic systems*, *Journal of Scientific Computing*, 48 (2011), pp. 70–88.
- [27] M. DUMBSER AND O. ZANOTTI, *Very high order PNPM schemes on unstructured meshes for the resistive relativistic MHD equations*, *Journal of Computational Physics*, 228 (2009), pp. 6991–7006.
- [28] M. DUMBSER, O. ZANOTTI, A. HIDALGO, AND D. S. BALSARA, *ADER-WENO finite volume schemes with space-time adaptive mesh refinement*, *Journal of Computational Physics*, 248 (2013), pp. 257–286.
- [29] R. FEDKIW AND X. LIU, *The ghost fluid method for viscous flows*, (1998), pp. 1–33.
- [30] L. L. FERRAS, J. M. NOBREGA, AND F. T. PINHO, *Analytical solutions for Newtonian and inelastic non-Newtonian flows with wall slip*, *Journal of Non-Newtonian Fluid Mechanics*, 175–176 (2012), pp. 76–88.
- [31] J. FRENKEL, *Kinetic Theory of Liquids*, Oxford University Press, 1947.

-
- [32] M. B. GILES, *An extended collection of matrix derivative results for forward and reverse mode algorithmic differentiation*, Tech. Rep. 9783540689355, 2008.
- [33] J. GLIMM AND D. MARCHESIN, *A Numerical Method for Two Phase Flow with an Unstable Interface*, *Journal of Computational Physics*, 39 (1981), pp. 179–200.
- [34] L. GRUNBERG AND A. H. NISSAN, *Mixture Law for Viscosity*, *Nature*, 164 (1949), p. 799.
- [35] R. N. GUPTA, J. M. YOS, R. A. THOMPSON, AND K.-P. LEE, *A review of reaction rates and thermodynamic and transport properties for an 11-species air model for chemical and thermal nonequilibrium calculations to 30000 K*, (1990).
- [36] C. HELZEL, R. J. LEVEQUE, AND G. WARNECKE, *A Modified Fractional Step Method for the Accurate Approximation of Detonation Waves*, *SIAM Journal on Scientific Computing*, 22 (2000), pp. 1489–1510.
- [37] F. HERNING AND L. ZIPPERER, *Calculation of the viscosity of technical gas mixtures from the viscosity of the individual gases*, *Gas u. Wasserfach*, 79 (1936), p. 69.
- [38] A. HIDALGO AND M. DUMBSER, *ADER schemes for nonlinear systems of stiff advection-diffusion-reaction equations*, *Journal of Scientific Computing*, 48 (2011), pp. 173–189.
- [39] H. JACKSON, *A Fast Numerical Scheme for the Godunov-Peshkov-Romenski Model of Continuum Mechanics*, *Journal of Computational Physics*, 348 (2017), pp. 514–533.
- [40] —, *On the Eigenvalues of the ADER-WENO Galerkin Predictor*, *Journal of Computational Physics*, 333 (2017), pp. 409–413.
- [41] G. S. JIANG AND C. W. SHU, *Efficient implementation of weighted WENO schemes*, *Journal of Computational Physics*, 126 (1996), pp. 202–228.
- [42] B. M. JOHNSON, *Analytical shock solutions at large and small Prandtl number*, *Journal of Fluid Mechanics*, 726 (2013).
- [43] E. JOUQUET, *On the Propagation of Chemical Reactions in Gases*, *Journal de Mathématiques Pures et Appliquées*, 1 (1905), pp. 347–425.

-
- [44] A. KAPILA, D. W. SCHWENDEMAN, J. J. QUIRK, AND T. HAWA, *Mechanisms of detonation formation due to a temperature gradient*, Combustion Theory & Modelling, 6 (2002), pp. 553–594.
- [45] R. LEVEQUE AND H. YEE, *A Study of Numerical Methods for Hyperbolic Conservation Laws with Stiff Source Terms*, Journal of Computational Physics, 86 (1990), pp. 187–210.
- [46] T. G. LIU, B. C. KHOO, AND K. S. YEO, *Ghost fluid method for strong shock impacting on material interface*, Journal of Computational Physics, 190 (2003), pp. 651–681.
- [47] T.-P. LIU, *The Riemann problem for general systems of conservation laws*, Journal of Differential Equations, 18 (1975), pp. 218–234.
- [48] X.-D. LIU, S. OSHER, AND T. CHAN, *Weighted Essentially Non-oscillatory Schemes*, Journal of Computational Physics, 115 (1994), pp. 200–212.
- [49] P. H. MAIRE, R. ABGRALL, J. BREIL, R. LOUBERE, AND B. REBOURCET, *A nominally second-order cell-centered Lagrangian scheme for simulating elastic-plastic flows on two-dimensional unstructured grids*, Journal of Computational Physics, 235 (2013), pp. 626–665.
- [50] A. N. MALYSHEV AND E. I. ROMENSKII, *Hyperbolic equations for heat transfer. Global solvability of the Cauchy problem*, Siberian Mathematical Journal, 27 (1986), pp. 734–740.
- [51] A. MCADAMS, A. SELLE, R. TAMSTORF, J. TERAN, AND E. SIFAKIS, *Computing the Singular Value Decomposition of 3×3 matrices with minimal branching and elementary floating point operations*, University of Wisconsin Madison, (2011).
- [52] R. MENIKOFF, *Complete Mie-Gruneisen Equation of State*, tech. rep., 2016.
- [53] G. H. MILLER, *An iterative Riemann solver for systems of hyperbolic conservation laws, with application to hyperelastic solid mechanics*, Journal of Computational Physics, 193 (2004), pp. 198–225.
- [54] G. I. MONTECINOS AND D. S. BALSARA, *A cell-centered polynomial basis for efficient Galerkin predictors in the context of ADER finite volume schemes. The one-dimensional case*, Computers & Fluids, 156 (2017), pp. 220–238.

-
- [55] M. MORDUCHOW AND P. A. LIBBY, *On a Complete Solution of the One-Dimensional Flow Equations of a Viscous, Heat-Conducting, Compressible Gas*, tech. rep., 1949.
- [56] P. NEOFYTOU, *A 3rd order upwind finite volume method for generalised Newtonian fluid flows*, *Advances in Engineering Software*, 36 (2005), pp. 664–680.
- [57] E. D. NERING, *Linear Algebra and Matrix Theory*, 1970.
- [58] T. E. OLIPHANT, *Python for Scientific Computing*, *Computing in Science & Engineering*, 9 (2007), pp. 10–20.
- [59] S. OSHER AND R. FEDKIW, *Level set methods and dynamic implicit surfaces*, 2003.
- [60] I. PESHKOV, W. BOSCHERI, R. LOUBĚŠRE, E. ROMENSKI, AND M. DUMBSER, *Theoretical and numerical comparison of hyperelastic and hypoelastic formulations for Eulerian non-linear elastoplasticity*, arXiv:1806.00706 [physics], (2018). arXiv: 1806.00706.
- [61] I. PESHKOV AND E. ROMENSKI, *A hyperbolic model for viscous Newtonian flows*, *Continuum Mechanics and Thermodynamics*, 28 (2016), pp. 85–104.
- [62] E. ROMENSKI, D. DRIKAKIS, AND E. TORO, *Conservative models and numerical methods for compressible two-phase flow*, *Journal of Scientific Computing*, 42 (2010), pp. 68–95.
- [63] E. ROMENSKI, A. D. RESNYANSKY, AND E. F. TORO, *Conservative hyperbolic model for compressible two-phase flow with different phase pressures and temperatures*, *Quarterly of applied mathematics*, 65(2) (2007), pp. 259–279.
- [64] E. I. ROMENSKI, *Hyperbolic equations of Maxwell's nonlinear model of elastoplastic heat-conducting media*, *Siberian Mathematical Journal*, 30 (1989), pp. 606–625.
- [65] S. K. SAMBASIVAN AND H. S. UDAYKUMAR, *Ghost Fluid Method for Strong Shock Interactions Part 1: Fluid-Fluid Interfaces*, *AIAA Journal*, 47 (2009), pp. 2907–2922.
- [66] —, *Ghost Fluid Method for Strong Shock Interactions Part 2: Immersed Solid Boundaries*, *AIAA Journal*, 47 (2009), pp. 2923–2937.
- [67] M. SHORT, *On the Critical Conditions for the Initiation of a Detonation in a Nonuniformly Perturbed Reactive Fluid*, *SIAM Journal on Applied Mathematics*, 57 (1997), pp. 1242–1280.

- [68] K. SVERDRUP, N. NIKIFORAKIS, AND A. ALMGREN, *Highly parallelisable simulations of time-dependent viscoplastic fluid flow with structured adaptive mesh refinement*, Physics of Fluids, 30 (2018), p. 093102.
- [69] E. F. TORO, *Riemann Solvers and Numerical Methods for fluid dynamics*, vol. 40, 2009.
- [70] J. VON NEUMANN, *Theory of Detonation Waves*, tech. rep., 1942.
- [71] S. P. WANG, M. H. ANDERSON, J. G. OAKLEY, M. L. CORRADINI, AND R. BONAZZA, *A thermodynamically consistent and fully conservative treatment of contact discontinuities for compressible multicomponent flows*, Journal of Computational Physics, 195 (2004), pp. 528–559.
- [72] C. R. WILKE, *A viscosity equation for gas mixtures*, The journal of chemical physics, 18 (1950), pp. 517–519.
- [73] Y. B. ZELDOVICH, *On the Theory of the Propagation of Detonation in Gaseous Systems*, Journal of Experimental & Theoretical Physics, 10 (1940), pp. 542–568.

Appendix A

System Matrices

A.1 Fluxes, Sources, and Non-Conservative Terms

The mixed-material GPR model takes the form $\frac{\partial \mathbf{Q}}{\partial t} + \frac{\partial \mathbf{F}(\mathbf{Q})}{\partial x} + \mathbf{B}(\mathbf{Q}) \cdot \frac{\partial \mathbf{Q}}{\partial x} = \mathbf{S}(\mathbf{Q})$ where $\mathbf{Q}, \mathbf{F}, \mathbf{B}, \mathbf{S}$ are given below.

A.2 Jacobians

Jacobian of the Conserved System

Define the following variables:

$$\tilde{\psi} = \left. \frac{\partial E}{\partial A} \right|_{\rho, p} \quad (\text{A.1a})$$

$$\Psi_{ij} = \rho v_i v_j - \sigma_{ij} \quad (\text{A.1b})$$

$$\Phi_{ij} = v_i v_j - \frac{\partial \sigma_{ij}}{\partial \rho} \quad (\text{A.1c})$$

$$\Omega_{ij}^k = \rho v_k \tilde{\psi}_{ij} - v_m \frac{\partial \sigma_{mk}}{\partial A_{ij}} \quad (\text{A.1d})$$

$$\Delta_i = v_i \left(E + \rho \left. \frac{\partial E}{\partial \rho} \right|_{p, A} \right) - \frac{\partial \sigma_{im}}{\partial \rho} v_m + \frac{\partial T}{\partial \rho} H_i \quad (\text{A.1e})$$

$$\Pi_i = v_i \left(\rho \frac{\partial E}{\partial p} + 1 \right) + \frac{\partial T}{\partial p} H_i \quad (\text{A.1f})$$

$$\Upsilon = \Gamma \left(\|\mathbf{v}\|^2 + c_t^2 \|\mathbf{J}\|^2 + Q\lambda - \left(E + \rho \left. \frac{\partial E}{\partial \rho} \right|_{p, A} \right) \right) \quad (\text{A.1g})$$

The Jacobians of the GPR system are given on the following pages.

$$\begin{aligned}
 \mathbf{Q} &= \begin{pmatrix} \rho \\ \rho E \\ \rho v_1 \\ \rho v_2 \\ \rho v_3 \\ A_{11} \\ A_{12} \\ A_{13} \\ A_{21} \\ A_{22} \\ A_{23} \\ A_{31} \\ A_{32} \\ A_{33} \\ \rho J_1 \\ \rho J_2 \\ \rho J_3 \\ \rho \lambda \end{pmatrix} & \mathbf{F}_1 &= \begin{pmatrix} \rho v_1 \\ \rho v_1 E + v_1 p - v_m \sigma_{m1} + q_1 \\ \rho v_1^2 + p - \sigma_{11} \\ \rho v_1 v_2 - \sigma_{21} \\ \rho v_1 v_3 - \sigma_{31} \\ A_{1m} v_m \\ 0 \\ 0 \\ A_{2m} v_m \\ 0 \\ 0 \\ A_{3m} v_m \\ 0 \\ 0 \\ \rho J_1 v_1 + T \\ \rho J_2 v_1 \\ \rho J_3 v_1 \\ \rho \lambda v_1 \end{pmatrix} \\
 & & \mathbf{F}_2 &= \begin{pmatrix} \rho v_2 \\ \rho v_2 E + v_2 p - v_m \sigma_{m2} + q_2 \\ \rho v_1 v_2 - \sigma_{12} \\ \rho v_2^2 + p - \sigma_{22} \\ \rho v_2 v_3 - \sigma_{32} \\ 0 \\ A_{1m} v_m \\ 0 \\ 0 \\ A_{2m} v_m \\ 0 \\ 0 \\ A_{3m} v_m \\ 0 \\ \rho J_1 v_2 \\ \rho J_2 v_2 + T \\ \rho J_3 v_2 \\ \rho \lambda v_2 \end{pmatrix} \\
 & & \mathbf{F}_3 &= \begin{pmatrix} \rho v_3 \\ \rho v_3 E + v_3 p - v_m \sigma_{m3} + q_3 \\ \rho v_1 v_3 - \sigma_{13} \\ \rho v_2 v_3 - \sigma_{23} \\ \rho v_3^2 + p - \sigma_{33} \\ 0 \\ 0 \\ A_{1m} v_m \\ 0 \\ 0 \\ A_{2m} v_m \\ 0 \\ 0 \\ A_{3m} v_m \\ \rho J_1 v_3 \\ \rho J_2 v_3 \\ \rho J_3 v_3 + T \\ \rho \lambda v_3 \end{pmatrix}
 \end{aligned}$$

$$B_2 =$$

$$B_3 =$$

$$\frac{\partial Q}{\partial P} =$$

[illegible]

[illegible]

Jacobian of Distortion ODEs

The Jacobian of the source function is used to speed up numerical integration of the ODE. It is derived thus:

$$\frac{\partial \text{dev}(G)_{ij}}{\partial A_{mn}} = \delta_{in} A_{mj} + \delta_{jn} A_{mi} - \frac{2}{3} \delta_{ij} A_{mn} \quad (\text{A.2})$$

Thus:

$$\begin{aligned} \frac{\partial (A \text{dev}(G))_{ij}}{\partial A_{mn}} &= \frac{\partial A_{it}}{\partial A_{mn}} \text{dev}(G)_{tj} + A_{it} \frac{\partial \text{dev}(G)_{tj}}{\partial A_{mn}} \\ &= \delta_{im} \delta_{tn} \left(A_{kt} A_{kj} - \frac{1}{3} A_{kl} A_{kl} \delta_{tj} \right) + A_{it} \left(\delta_{tn} A_{mj} + \delta_{jn} A_{mt} - \frac{2}{3} \delta_{tj} A_{mn} \right) \\ &= \delta_{im} A_{kn} A_{kj} - \frac{1}{3} \delta_{im} \delta_{jn} A_{kl} A_{kl} + A_{in} A_{mj} + \delta_{jn} A_{ik} A_{mk} - \frac{2}{3} A_{ij} A_{mn} \end{aligned} \quad (\text{A.3})$$

Thus:

$$\begin{aligned} J_A &\equiv \frac{-3}{\tau_1} \frac{\partial \left(\det(A)^{\frac{5}{3}} A \text{dev}(G) \right)_{ij}}{\partial A_{mn}} \\ &= \frac{-3}{\tau_1} \det(A)^{\frac{5}{3}} \left(\frac{5}{3} (A \text{dev}(G))_{ij} A_{mn}^{-T} + A_{in} A_{mj} + \delta_{jn} G'_{im} + \delta_{im} G_{jn} - \frac{1}{3} \delta_{im} \delta_{jn} A_{kl} A_{kl} - \frac{2}{3} A_{ij} A_{mn} \right) \\ &= \frac{1}{\tau_1} \det(A)^{\frac{5}{3}} \left(-5 (A \text{dev}(G)) \otimes A^{-T} + 2A \otimes A - 3(A \otimes A)^{1,3} + \|A\|_F^2 (I \otimes I)^{2,3} - 3(G' \otimes I + I \otimes G') \right) \end{aligned} \quad (\text{A.4})$$

where $G' = AA^T$ and $X^{a,b}$ refers to tensor X with indices a, b transposed.

Jacobian of Thermal Impulse ODEs

As demonstrated in 2.2.2, we have:

$$\frac{dJ_i}{dt} = \frac{J_i}{2} \left(-a + b (J_1^2 + J_2^2 + J_3^2) \right) \quad (\text{A.5})$$

where

$$a = \frac{2\rho_0}{\tau_2 T_0 \rho c_v} (E - E_{2A}(A) - E_3(\mathbf{v})) \quad (\text{A.6a})$$

$$b = \frac{\rho_0 c_t^2}{\tau_2 T_0 \rho c_v} \quad (\text{A.6b})$$

Thus, the Jacobian of the thermal impulse ODEs is:

$$\begin{pmatrix} \frac{b}{2}(3J_1^2 + J_2^2 + J_3^2) - \frac{a}{2} & bJ_1J_2 & bJ_1J_3 \\ bJ_1J_2 & \frac{b}{2}(J_1^2 + 3J_2^2 + J_3^2) - \frac{a}{2} & bJ_2J_3 \\ bJ_1J_3 & bJ_2J_3 & \frac{b}{2}(J_1^2 + J_2^2 + 3J_3^2) - \frac{a}{2} \end{pmatrix} \quad (\text{A.7})$$

Appendix B

Eigenstructure

B.1 Primitive System

Taking the ordering \mathbf{P} of primitive variables in (B.13), note that (3), (1b), (1c), (1d) can be stated as:

$$\frac{D\rho}{Dt} + \rho \frac{\partial v_k}{\partial x_k} = 0 \quad (\text{B.1a})$$

$$\frac{Dv_i}{Dt} + \frac{1}{\rho} \frac{\partial \Sigma_{ik}}{\partial x_k} = 0 \quad (\text{B.1b})$$

$$\frac{DA_{ij}}{Dt} + A_{ik} \frac{\partial v_k}{\partial x_j} = -\frac{\psi_{ij}}{\theta_1} \quad (\text{B.1c})$$

$$\frac{DJ_i}{Dt} + \frac{1}{\rho} \frac{\partial T \delta_{ik}}{\partial x_k} = -\frac{H_i}{\theta_2} \quad (\text{B.1d})$$

$$\frac{DE}{Dt} + \frac{1}{\rho} \frac{\partial (\Sigma_{ik} v_i + T H_k)}{\partial x_k} = 0 \quad (\text{B.1e})$$

$$\frac{D\lambda}{Dt} = -K \quad (\text{B.1f})$$

where the total stress tensor $\Sigma = pI + \rho A^T \psi$. Note that:

$$\begin{aligned} \frac{DE}{Dt} &= \frac{\partial E}{\partial p} \frac{Dp}{Dt} + \frac{\partial E}{\partial \rho} \frac{D\rho}{Dt} + v_i \frac{Dv_i}{Dt} + \frac{\partial E}{\partial A_{ij}} \frac{DA_{ij}}{Dt} + H_i \frac{DJ_i}{Dt} + \frac{\partial E}{\partial \lambda} \frac{D\lambda}{Dt} \\ &= \frac{\partial E}{\partial p} \frac{Dp}{Dt} - \rho \frac{\partial E}{\partial \rho} \frac{\partial v_k}{\partial x_k} - \frac{1}{\rho} v_i \frac{\partial \Sigma_{ik}}{\partial x_k} - \frac{\partial E}{\partial A_{ij}} \left(A_{ik} \frac{\partial v_k}{\partial x_j} + \frac{\psi_{ij}}{\theta_1} \right) - H_i \left(\frac{1}{\rho} \frac{\partial T \delta_{ik}}{\partial x_k} + \frac{H_i}{\theta_2} \right) - \frac{\partial E}{\partial \lambda} K \end{aligned} \quad (\text{B.2})$$

Thus, the energy equation becomes:

$$\frac{\partial E}{\partial p} \frac{Dp}{Dt} - \rho \frac{\partial E}{\partial \rho} \frac{\partial v_k}{\partial x_k} - \frac{1}{\rho} v_i \frac{\partial \Sigma_{ik}}{\partial x_k} - \frac{\partial E}{\partial A_{ij}} A_{ik} \frac{\partial v_k}{\partial x_j} - \frac{H_k}{\rho} \frac{\partial T}{\partial x_k} + \frac{1}{\rho} \frac{\partial (\Sigma_{ik} v_i + T H_k)}{\partial x_k} = \frac{\partial E}{\partial A_{ij}} \frac{\psi_{ij}}{\theta_1} + \frac{H_i H_i}{\theta_2} + \frac{\partial E}{\partial \lambda} K \quad (\text{B.3})$$

Simplifying:

$$\frac{Dp}{Dt} + \frac{1}{\rho E_p} \left(\Sigma_{ik} - \rho A_{ji} \frac{\partial E}{\partial A_{jk}} - \rho^2 \frac{\partial E}{\partial \rho} \delta_{ik} \right) \frac{\partial v_i}{\partial x_k} + \frac{T}{\rho E_p} \frac{\partial H_k}{\partial x_k} = \frac{\partial E}{\partial A_{ij}} \frac{\psi_{ij}}{\theta_1 E_p} + \frac{H_i H_i}{\theta_2 E_p} + \frac{E_\lambda}{E_p} K \quad (\text{B.4})$$

We have¹²³:

$$\frac{p - \rho^2 E_\rho}{\rho E_p} = \rho c_0^2 \quad (\text{B.9a})$$

$$\frac{c_t^2 T}{\rho E_p} = \frac{\rho c_h^2}{T_p} \quad (\text{B.9b})$$

$$\left. \frac{\partial E}{\partial A} \right|_{\rho, p} = \left(1 - 2\rho^2 E_p \frac{\partial \log(c_s)}{\partial \rho} \right) \psi \quad (\text{B.9c})$$

$$-\rho A^T \left. \frac{\partial E}{\partial A} \right|_{\rho, p} = \sigma + \rho^2 E_p \left(\frac{\sigma}{\rho} - \frac{\partial \sigma}{\partial \rho} \right) \quad (\text{B.9d})$$

1

$$\begin{aligned} \frac{p - \rho^2 E_\rho}{\rho E_p} &= \frac{\rho^2 E_\rho|_s - \rho^2 E_\rho|_p}{\rho E_p|_\rho} = \rho \frac{E_\rho|_s - (E_\rho|_s + E_s|_\rho s_\rho|_p)}{E_s|_\rho s_p|_\rho} \\ &= \rho \frac{-s_\rho|_p}{s_p|_\rho} = \rho \left. \frac{\partial p}{\partial \rho} \right|_s \end{aligned} \quad (\text{B.5})$$

2

$$\frac{c_t^2 T}{\rho E_p} = \frac{c_t^2 T}{\rho c_v T_p} = \frac{\rho c_h^2}{T_p} \quad (\text{B.6})$$

3

$$\left. \frac{\partial E}{\partial A} \right|_{\rho, p} = \left(c_s^2 - \frac{\rho}{\Gamma} \frac{\partial c_s^2}{\partial \rho} \right) \frac{\psi}{c_s^2} = \left(1 - 2 \frac{\rho^2}{\rho \Gamma} \frac{\partial \log(c_s)}{\partial \rho} \right) \psi \quad (\text{B.7})$$

$$\begin{aligned} \frac{\partial \sigma}{\partial \rho} &= \frac{\partial}{\partial \rho} \left(-\rho c_s^2 A^T \frac{\psi}{c_s^2} \right) = -c_s^2 A^T \frac{\psi}{c_s^2} - \rho \frac{\partial c_s^2}{\partial \rho} A^T \frac{\psi}{c_s^2} \\ &= \frac{\sigma}{\rho} + 2 \frac{\partial \log(c_s)}{\partial \rho} \sigma \end{aligned} \quad (\text{B.8})$$

The full system then becomes:

$$\frac{D\rho}{Dt} + \rho \frac{\partial v_k}{\partial x_k} = 0 \quad (\text{B.10a})$$

$$\frac{Dp}{Dt} + \rho c_0^2 \frac{\partial v_i}{\partial x_i} + \left(\sigma_{ik} - \rho \frac{\partial \sigma_{ik}}{\partial \rho} \right) \frac{\partial v_i}{\partial x_k} + \frac{\rho c_h^2}{T_p} \frac{\partial J_k}{\partial x_k} = \left(1 - 2\rho^2 E_p \frac{\partial \log(c_s)}{\partial \rho} \right) \frac{\|\psi\|_F^2}{\theta_1 E_p} + \frac{\|H\|^2}{\theta_2 E_p} + \frac{E_\lambda}{E_p} K \quad (\text{B.10b})$$

$$\frac{DA_{ij}}{Dt} + A_{ik} \frac{\partial v_k}{\partial x_j} = -\frac{\psi_{ij}}{\theta_1} \quad (\text{B.10c})$$

$$\frac{Dv_i}{Dt} - \frac{1}{\rho} \frac{\partial \sigma_{ik}}{\partial \rho} \frac{\partial \rho}{\partial x_k} + \frac{1}{\rho} \frac{\partial p}{\partial x_i} - \frac{1}{\rho} \frac{\partial \sigma_{ik}}{\partial A_{mn}} \frac{\partial A_{mn}}{\partial x_k} = 0 \quad (\text{B.10d})$$

$$\frac{DJ_i}{Dt} + \frac{T_p}{\rho} \frac{\partial \rho}{\partial x_i} + \frac{T_p}{\rho} \frac{\partial p}{\partial x_i} = -\frac{H_i}{\theta_2} \quad (\text{B.10e})$$

$$\frac{D\lambda}{Dt} = -K \quad (\text{B.10f})$$

Thus, the GPR system can be written in the following form:

$$\frac{\partial \mathbf{P}}{\partial t} + \mathbf{M} \cdot \nabla \mathbf{P} = \mathbf{S}_p \quad (\text{B.11})$$

B.2 Eigenvalues

Considering the primitive system matrix (B.12), it is clear that the eigenvalues of the GPR system in the first spatial axis consist of v_1 repeated 8 times, along with the roots of:

$$\begin{vmatrix} (v_1 - \lambda) I & \Xi_2 \\ \Xi_1 & (v_1 - \lambda) I \end{vmatrix} = 0 \quad (\text{B.15})$$

where

$$\Xi_1 = \begin{pmatrix} -\frac{1}{\rho} \frac{\partial \sigma_{11}}{\partial \rho} & \frac{1}{\rho} & -\frac{1}{\rho} \frac{\partial \sigma_{11}}{\partial A_{11}} & -\frac{1}{\rho} \frac{\partial \sigma_{11}}{\partial A_{21}} & -\frac{1}{\rho} \frac{\partial \sigma_{11}}{\partial A_{31}} \\ -\frac{1}{\rho} \frac{\partial \sigma_{21}}{\partial \rho} & 0 & -\frac{1}{\rho} \frac{\partial \sigma_{21}}{\partial A_{11}} & -\frac{1}{\rho} \frac{\partial \sigma_{21}}{\partial A_{21}} & -\frac{1}{\rho} \frac{\partial \sigma_{21}}{\partial A_{31}} \\ -\frac{1}{\rho} \frac{\partial \sigma_{31}}{\partial \rho} & 0 & -\frac{1}{\rho} \frac{\partial \sigma_{31}}{\partial A_{11}} & -\frac{1}{\rho} \frac{\partial \sigma_{31}}{\partial A_{21}} & -\frac{1}{\rho} \frac{\partial \sigma_{31}}{\partial A_{31}} \\ \frac{T_p}{\rho} & \frac{T_p}{\rho} & 0 & 0 & 0 \end{pmatrix} \quad (\text{B.16})$$

[illegible]

$$\Xi_2 = \begin{pmatrix} \rho & 0 & 0 & 0 \\ (\rho c_0^2 + \sigma_{11} - \rho \frac{\partial \sigma_{11}}{\partial \rho}) & (\sigma_{21} - \rho \frac{\partial \sigma_{21}}{\partial \rho}) & (\sigma_{31} - \rho \frac{\partial \sigma_{31}}{\partial \rho}) & \frac{\rho c_h^2}{T_p} \\ A_{11} & A_{12} & A_{13} & 0 \\ A_{21} & A_{22} & A_{23} & 0 \\ A_{31} & A_{32} & A_{33} & 0 \end{pmatrix} \quad (\text{B.17})$$

By the properties of block matrices⁴, the remaining eigenvalues are v_1 and the roots of $|(v_1 - \lambda)^2 I - \Xi_1 \Xi_2| = 0$. Thus, $\lambda_i = v_1 \pm \sqrt{\tilde{\lambda}_i}$ where the $\tilde{\lambda}_i$ are the eigenvalues of the following matrix:

$$\Xi = \Xi_1 \Xi_2 = \begin{pmatrix} \Omega_{11}^1 + (c_0^2 + \frac{\sigma_{11}}{\rho} - \frac{\partial \sigma_{11}}{\partial \rho}) & \Omega_{12}^1 + (\frac{\sigma_{21}}{\rho} - \frac{\partial \sigma_{21}}{\partial \rho}) & \Omega_{13}^1 + (\frac{\sigma_{31}}{\rho} - \frac{\partial \sigma_{31}}{\partial \rho}) & \frac{c_h^2}{T_p} \\ \Omega_{21}^1 & \Omega_{22}^1 & \Omega_{23}^1 & 0 \\ \Omega_{31}^1 & \Omega_{32}^1 & \Omega_{33}^1 & 0 \\ T_\rho + T_p (c_0^2 + \frac{\sigma_{11}}{\rho} - \frac{\partial \sigma_{11}}{\partial \rho}) & T_p (\frac{\sigma_{21}}{\rho} - \frac{\partial \sigma_{21}}{\partial \rho}) & T_p (\frac{\sigma_{31}}{\rho} - \frac{\partial \sigma_{31}}{\partial \rho}) & c_h^2 \end{pmatrix} \quad (\text{B.18})$$

where Ω is given shortly. Similar results hold for the other two spatial directions. In general it is not possible to express the eigenvalues of Ξ in terms of the eigenvalues of its submatrices. Note, however, that if $c_t = 0$ then one of the eigenvalues is 0 and the remaining eigenvalues can be found analytically, using the form given in the appendix of [24].

It is straightforward to verify the following:

$$\frac{\partial \sigma_{ij}}{\partial A_{mn}} = -c_s^2 \rho \left(\delta_{in} (A \text{ dev } (G))_{mj} + \delta_{jn} (A \text{ dev } (G))_{mi} + A_{mi} G_{jn} + A_{mj} G_{in} - \frac{2}{3} G_{ij} A_{mn} \right) \quad (\text{B.19})$$

The quantity Ω is named here the *acoustic tensor*, due to its similarity to the acoustic tensor described in [7]:

⁴If A is invertible, $\det \begin{pmatrix} A & B \\ C & D \end{pmatrix} = \det(A) \det(D - CA^{-1}B)$

$$\begin{aligned}
 \Omega_{ij}^d &= -\frac{1}{\rho} \frac{\partial \sigma_{id}}{\partial A_{kd}} A_{kj} - \frac{\sigma_{id}}{\rho} \delta_{dj} \\
 &= c_s^2 \left(\delta_{id} (G \operatorname{dev} (G))_{dj} + (G \operatorname{dev} (G))_{id} \delta_{dj} \right. \\
 &\quad \left. + (G \operatorname{dev} (G))_{ij} + G_{ij} G_{dd} + \frac{1}{3} G_{dj} G_{id} \right) \\
 &= c_s^2 \left(E^d G \operatorname{dev} (G) + G \operatorname{dev} (G) E^d + G \operatorname{dev} (G) + G_{dd} G + \frac{1}{3} G_d G_d^T \right)
 \end{aligned} \tag{B.20}$$

where $E_{ij}^d = \delta_{id} \delta_{jd}$.

B.3 Eigenvectors

The following results are presented for an unmixed material ($z \equiv 0$).

With Heat Conduction

By hyperbolicity of the system, Ξ can be expressed as:

$$\Xi = Q^{-1} D^2 Q \tag{B.21}$$

where D is a diagonal matrix with positive diagonal entries. The eigenvectors corresponding to $\lambda_i = v_1 \pm \sqrt{\tilde{\lambda}_i}$ take the form $\begin{pmatrix} \hat{\mathbf{u}} & 0_6 & \tilde{\mathbf{u}} & 0_2 \end{pmatrix}^T$ where $\hat{\mathbf{u}} \in \mathbb{R}^5, \tilde{\mathbf{u}} \in \mathbb{R}^4$ satisfy:

$$\begin{pmatrix} v_1 I & \Xi_2 \\ \Xi_1 & v_1 I \end{pmatrix} \begin{pmatrix} \hat{\mathbf{u}} \\ \tilde{\mathbf{u}} \end{pmatrix} = \left(v_1 \pm \sqrt{\tilde{\lambda}_i} \right) \begin{pmatrix} \hat{\mathbf{u}} \\ \tilde{\mathbf{u}} \end{pmatrix} \tag{B.22}$$

Thus, $\Xi_2 \tilde{\mathbf{u}} = \pm \sqrt{\tilde{\lambda}_i} \hat{\mathbf{u}}$ and $\Xi_1 \hat{\mathbf{u}} = \pm \sqrt{\tilde{\lambda}_i} \tilde{\mathbf{u}}$. Combining these results, $\Xi \tilde{\mathbf{u}} = \tilde{\lambda}_i \tilde{\mathbf{u}}$. Thus, $\tilde{\mathbf{u}}$ is a right eigenvector of Ξ and, taking the form $Q^{-1} \mathbf{e}_i$ for some $i = 1 \dots 4$.

The four eigenvectors corresponding to eigenvalues of the form $v_1 + \sqrt{\tilde{\lambda}_i}$ are columns 1-4 of matrix R in (B.23). Those corresponding to eigenvalues of the form $v_1 - \sqrt{\tilde{\lambda}_i}$ are columns 5-8. By inspection, it can be verified that the remaining 9 eigenvectors (corresponding to eigenvalue v_1) are the remaining columns.

A similar analysis yields the left eigenvectors as the rows of (B.25).

$$R = \left\{ \begin{pmatrix} \frac{1}{2}\Xi_2 (D^2Q)^{-1} & \frac{1}{2}\Xi_2 (D^2Q)^{-1} \\ 0_{6,4} & 0_{6,4} \\ \frac{1}{2}(DQ)^{-1} & -\frac{1}{2}(DQ)^{-1} \\ 0_{2,4} & 0_{2,4} \end{pmatrix}, \begin{pmatrix} -cT_p \\ cT_p \\ c\Pi_d^{-1}\mathbf{w} \\ 0_{12,1} \end{pmatrix}, \begin{pmatrix} 0_{2,3} & 0_{2,3} \\ -\Pi_1^{-1}\Pi_2 & -\Pi_1^{-1}\Pi_3 \\ I_3 & 0_{3,3} \\ 0_{3,3} & I_3 \\ 0_{6,3} & 0_{6,3} \end{pmatrix}, \begin{pmatrix} 0_{15,2} \\ I_2 \end{pmatrix} \right\} \quad (\text{B.23})$$

where

$$\mathbf{w} = T_p \frac{\partial \sigma_d}{\partial \rho} + T_p \mathbf{e}_d \quad (\text{B.24a})$$

$$c = \frac{1}{\mathbf{e}_d^T (\Pi_d A)^{-1} \mathbf{w} + \frac{T_p}{\rho}} \quad (\text{B.24b})$$

$$L = \left\{ \begin{pmatrix} Q\Xi_1 - \frac{1}{\rho}Q_{:,1:3}\Pi_2 - \frac{1}{\rho}Q_{:,1:3}\Pi_3 & DQ & 0_{4,2} \\ Q\Xi_1 - \frac{1}{\rho}Q_{:,1:3}\Pi_2 - \frac{1}{\rho}Q_{:,1:3}\Pi_3 & -DQ & 0_{4,2} \\ -\frac{1}{\rho} & 0 & \mathbf{e}_d^T A^{-1} & \mathbf{e}_d^T A^{-1} \Pi_1^{-1} \Pi_2 & \mathbf{e}_d^T A^{-1} \Pi_1^{-1} \Pi_3 & 0_{1,6} \end{pmatrix}, \begin{pmatrix} 0_{3,5} & I_3 & 0_{3,3} & 0_{3,6} \\ 0_{3,5} & 0_{3,3} & I_3 & 0_{3,6} \\ 0_{2,15} & I_2 \end{pmatrix} \right\} \quad (\text{B.25})$$

Without Heat Conduction

If the system does not include the heat conduction terms, the eigenstructure of the system matrix changes. Ξ_1, Ξ_2, Ξ now take the following values:

$$\Xi_1 = \begin{pmatrix} -\frac{1}{\rho} \frac{\partial \sigma_{11}}{\partial \rho} & \frac{1}{\rho} & -\frac{1}{\rho} \frac{\partial \sigma_{11}}{\partial A_{11}} & -\frac{1}{\rho} \frac{\partial \sigma_{11}}{\partial A_{21}} & -\frac{1}{\rho} \frac{\partial \sigma_{11}}{\partial A_{31}} \\ -\frac{1}{\rho} \frac{\partial \sigma_{21}}{\partial \rho} & 0 & -\frac{1}{\rho} \frac{\partial \sigma_{21}}{\partial A_{11}} & -\frac{1}{\rho} \frac{\partial \sigma_{21}}{\partial A_{21}} & -\frac{1}{\rho} \frac{\partial \sigma_{21}}{\partial A_{31}} \\ -\frac{1}{\rho} \frac{\partial \sigma_{31}}{\partial \rho} & 0 & -\frac{1}{\rho} \frac{\partial \sigma_{31}}{\partial A_{11}} & -\frac{1}{\rho} \frac{\partial \sigma_{31}}{\partial A_{21}} & -\frac{1}{\rho} \frac{\partial \sigma_{31}}{\partial A_{31}} \end{pmatrix} \quad (\text{B.26})$$

$$\Xi_2 = \begin{pmatrix} \rho & 0 & 0 \\ (\rho c_0^2 + \sigma_{11} - \rho \frac{\partial \sigma_{11}}{\partial \rho}) & (\sigma_{21} - \rho \frac{\partial \sigma_{21}}{\partial \rho}) & (\sigma_{31} - \rho \frac{\partial \sigma_{31}}{\partial \rho}) \\ A_{11} & A_{12} & A_{13} \\ A_{21} & A_{22} & A_{23} \\ A_{31} & A_{32} & A_{33} \end{pmatrix} \quad (\text{B.27})$$

$$\Xi = \Xi_1 \Xi_2 = \begin{pmatrix} \Omega_{11}^1 + \left(c_0^2 + \frac{\sigma_{11}}{\rho} - \frac{\partial \sigma_{11}}{\partial \rho}\right) \Omega_{12}^1 + \left(\frac{\sigma_{21}}{\rho} - \frac{\partial \sigma_{21}}{\partial \rho}\right) \Omega_{13}^1 + \left(\frac{\sigma_{31}}{\rho} - \frac{\partial \sigma_{31}}{\partial \rho}\right) \\ \Omega_{21}^1 & \Omega_{22}^1 & \Omega_{23}^1 \\ \Omega_{31}^1 & \Omega_{32}^1 & \Omega_{33}^1 \end{pmatrix} \quad (\text{B.28})$$

Using the eigendecomposition $\Xi = Q^{-1} D^2 Q$ as before, we have:

$$R = \left\{ \begin{pmatrix} \frac{1}{2} \Xi_2 (D^2 Q)^{-1} & \frac{1}{2} \Xi_2 (D^2 Q)^{-1} \\ 0_{6,3} & 0_{6,3} \\ \frac{1}{2} (DQ)^{-1} & -\frac{1}{2} (DQ)^{-1} \end{pmatrix}, \begin{pmatrix} 1 & 0 \\ 0 & 1 \\ -\Pi_1^{-1} \frac{\partial \sigma_1}{\partial \rho} & \Pi_1^{-1} \mathbf{e}_1 \\ \mathbf{0}_9 & \mathbf{0}_9 \end{pmatrix}, \begin{pmatrix} 0_{2,3} & 0_{2,3} \\ -\Pi_1^{-1} \Pi_2 & -\Pi_1^{-1} \Pi_3 \\ I_3 & 0_{3,3} \\ 0_{3,3} & I_3 \\ 0_{3,3} & 0_{3,3} \end{pmatrix} \right\} \quad (\text{B.29})$$

By considering their products with the first 8 columns of R , two of the left eigenvectors corresponding the the 7th and 8th right eigenvectors must come in the form of the rows of the following matrix:

$$\begin{pmatrix} W & X & Y & Z \end{pmatrix} \quad (\text{B.30})$$

where $W \in \mathbb{R}^{2,5}$ and $X, Y, Z \in \mathbb{R}^{2,3}$, and:

$$W \Xi_2 (D^2 Q)^{-1} + Z (DQ)^{-1} = 0 \quad (\text{B.31a})$$

$$W \Xi_2 (D^2 Q)^{-1} - Z (DQ)^{-1} = 0 \quad (\text{B.31b})$$

$$W \begin{pmatrix} 0_{2,3} \\ -\Pi_1^{-1} \Pi_2 \end{pmatrix} + X = 0 \quad (\text{B.31c})$$

$$W \begin{pmatrix} 0_{2,3} \\ -\Pi_1^{-1} \Pi_3 \end{pmatrix} + Y = 0 \quad (\text{B.31d})$$

Thus:

$$Z = 0 \quad (\text{B.32a})$$

$$X = W_{:,3:5} \Pi_1^{-1} \Pi_2 \quad (\text{B.32b})$$

$$Y = W_{:,3:5} \Pi_1^{-1} \Pi_3 \quad (\text{B.32c})$$

and

$$W \begin{pmatrix} \rho & 0 & 0 & 1 & 0 \\ \left(\rho c_0^2 + \sigma_{11} - \rho \frac{\partial \sigma_{11}}{\partial \rho}\right) & \left(\sigma_{21} - \rho \frac{\partial \sigma_{21}}{\partial \rho}\right) & \left(\sigma_{31} - \rho \frac{\partial \sigma_{31}}{\partial \rho}\right) & 0 & 1 \\ A_{11} & A_{12} & A_{13} & \vdots & \vdots \\ A_{21} & A_{22} & A_{23} & -\Pi_1^{-1} \frac{\partial \sigma_1}{\partial \rho} & \Pi_1^{-1} \mathbf{e}_1 \\ A_{31} & A_{32} & A_{33} & \vdots & \vdots \end{pmatrix} = WM = \begin{pmatrix} 0 & 0 & 0 & 1 & 0 \\ 0 & 0 & 0 & 0 & 1 \end{pmatrix} \quad (\text{B.33})$$

By the properties of block matrices:

$$M^{-1} = \begin{pmatrix} -A^{-1}C(I - BA^{-1}C)^{-1}A^{-1}(I + C(I - BA^{-1}C)^{-1}BA^{-1}) \\ (I - BA^{-1}C)^{-1} & -(I - BA^{-1}C)^{-1}BA^{-1} \end{pmatrix} \quad (\text{B.34})$$

where

$$B = \begin{pmatrix} \rho & 0 & 0 \\ \left(\rho c_0^2 + \sigma_{11} - \rho \frac{\partial \sigma_{11}}{\partial \rho}\right) & \left(\sigma_{21} - \rho \frac{\partial \sigma_{21}}{\partial \rho}\right) & \left(\sigma_{31} - \rho \frac{\partial \sigma_{31}}{\partial \rho}\right) \end{pmatrix} \quad (\text{B.35a})$$

$$C = \begin{pmatrix} \cdots & -\Pi_1^{-1} \frac{\partial \sigma_1}{\partial \rho} & \cdots \\ \cdots & \Pi_1^{-1} \mathbf{e}_1 & \cdots \end{pmatrix}^T \quad (\text{B.35b})$$

Thus:

$$W = \left((I - BA^{-1}C)^{-1} - (I - BA^{-1}C)^{-1}BA^{-1} \right) \quad (\text{B.36})$$

$$W = (I - BA^{-1}C)^{-1} (I_2 - BA^{-1}) \quad (\text{B.37a})$$

$$X = -(I - BA^{-1}C)^{-1} BA^{-1} \Pi_1^{-1} \Pi_2 \quad (\text{B.37b})$$

$$Y = -(I - BA^{-1}C)^{-1} BA^{-1} \Pi_1^{-1} \Pi_3 \quad (\text{B.37c})$$

$$L = \left\{ (I_2 - BA^{-1}C)^{-1} \begin{pmatrix} Q\Xi_1 - \frac{1}{\rho}Q\Pi_2 - \frac{1}{\rho}Q\Pi_3 & DQ \\ Q\Xi_1 - \frac{1}{\rho}Q\Pi_2 - \frac{1}{\rho}Q\Pi_3 & -DQ \end{pmatrix} \right. \\ \left. \begin{pmatrix} I_2 - BA^{-1} - BA^{-1}\Pi_1^{-1}\Pi_2 & -BA^{-1}\Pi_1^{-1}\Pi_3 & 0_{2,3} \\ 0_{3,5} & I_3 & 0_{3,3} & 0_{3,3} \\ 0_{3,5} & 0_{3,3} & I_3 & 0_{3,3} \end{pmatrix} \right\} \quad (\text{B.38})$$

$$\mathbf{P} = \begin{pmatrix} \rho \\ p \\ A_{11} \\ A_{21} \\ A_{31} \\ A_{12} \\ A_{22} \\ A_{32} \\ A_{13} \\ A_{23} \\ A_{33} \\ v_1 \\ v_2 \\ v_3 \\ J_1 \\ J_2 \\ J_3 \end{pmatrix} \quad (\text{B.13})$$

$$\begin{aligned}
 \mathbf{S}_p = \frac{1}{\theta_1} & \begin{pmatrix} 0 \\ \left(\frac{1}{E_p} - 2\rho^2 \frac{\partial \log(c_s)}{\partial \rho}\right) \|\psi\|_F^2 \\ -\psi_{11} \\ -\psi_{21} \\ -\psi_{31} \\ -\psi_{12} \\ -\psi_{22} \\ -\psi_{32} \\ -\psi_{13} \\ -\psi_{23} \\ -\psi_{33} \\ 0 \\ 0 \\ 0 \\ 0 \\ 0 \\ 0 \\ 0 \\ 0 \end{pmatrix} + \frac{1}{\theta_2} \begin{pmatrix} 0 \\ \frac{1}{E_p} \|\mathbf{H}\|^2 \\ 0 \\ 0 \\ 0 \\ 0 \\ 0 \\ 0 \\ 0 \\ 0 \\ 0 \\ 0 \\ 0 \\ 0 \\ 0 \\ -H_1 \\ -H_2 \\ -H_3 \\ 0 \end{pmatrix} + \begin{pmatrix} 0 \\ \frac{1}{E_p} \\ 0 \\ 0 \\ 0 \\ 0 \\ 0 \\ 0 \\ 0 \\ 0 \\ 0 \\ 0 \\ 0 \\ 0 \\ 0 \\ 0 \\ 0 \\ 0 \\ -K \end{pmatrix} \quad (\text{B.14})
 \end{aligned}$$

Appendix C

Model Parameters

The parameters for different materials under different equations of state are given in the tables below. All variables are given in SI units.

C.1 Material Properties

Material	ρ_0	p_0	T_0	c_v	c_s	μ	c_t	κ	P_r
Air	1.18	10100		721	1	1.85×10^{-5}	1		0.714
Helium	0.163	10100		3127	1	1.99×10^{-5}	1		0.688
Water	1000	10000		950	10^{-4}	10^{-3}	10^{-4}		7
PBX	1840	10000		-	10^{-4}	10^{-5}	-		-
Aluminium	2710	0	300	900	3160	-			-
Copper	8930	0	300	390	2141	-			-
Steel	7860	0	298	134	2888	-			-
C4	1590								

Table C.1: Reference parameters for various materials

C.2 Equation of State Parameters

	Ideal/Stiffened Gas		Shock Mie-Gruneisen			Godunov-Romenski			
	γ	p_∞	c_0	Γ_0	s	c_0	α	β	γ
Air	1.4	-				-	-	-	-
Helium	1.66	-				-	-	-	-
Water	4.4	6×10^8				-	-	-	-
PBX	2.85	-				-	-	-	-
Aluminium	-	-				5037	1	3.577	2.088
Copper	-	-	3939	2	1.5	3939	1	3	2
Steel	-	-	4030	1.43	1.24				
C4	-	-							

Table C.2: Parameters for the Ideal-/Stiffened-Gas, Shock Mie-Gruneisen, and Godunov-Romenski equations of state

Material	τ_1	σ_Y	n
Copper	0.1	9×10^8	10
Aluminium	1	4×10^8	20

Table C.3: Plasticity parameters for various materials

C.3 Combustion Parameters